Development of precipitation hardenable Mg-Sn based wrought alloys

Fady Refaat Elsayed

Doctoral Program in Materials Science and Engineering

Submitted to the Graduate School of

Pure and Applied Sciences

In Partial Fulfillment of the Requirements

For the Degree of Doctor of Philosophy in Engineering

at the

University of Tsukuba

Table of Contents

Acknowledgments

This work was undergone throughout the doctoral course at the University of Tsukuba under the National Institute for Materials Science - Junior Research Assistantship program. I would like to take this opportunity to thank NIMS for providing the financial assistance during the doctoral course.

I would like to express my sincere appreciation to my supervisor Professor Kazuhiro Hono for providing me with the opportunity to undertake my doctoral research in the Magnetic Materials Unit MMU- Nanostructure Analysis group and providing me with guidance during my research work.

A great debt of gratitude is owed to Dr. Taisuke Sasaki for the invaluable assistance in teaching concepts, experimental work, and discussions; his continuous encouragement, help, and guidance was instrumental in bringing this work to its completion.

I would like to thank Dr. Tadakatsu Ohkubo for his support with experimental efforts. Special thanks to Dr. Chamini Mendis for providing guidance and help at the start of my research work. I also would like to extend many thanks for all the staff and students of the Magnetic Materials Unit and Nanostructure Analysis Group for their support during my stay.

Finally, I wish to extend my thanks to my family and friends for their support and encouragement.

Chapter (1) – Introduction and Literature Review

1.1 Magnesium Alloys General Background

1.1.1 Historical background

Magnesium is the sixth most abundant element, constituting 2% of the total mass of the Earth's crust [(1)]. It belongs to the second main group in the periodic table of elements (alkaline earth metals). The name of magnesium originates from an area in northern Greece called 'Magnesia' [(1)].

The history of the metal began in 1755 when Joseph Black a Scottish Chemist discovered that magnesia contained a new element, magnesium. British Chemist and Scientist -Sir Humphrey Davy is credited with the discovery, when he isolated the metal in 1808 by decomposing wet magnesium sulphate by electrolysis using a voltaic cell, and a mercury cathode [(2)].

Twenty years later, French man Antoine Alexandre Brutun Bussy isolated magnesium by fusing dehydrated magnesium chloride with potassium at elevated temperatures. Michael Faraday in 1833 reduced dehydrated magnesium chloride by electrolysis, and obtained pure metallic magnesium [(2)], while German Robert Bunsen produced metallic magnesium, and opened base for industrial production in 1852 by modifying the Bunsen carbon zinc electric cell starting from fused, dehydrated magnesium chloride.

Magnesium chemical applications outweighed structural uses in the beginning of its use [2]. In second half of 19th century, few tons of magnesium was produced mainly for use in flash-lights and pyrotechnics [2]. In 1909, a crankcase for an aero plane cast by IG Farben Elektron Co. GmbH made from a magnesium aluminum zinc (AZ) alloy was presented at Frankfurt (International Air Transport) fair [2]. This represented one of the earliest structural applications.

Since World War II, there has been a dramatic rise in the use of magnesium in structural uses (228,000 tons per year in 1944) [2], utilizing the desired high strength to weight ratio in aerospace applications. The RB-36D US strategic bomber contained alone around 9000 kg of magnesium [3]. Many other applications were used in military vehicles and airplanes, but the metal was used also in production of flares and incendiary bombs.

There have been attempts to use magnesium in civilian automobile production, but these were relatively few. The famous Volkswagen beetle (introduced in late 1930's), contained nearly 20 kg of magnesium AS-series alloy (Aluminum-silicon) used for the crankcase, and transmission housing casting[2]. This represented the largest single application of magnesium alloys at this time.

The annual magnesium consumption of Volkswagen group then rose reaching 42,000 tons in 1972, a record high which was not encountered until nearly 20 years later [4].

Other non-direct structural and chemical uses for magnesium were as an alloying element in aluminum alloys, in de-sulfurization, de-oxidation of steel, and as a reducing agent in titanium and zirconium production.

1.1.2 Magnesium Production Processes

Due to its high reactivity, magnesium is not found in elemental form in nature, only in chemical combinations in natural ores like the mineral dolomite ($MgCO_3$.Ca CO_3), and Magnesite ($MgCO_3$). Magnesium is also present as the third most common element in sea water as Mg^{2+} ions, with an abundance of 0.13% of sea water composition [(2)]. It is also abundant in the mineral carnallite ($MgCl_2$-KCl-$6H_2O$) extracted from sea water.

Owing to its low ionization energy, all magnesium production technologies require a reduction agent which can transfer two electrons to the magnesium. The reduction agents are usually electric current operated at the appropriate potential, coal in various forms, and silicone-based materials (FeSi). All thermal and electrochemical production technologies stem from this central feature [(2)].

All the electrochemical technologies use direct current electricity form, which passes through the electrolysis cells and discharges chlorine and magnesium ions into gaseous chlorine and metallic magnesium. The thermal methods are based on heating

of magnesia in the presence of various reduction materials, to a variety of temperatures. At a particular temperature the reduction reaction takes place and the magnesium becomes metal, usually in its gaseous form [2].

In the electrolysis method, dehydrated magnesium chloride is obtained either by roasting dolomite, and its addition to sea water, or by reaction of magnesium oxide, carbon, and chlorine. Magnesium chloride ($MgCl_2$) is then reduced by a direct electric current, into magnesium metal, and chlorine gas at a temperature of 700°C.

- $MgCl_2$ + 641.8 kJ □ Mg + Cl_2

In thermal processes which are most popular in Chinese production of magnesium, magnesium oxide, and ferrosilicon are heated, and the metal is reduced, and recovered in vapor form, cooled, and condensed into solid form.

The silicothermic process (or most commonly known as the Pidgeon process) has many variations; one of them can be shown in the following chemical reaction[2]:

- 2MgO (solid) + Si (Fe) □ 2Mg (vapor) + SiO_2 (1iquid) + Fe Pressure = $1*10^5$ Pa; T = 2,300°C or Pressure = 13.3 Pa; T = 1,500°C

4

1.1.3 Magnesium Alloys Properties

Magnesium alloys exhibits a number of interesting properties that allow their use in a vast area of non-structural and structural applications. The pure metal is rarely used; it's mostly alloyed to improve mechanical, thermal, and other physical properties. The properties of pure magnesium are summarized in Table 2.1 **(1)**

Table 1.1: Properties of pure magnesium **(1)**:

Crystal structure	HCP
Density	1738 kg/m^3 @ room temperature
Young's Modulus	45 GPa
Ultimate Tensile Strength	80-180 MPa
Fracture Elongation	1-12%
Melting Point	650+/- 0.5 °C
Boiling Point	1090 °C
Specific Heat Capacity	1.05 $kJkg^{-1}K^{-1}$
Fusion Heat	195 $kJk^{-1}g^{-1}$
Thermal Conductivity	156 $Wm^{-1}K^{-1}$ @ room temperature
Linear Expansion Coefficient	$26*10^{-4}K^{-1}$ @ room temperature
Shrinkage (solid-liquid)	4.20%
Specific Electrical Conductivity	22.4 $m/(\_ /mm^{-2})$ @ room temperature
Normal Potential	-2.37 V

Magnesium as the lightest of the structural metals is substantially less dense than aluminum. Its density is nearly two third that of aluminum and one fifth that of steel, featuring 30% weight savings compared to Al and around 75% compared to Steels. It also has one of the highest strength to weight ratios among light metals reaching 14

km breaking length. (Breaking length is a method to represent values for specific strength usually used by textile industry = Length of specimen whose weight is equal to the breaking load, and is calculating by dividing the ultimate tensile strength in MPa by (density* gravitational acceleration)

$$\frac{MPa * m_3 * s_2 \square (breaking \square length) * 10^2 m}{Kg * m * 10}$$

A summary of properties of most popular most magnesium alloys

Commercial used alloys, in comparison to aluminum alloys is represented in table 2.2 [7]**Table 1.2**: Common commercial magnesium, and aluminum alloys specific strength, and mechanical properties [7]

	Density	E -modulus		Yield Strength		Ultimate Tensile Strength	
	[g.cm-3]	[GPa]	Specific Modulus* [km]	[MPa]	Specific YS Breaking Length*[km]	[MPa]	Specific UTS Breaking Length*[km]
AZ91 permanent mold	1.8	45	$2.55*10^3$	110	6.23	160	9.06
AZ91 high pressure die cast	1.8	45	$2.55*10^3$	160	9.06	230	13.03
Al-Si8Cu3 permanent mold	2.7	70	$2.64*10^3$	160	6.04	220	8.31
Al-Si8-Cu3 high pressure die cast	2.7	70	$2.64*10^3$	240	9.06	310	11.7
AZ31 H24	1.8	45	$2.55*10^3$	200	11.33	269	15.23
6061 O	2.7	70	$2.64*10^3$	55	2.08	125	4.72
6061 T6	2.7	70	$2.55*10^3$	275	10.38	310	11.7

* property divided by density, and gravity acceleration

Magnesium alloys show very good machinability and die casting offer the possibility of manufacturing the most complex shaped parts. Cast, and forged parts made of magnesium alloys are weldable and machinable. Another interesting property of magnesium is its good damping behavior, which makes the use of these alloys attractive for increasing the life cycle of machines and equipment, and the reduction of harshness, noise, and vibrations [1].

Summary of magnesium alloys advantages:

- Low density of alloys ~ 1.8 kgm^{-3}
- High specific strength
- Excellent castability
- Highly recyclable
- Improved corrosion resistance with high-purity al loys, and modern coating systems.
- High damping properties
- Good machinability
- Good weldability under inert gases

1.1.4 Magnesium Alloys Applications

Since the World War II, there had been a dramatic rise in the use of magnesium in structural uses (228,000 tones per year in 1944) **(11)**, mainly for aircraft construction, it took nearly another 40 years to reach the same size level in 1992. Many cast parts were used in military vehicles and airplanes, but the metal was used in production of flares and incendiary bombs.

Figure 1.1 : Northrop XP-56 – first aero plane designed using magnesium

Since the 1990's there has been renewed interest in using magnesium based alloys in automotive, household, consumer electronics and sport applications. Developments in alloy technology, and improvements in melting and casting processes as well as in surface treatment have made magnesium alloys an attractive choice for lightweight construction. The driving force for the renewed interest is their attractive properties such as heat dissipation, damping, machinability; electro-magnetic shielding, recycling, and most importantly the weight savings induced that result in lifetime fuel savings and CO_2 emissions.

The main drive for the lightweight construction is the industry's commitment to achieve a 25% reduction in average fuel consumption for all new cars compared to levels in 1990. For that reason the expected global growth of Magnesium usage is around 6% until the end of the decade. The amount of magnesium used in modern cars, is substantially increasing every year, which can be seen in figure 1.2. This increase can be attributed to the request for weight reduction, and carbon dioxide

emissions cut, increase due to the increasing fuel costs, and global warming caused by CO2 emissions.

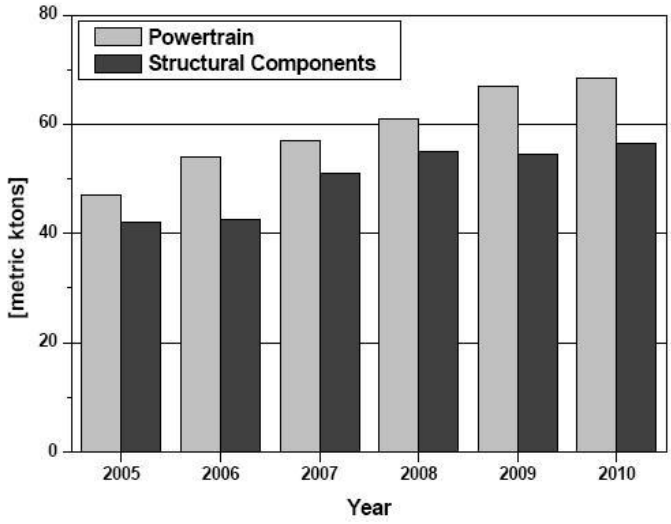

Figure 1.2: Magnesium use in automotive production (1)

Besides the numerous room temperature applications for die cast magnesium components; the powertrain segment is a very important market for the magnesium industry, and for that reason, new alloys with improved creep resistance are being developed for high temperature power train applications. Figure 1.3 shows a composite engine block jacket made from aluminum insert encased in an AJ62 creep resistant magnesium alloy (6)

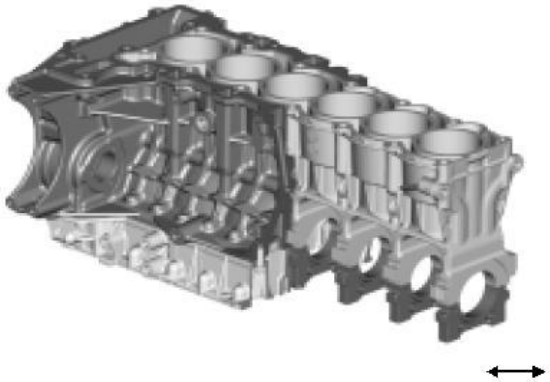

Figure 1.3: Engine block jacket made from magnesium (6)

Pressure die-cast components are extensively used because they permit the manufacturer to create parts with complex geometries. This manufacturing technology makes it possible to integrate a diverse set of functions into a single component in one manufacturing step which reduce costs significantly. Examples of complex structural

parts that can be manufactured from magnesium cast alloys are instrument panels, and car seats. Magnesium alloys have a huge potential use, in many automotive structural applications out of the power train segment which lead to a huge total weight reduction of a car. These possible applications are shown in figure 1.4

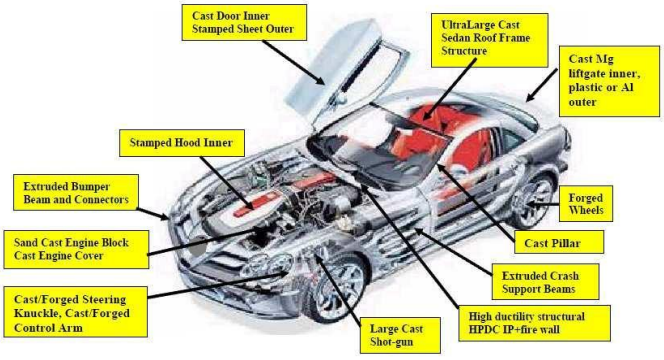

Figure 1.4: Potential Magnesium applications in modern automotives (8)

Manufactures of consumer electronics like laptops, mobile phones, and portable mp3 players as well as sports goods manufacturers are also utilizing the lightweight of magnesium in their product design in order to be more appealing to customers**,** an example of these applications is shown in figure 1.5 [(9)]

Figure 1.5: Examples of electronics parts utilizing the light-weight of magnesium alloys [(9)]

One of the milestones of Magnesium use in automotive structural components is the (Volkswagen 1-Litre Car), shown in figure 1.6 with a fuel consumption of 1 liter diesel/ 100 km, and weighing 290 kg.

Figure 1.6: The Volkswagen magnesium space frame in the "1-Lit re Car" [(10)]

The 1-Litre-Car's body is made completely of carbon fiber composites, tensioned over a space frame that is made of magnesium. Lightweight space frame including various magnesium components (gearbox housing, front axle upper wishbone, fuel pump housing, steering-wheel and steering box, brake pedal, and seat frames.) can be seen in figure 1.7

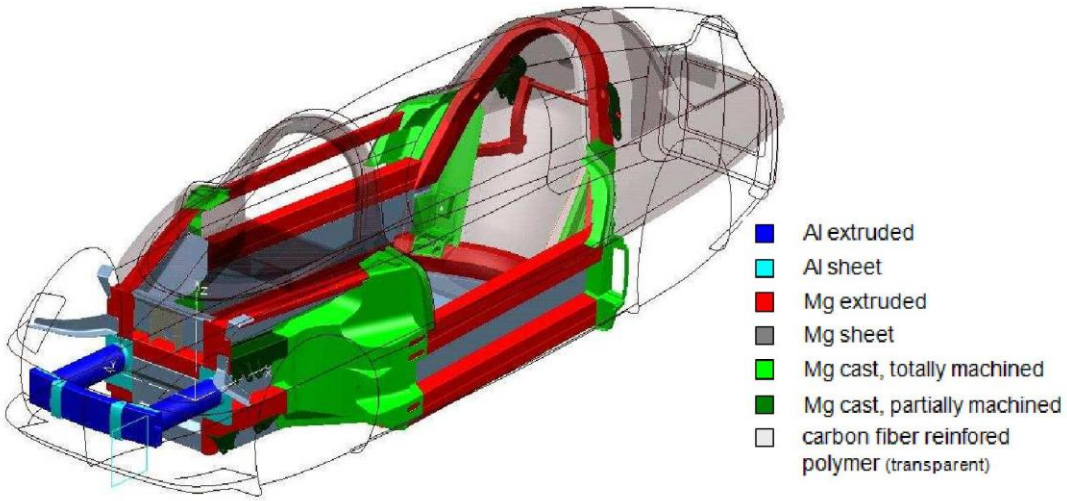

Figure 1.7: The VW 1-liter Space Frame utilizing extensive use of magnesium [8]

1.1.5: Structure of Magnesium:

The magnesium lattice parameters at room temperature are a = 0.32092 nm and c = 0.52105 nm with a (c/a) ratio of 1.6236. These parameters are nearly perfectly close to the packed hexagonal structure [2, 3, 11]. The hexagonal structure of the magnesium unit cell is shown in Figure 1.8 showing the major planes and directions [11].

In general, primary and secondary slip and twinning occur at room and elevated temperatures. Primary slip takes place on the (0001) basal plane and in the $\langle 11\bar{2}0 \rangle$ most closely packed direction of the plane at room temperature while secondary slip occurs in the $\langle 11\bar{2}0 \rangle$ direction on the $\{10\bar{1}0\}$ vertical face planes.

Table 1.3: Most important slip systems in Magnesium deformation (33)

Slip plane	Slip direction
{0001}	$\langle 11\bar{2}0 \rangle$
$\{10\bar{1}0\}$	$\langle 11\bar{2}0 \rangle$
{1011}	$\langle 11\bar{2}0 \rangle$

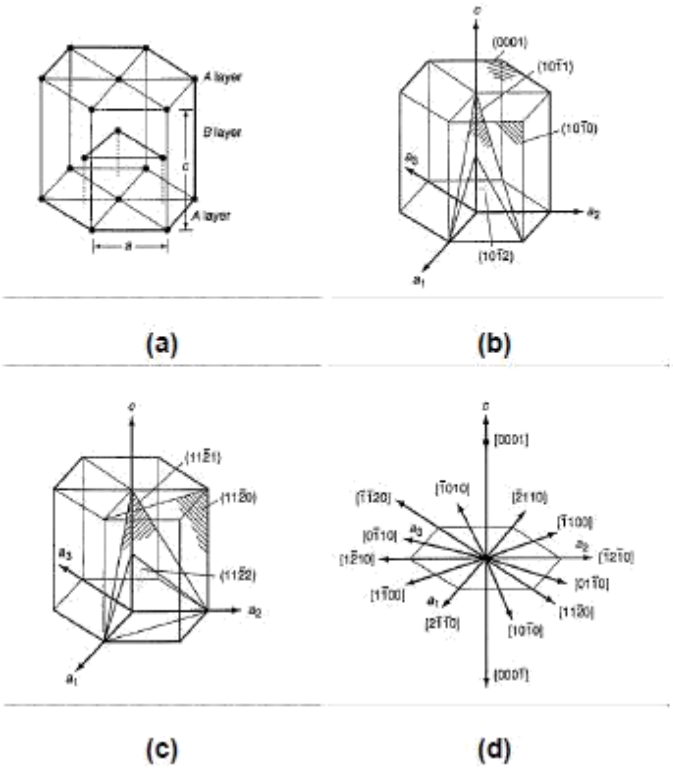

Figure 1.8: The HCP crystal structure showing unit cell, major planes and directions[11]

1.1.6 Magnesium Alloys Naming Convention

Although there is no international system for designating magnesium, the naming method used by the American society for testing, and materials (ASTM), is the most commonly used for magnesium alloys [11]

The method is a three part letter-number-letter. The first part consists of code letters indicating the two principal alloying elements listed in order of decreasing alloying

content. The second part consists of the weight percentages of these two elements rounded off to the nearest whole number, and listed in the same order as the code letters. The third part consists of an assigned letter- beginning with (A) to distinguish between states of development of alloys having the same nominal composition. Example: AZ91D is a magnesium alloy with 9% aluminum, 1% zinc, and is the fourth specific composition registered having this nominal composition.

Table 1.4: Code letters system for magnesium alloys designation [11]

Letter	Alloying Element	Letter	Alloying Element
A	Aluminum	**N**	Nickel
B	Bismuth	**P**	Lead
C	Copper	**Q**	Silver
D	Cadmium	**R**	Chromium
E	Rare earth metals	**S**	Silicon
F	Iron	**T**	Tin
H	Thorium	**W**	Yttrium
K	Zirconium	**Y**	Antimony
J	Strontium	**Z**	Zinc
L	Lithium		
M	Manganese		

Table 1.5: Temper designation for magnesium alloys [11]

Letter	Temper
F	As fabricated
T4	Solution heat treated
T6	Solution heat treated and artificially aged

1.2 Mg wrought alloys microstructure design for high strength

The mechanical properties of magnesium can be widely influenced by alloying. The strength of cast magnesium alloys is obtained by one or more of the well known hardening mechanisms: solid solution hardening, grain refinement or Hall Petch hardening, age hardening, cold working and dispersion hardening. Martensite formation is a well understood strengthening mechanism, but is not relevant in magnesium alloys.

1.2.1 Solid solution strengthening

Pure metals are almost always softer than alloys composed of same base metal. Alloying with impurity atoms that go to either substitutional or interstitial solid solution greatly strengthen, and harden metals. The mechanism by which solid solution hardening work is that, solute atoms impose lattice strains on surrounding host atoms. Lattice strain field interactions between dislocations and solute atoms occur, and as a result, dislocation movement is restricted [(33)].

1.2.2 Grain refinement

The size of grains, or average grain diameter, in metals influences the mechanical properties to a large extent. Adjacent grains have some different crystallographic orientations, and a common grain boundary. During plastic deformation, slip, or dislocation motion must go across these grain boundaries, so that grain boundaries could be seen as barriers to dislocation motion.

The grain size dependence of the yield stress can be expressed through the Hall-Petch relationship [33]:

$$\sigma_{yield} = \sigma_0 + K_y d^{-1/2}$$

Where d is the average grain diameter, σ_0 and Ky are material constants**.** The relationship expresses why most fine grained materials are stronger than coarse grained ones, since the former have greater grain boundary area to oppose dislocation motion. Fine grain size improves most mechanical properties, except creep resistance because diffusion occurs on grain boundaries. The grain size is usually manipulated by different techniques such as:

a) Chemical grain refinement: By using certain alloying additions or ceramic poarticles like SiC.

b) Severe plastic deformation (SPD) processes: like equal channel angular

pressing (ECAP) or equal channel angular extrusion (ECAE), and high pressure torsion (HPT)

c) Controlling solidification: higher cooling rates, ultrasonic treatment of melt, high shearing forces during melting> thixomolding

d) Zr additions have been established as grain refiners in Mg-Zn system ZK60 alloys.

1.2.3 Dispersion hardening – MMC,s

The strength of dispersion strengthened materials depends on the size, distribution and volume fraction of dispersoids, where dislocations cannot cut the incoherent dispersoids like fibres or whiskers [2] . For an optimum dispersion strengthening a large number of small, hard and discontinuous dispersed phase particles should form inside a ductile matrix to form a metal matrix composite (MMC).

These particles provide better blockage to dislocations, and optimum strength. Particle or fibre reinforcement results in increase of the maximum strength, yield strength, Young's modulus, heat resistance, creep resistance, and reduction of the thermal expansion coefficient. All these effects make dispersion strengthened materials very attractive for many demanding applications. Common reinforcements include Al_2O_3, SiC, carbon, and glass fibers.

1.2.4 Age hardening

Intermetallic precipitates formed by the age hardening heat treatment process are very effective in hardening magnesium alloys. The main mechanism involves the formation of stable hard intermetallic phases at many points, like within the grains, and on grain boundaries which can be achieved by the appropriate choice of alloying elements and heat treatment. The most common precipitation hardenable systems require a large solid solubility of the main constituent element at higher temperature which decreases going down to room temperature to facilitate forming a super-saturated solid solution by rapid quenching during the solution treatment process. The nature of the precipitate, their structure, coherence and their inter-particle spacing at the grain boundary is also of great importance to restriction of grain boundary sliding [33]. Generally the better distributed, and finer the particles and more closely spaced, the better its obstructive effect to grain boundary sliding.

1.3 Major barriers to the use of magnesium wrought alloys in structural applications:

The major portion in magnesium structural use is in die-cast components. The main obstacle facing cast components in automotive applications is the poor creep resistance at temperatures above 150 ºC which is inadequate in most powertrain components.

As for the wrought products in the form of sheets, extrusions, and forgings: the lack of sufficient poor cold workability of the hexagonal lattice structure and the formation of twins and therefore the anisotropy of the properties of finished components. In addition; out of the few commercial wrought alloys developed; few alloys have higher or comparable yield strength in comparison with Aluminum wrought alloys in the same price range. That always constitutes a price disadvantage for Mg alloys if the strength level is lower than their Al counterparts.

Magnesium wrought alloys development are still in the development stage specially the area of precipitation hard enable heat treatable alloys where it is still immature compared to the well-established range of developed heat treatable Al alloys series. These factors have limited the usage of magnesium as a wrought material, although they have better mechanical properties than cast Mg alloys, and are comparable to some Al alloys (i.e. 6xxx series alloys). Therefore, the range, and size of use of magnesium wrought alloys in high volume applications is still limited.

Other Influential Factors in alloy development efforts are:

- The cost of production of the raw material (much fewer producers worldwide)
- The less ease of hot working compared to aluminum (strong texture and anisotropy)
- Relatively few wrought alloys developed compared to Aluminum alloys
- Corrosion resistance and better Coating systems.

All these factors prevent or restrict the current wide acceptance of using Mg alloys by the automotive/ aerospace industries; the largest markets for light metals wrought products.

Necessary Developments for Magnesium Alloys

In order to fully exploit the advantages of magnesium alloys, and increase their use in vehicle, aerospace, and other structural applications benefiting from their inherent property profile in lightweight construction, alloy development for cast, and wrought magnesium should be pursued to improve their property profile to compete with other lightweight structural materials like aluminum alloys, and polymer composites.

Some of the developments in magnesium alloys can be summarized in the figure 1.9 depending on the alloy composition; process used, and design criteria:

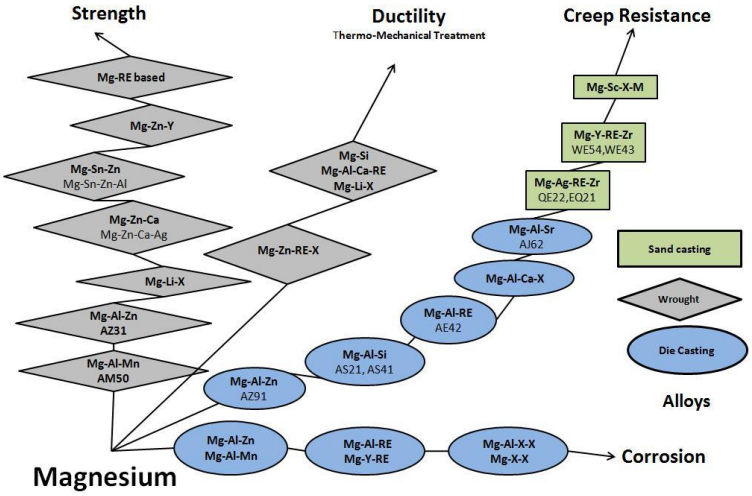

Figure 1.9: Developments in Mg alloys

Therefore, further necessary development in magnesium alloys include:

]

- Better and cheaper creep resistant alloys, with enhanced castability.

- Better age hardenable alloys for wrought products for room temperature applications.
- Better wrought alloys with enhanced strength, ductility, and formability.

- Better corrosion resistance and surface coatings for all alloys.

1.4: Precipitation Hardened Mg alloys

The majority of the commercial Mg wrought alloys are rarely heat treated after wrought processes although most of them are precipitation hardenable. This is because the age-hardening responses of commercial wrought alloys such as Mg–Al–Zn (AZ) and Mg–Zn (ZK) alloys are too low to achieve sufficient improvement by heat treatment . Additionally, the yield strength of the best commercial wrought Mg alloys is ~ 240 MPa, which is much lower than that of medium-strength 6xxx series Al–Mg–Si based alloys, so in order to compete with Al alloys, the yield strength of wrought Mg alloys needs to be improved to over 300 MPa (45). Tensile yield strengths and elongations of commercial wrought Mg alloys and alloy design efforts demonstrated by some recently developed experimental alloys are summarized in Figure 1.10

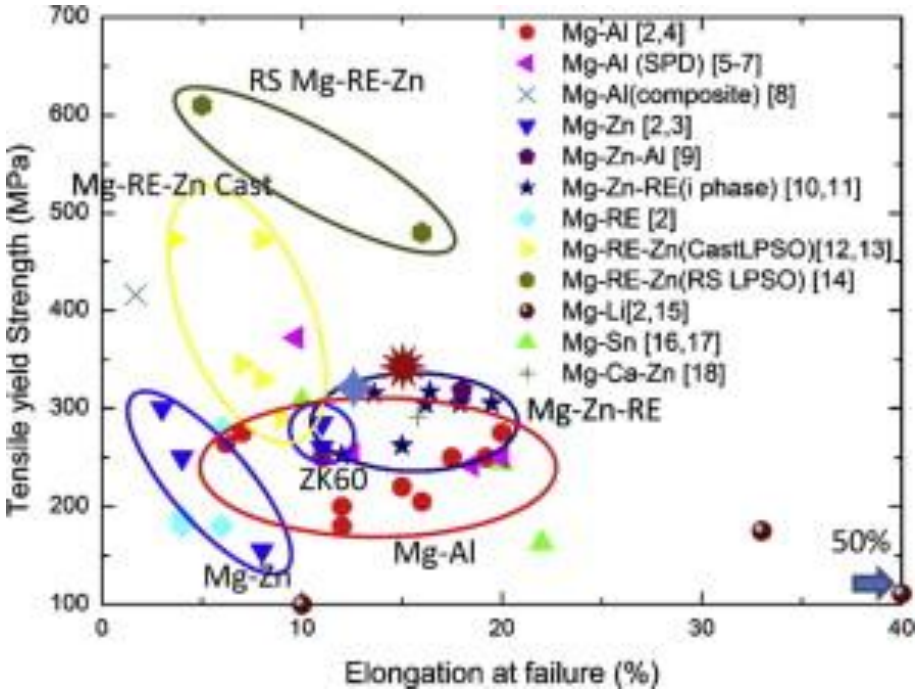

Figure 1.10: Tensile yield strength and elongations for wrought commercial and Experimental Mg alloys [45]

Pure magnesium is hardly used as a construction material. Alloying elements are used to influence a wide variety of product properties, and process-ability. Many elements including most transitional metals have poor solubility in magnesium alloys. Consequently there are only about ten elements which can be considered as the common alloying elements in magnesium alloys. Those elements which dissolve usually modify the ductility and the elastic properties by solid solution or precipitation hardening. Only dissolved additions can modify the elastic constants unless composites are considered [(2)].

The solubility of different elements in magnesium is shown in the figure below:

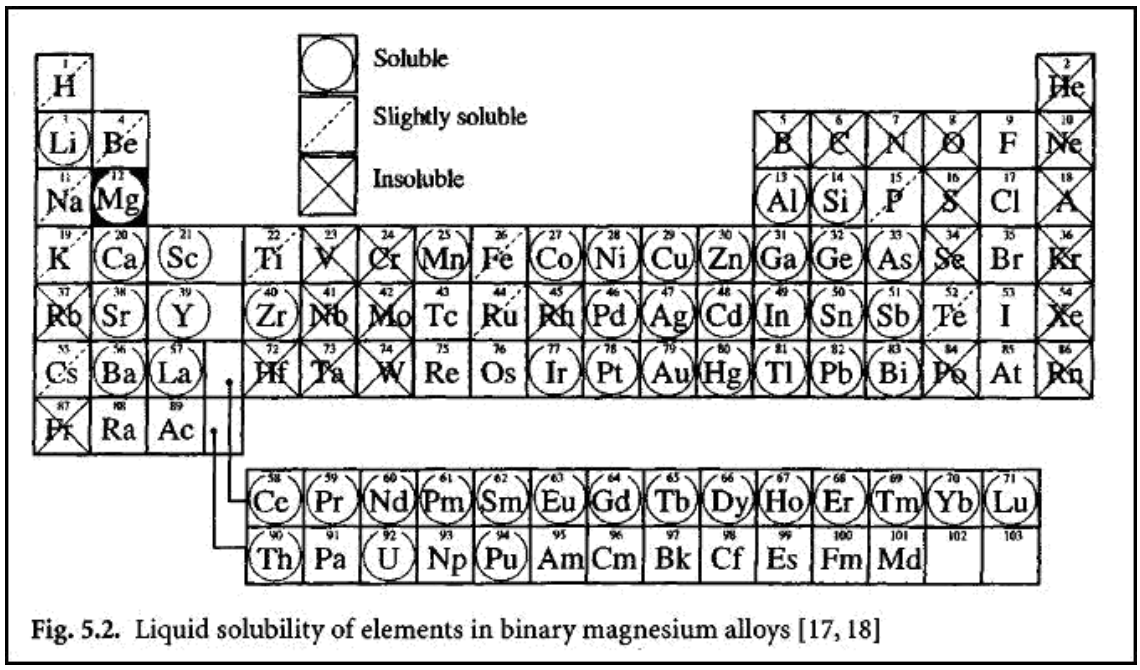

Fig. 5.2. Liquid solubility of elements in binary magnesium alloys [17, 18]

Figure 1.11: Solubility of different elements in magnesium [(2)]

When intermetallics are formed they restrict the ductility and often such alloys formed with these can only be used as casting alloys. The formation of intermetallics is usually exploited to improve the strength providing the precipitates have adequate size, coherence, and distribution. The formed precipitates in an alloy are important in determining the suitability of an alloy for applications in which creep resistance is necessary [(2)].

The most common alloying elements used in magnesium alloys are: Aluminum, Zinc, Manganese, Silicon, Rare Earths, Calcium, Lithium, Silver, Thorium, and Yttrium. Precipitation hardenable Mg alloys systems are mainly based on Mg-Al, Mg-Zn, Mg-RE, Mg-Ca, and Mg-Sn. Detailed description of various roles of alloying elements can be obtained from references: 1, 2, and 11.

1.4.1 Mg-Al System

Aluminum is by far the most common alloying element, and form the backbone of most casting alloys, and many wrought ones. The maximum solubility of Al in Mg is 11.8 at.% at a eutectic temperature of 437 °C and f alls to about 1% at room temperature [(11)]. Aluminum improves room temperature strength, and hardness, although the observed hardening effect can be observed till 120°C.

The creep resistance is limited due to the poor thermal stability of the $Mg_{17}Al_{12}$ phase above 120°C. The second major effect of aluminum is better castability of aluminum bearing alloys, which explain the reason why most die cast magnesium alloys contain aluminum (AZ, AM series). The optimum combination of strength and ductility in Al containing alloys being observed at about 6 wt. % [(2)].

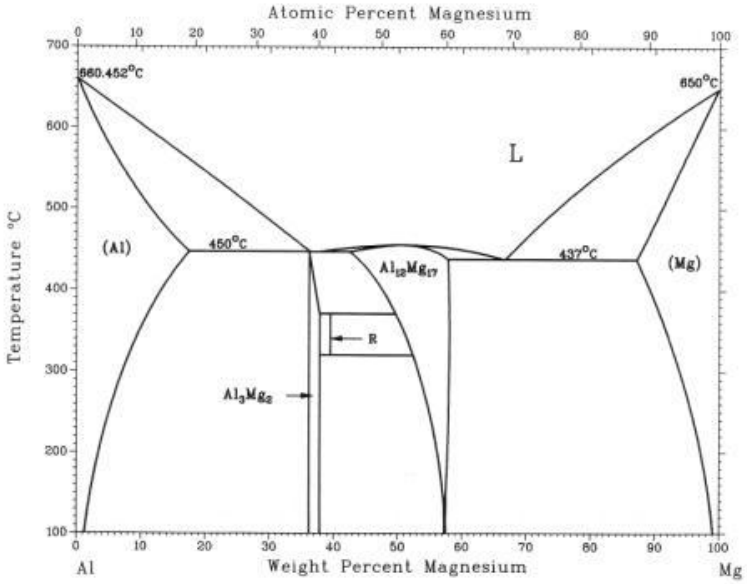

Figure 1.12: Mg-Al phase diagram [16]

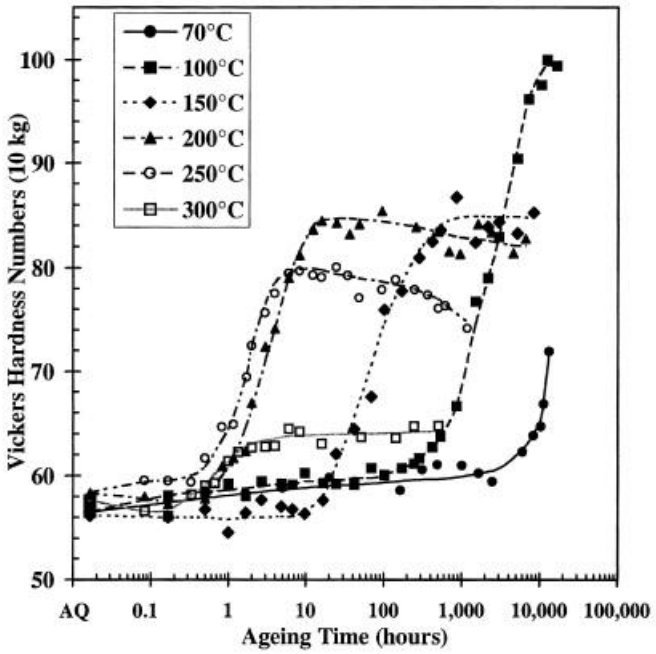

Figure 1.13: Age hardening behavior of AZ91 alloy at different temperatures(48)

1.4.2 Mg-Zn System

Zinc is also a very common alloying element, usually employed in conjunction with aluminum to form the most common commercial alloy system - the AZ series. Figure 1.14 demonstrates the binary Mg-Zn phase diagram showing the maximum solid solubility of Zn of 6.2 wt.-% in magnesium at the eutectic temperature 340°C. Zinc is specified in the second greatest amount in the Mg alloys. Zn is used in combination with zirconium (ZK60 alloy) or RE to obtain good strength by producing age-hardenable Mg-alloys. It enhances the room temperature mechanical properties when adding it to aluminum containing alloys [2]. Zn assists to avoid the harmful corrosive effect of iron and nickel impurities that might be present in Mg-alloys [11]. Also Zn increases the fluidity and thus improves castability inducing double effect of improving strength, and castability. Usually maximum amounts of Zinc used are less than 6 wt. % [(2)].

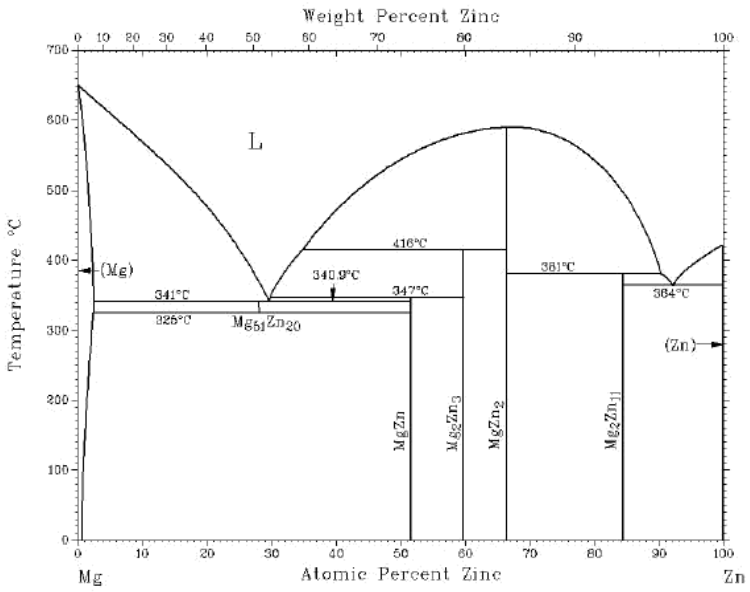

Figure 1.14: Mg-Zn phase diagram [(16)]

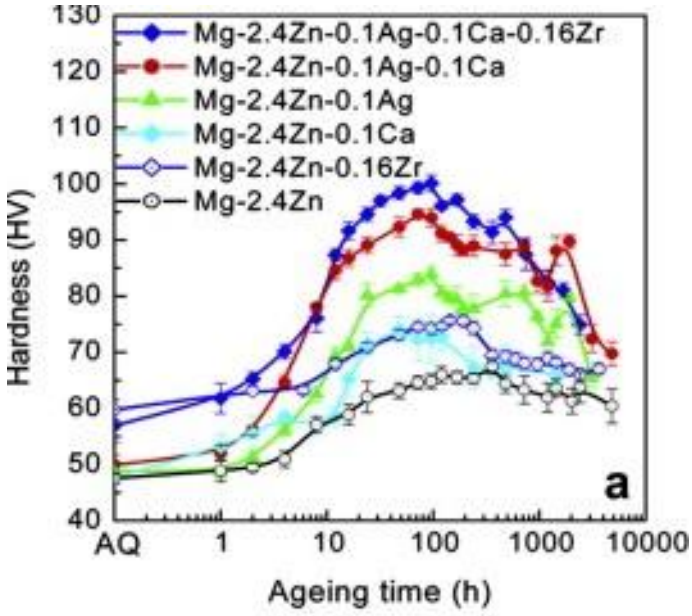

Figure 1.15: Age hardening behavior of Mg-Zn-Zr sytem with Ag and Ca microalloying additions alloys (45)

1.4.3 Mg-RE System

Rare earth elements are usually added to magnesium alloys as mish-metal (MM) as all elements have the same behavior. All rare earth elements form eutectic systems of limited solubility with magnesium at lower temperatures, thus enabling precipitation hardening to take place due to formation of stable intermetallic compounds. They are mainly used in to increase creep resistance for elevated temperature applications [(2)].

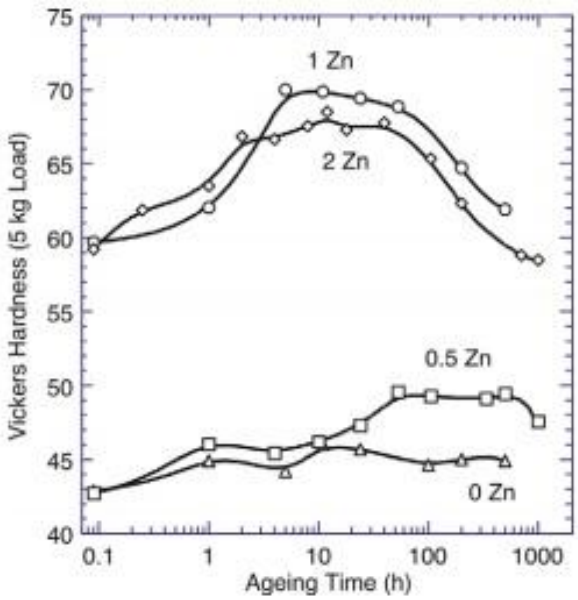

Fig. 1. Age hardening response at 250 °C of Mg–6Gd–0.6Zr alloys with and without Zn additions.

Figure 1.16: Age hardening behavior of Mg-Gd-Zn alloys (46)

1.4.4 Mg-Ca System

Calcium as well as other alkaline earth metals like strontium is more attractive in the development of creep resistant alloys - essentially replacing the unstable $Mg_{17}Al_{12}$ with more stable intermetallic phases. Calcium's low density and price makes it exceptionally competitive with the rare earth metals, if cheaper high creep resistance alloys are to be developed.

Calcium has been reported to have an approximate atomic diameter size difference of (–24%) with that of magnesium. Calcium tendency to form Mg_2Ca which has a melting point of 715°C and also the presence of eutectic at 516.5°C makes it attractive for high temperature applications [15]. In aluminum containing alloys it is being widely applied to improve oxidation resistance at high temperature [29, 30] and to improve the strength at high temperatures due to the formation of Mg_2Ca and Al_2Ca intermetallic phases. Concerning

castability, however, it has been reported that calcium lead to sticking to tools during casting and also can lead to hot cracking [(1)].

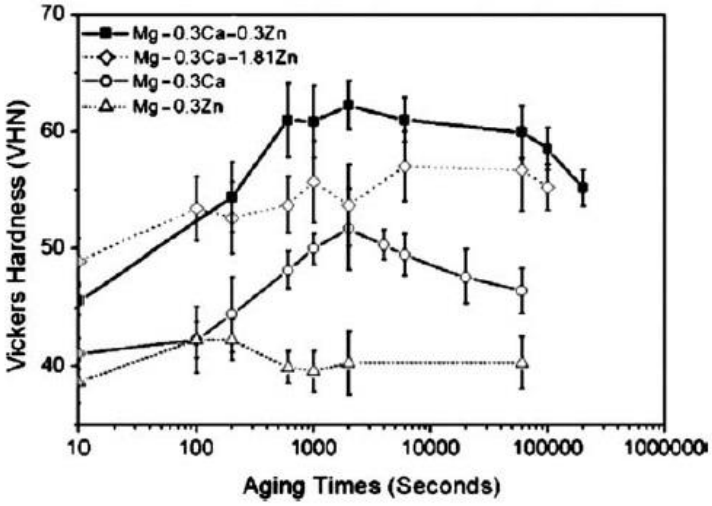

Figure 1.17: Age hardening behavior of Mg-Ca-Zn alloys at different temperatures(47)

Calcium has a lower density than either aluminum or magnesium; it is also known to be a microstructural refiner in magnesium alloys [(30)]. Previous investigations showed that in Mg-Al-Ca alloys, when Ca/Al mass ratio was more than 0.8, both Mg_2Ca andAl_2Ca phases were formed. When this ration was less than 0.8 only Al_2Ca phase was formed [(29)]. Since most of the Mg alloys modified by Ca have Ca/Al mass ratio less than 0.8, the formation of Al-Ca intermetallic phases is most likely rather than Mg_2Ca[(28)]. Al forms two types of intermetallic compounds Al_4Ca and Al_2Ca having high melting temperatures. These precipitates are generally present along the grain boundaries in the microstructure. The Al_2Ca phase especially has a high melting temperature of 1079 °C and thus results in metallurgical stability of the grain boundaries at elevated temperatures.

Recently two new compounds such as AlCa and Al_3Ca_8 have been discovered in Ca rich areas of Al-Ca system [(12)]. After recent extensive alloy research programs, it has become more possible to replace expensive rare earths by cheap calcium in magnesium alloys to achieve similar or comparable properties at high temperature.

1.4.5 Mg-Sn System

The system Mg-Sn has a relatively high Sn solubility limit (14.48 wt. %) at 561°C, (0.45 wt. %) at 200°C, and a very low solubility (0.035 at. %) at room temperature. These solubility limits provide the basis for improving the strength of magnesium-tin alloys through precipitation hardening ageing processes.

The Mg-Sn phase diagram in figure 1.18 shows the presence of Mg_2Sn with a melting temperature of 770°C and eutectic temperature of 56 1°C. This formation of the intermetallic phase shows good potential for creep resistance and high strength applications. The precipitation of Mg_2Sn stabilize the matrix structure which is a prerequisite for a creep resistance alloy [15] , and therefore, high-temperature properties which are superior to that of the AZ alloys, can be expected.

It has been reported that Sn in magnesium alloys confers some strengthening at the expense of ductility [13]. The large solubility of Sn in liquid magnesium and the low melting point of Sn (232°C) make Sn very attractive as an alloying element in magnesium alloys. Sn is also expected to reduce the magnesium free corrosion polarization, although there might be possibility of galvanic corrosion with alloys containing Al and or Zn [13].

The research into the Mg-Sn system stemmed from the need to develop promising age-hardenable creep resistant/wrought alloys that are RE- free. The Mg-RE cast alloys, with their enhanced strength, and creep resistance, are an exception for Mg alloys, which are precipitation hardenable, however, because of their high cost, these alloys find only limited

applications. Magnesium tin ternary systems, with the additions of other alloying elements have recently attracted research efforts because of their low cost, and superior properties.

The excellent castability of the AZ alloys is attributed to the eutectic nature of the Mg-Al phase diagram. Mg-Sn, being a eutectic diagram as well, can be expected to exhibit good castability [(14)]. The expectation of good castability and precipitation hardening makes the Mg-Sn-based alloys candidates for high-performance cast magnesium alloys. [(14)]

Concerning their use as cast alloys; some major research effort has concentrated on development of Mg-Sn-Ca alloys for creep resistant cast alloys development as a replacement for rare earth metals containing alloys. Hort et al. investigated the Mg-Sn-Ca[(15)] system extensively, with emphasis on creep behavior.Based on this work the Magnesium-tin-calcium system offer a potential to improve the property profile to extend the range of applications for magnesium alloys **[(15)]**. The alloy development was undertaken in accordance to the formation of intermetallic phases during solidification. The ternary Mg-Sn-Ca phase diagram has recently been studied, and assessed by Schmid-Fetzer **[(31)]**. The newly developed ternary Mg-Sn-Ca phase diagram confirmed the presence of ternary CaMgSn phase. Furthermore, the formation of Mg_2Sn or Mg_2Ca phase was expected according to the binary Mg-Sn or Mg-Ca phase diagrams.

The studies showed that Mg-Sn-Ca alloys are able to form several precipitates which can serve as improvement for high temperature stability. These precipitates include a

number of Ca-Sn compounds known from the binary phase diagram, Mg_2Sn, Mg_2Ca, and finally, ternary CaMgSn phase. **[(15)]**·N. Hort et al. **[(32)]** studied the Mg-Sn-Ca system

excessively, and promising results were obtained for some alloys concerning creep resistance, however corrosion resistance was not satisfactory compared to other commercial cast alloys.

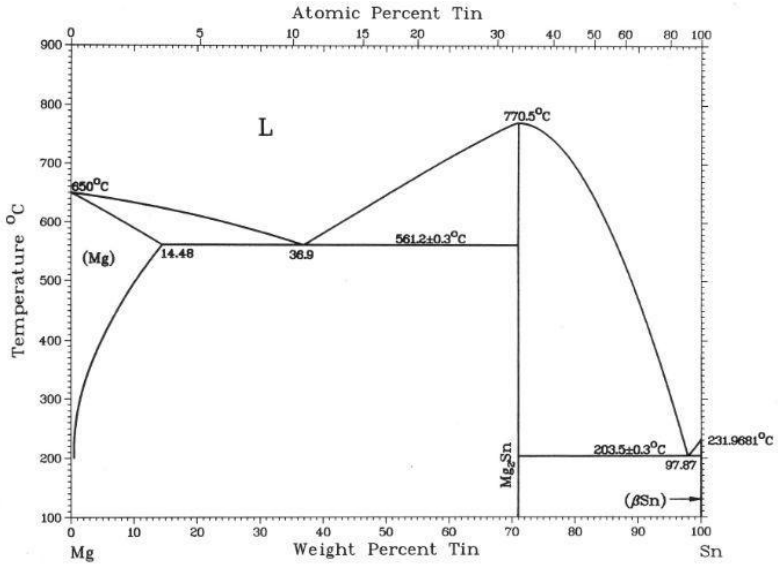

Figure 1.18: Mg-Sn phase diagram [16]

There has been some interest in the Mg-Sn system as early as the 1960's, but only recently that there has been renewed interest, and many studies focusing on magnesium tin alloys. One of the earliest studies has been done by Van Der Planken who studied age hardening behavior of binary Mg-Sn alloys [17]. The investigation reported a peak hardness of Hv = 62 after 100 h aging at 473 K in the Mg–1.65 at.% Sn alloy. Derge et al (40) investigated the orientation relationship between the Mg matrix and the Mg2Sn equilibrium phase using X-ray diffraction and optical microscopy techniques.

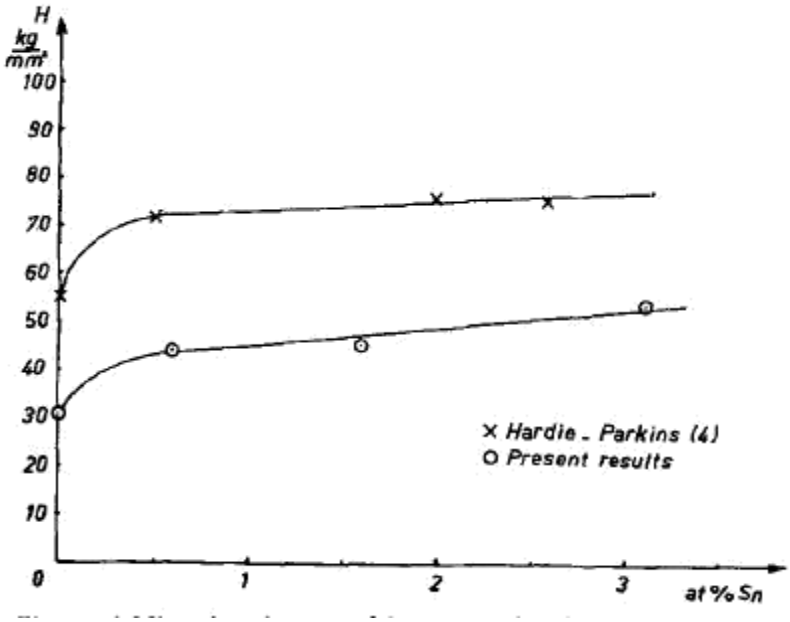

Figure 1.19: Microhardness of homogenized magnesium-tin alloys plotted as a function of tin content (17)

Mendis et al.[41] have examined a Mg-Sn alloy aged at 200 ◦C and using transmission electron microscopy observations, reported that the Mg_2Sn phase forms with a lath-shaped morphology on the (0 0 0 1)Mg basal planes of the matrix with the following orientation relationship: **{**1 1 1**}**Mg2Sn//(0 0 0 1)Mg and <1 1 0>Mg2Sn//<1 1 $\bar{2}$ 0>Mg

There are several patents reported in literature spanning the range between 1931 and 2003. Some of the patents include [18-22]; Mg-Sn-Zn creep resistant alloy with Sn added for castability, Mg-Al-Zn-Sn, a high temperature alloy, and so on. It has been reported in another Japanese patent that the presence of Sn as an alloying element in magnesium is beneficial for strength and creep properties [22].

Concerning research work done in recent years on magnesium tin alloys: Park et al.[43] studied the tensile properties of extruded Mg–Sn–Al –Zn alloy at elevated temperature. They

showed thatl low-temperature superplasticity was found in the alloy, which exhibited tensile elongations of 410–9 50% at low strain rates in the range 1*10-3 to 1*10-4 s at 200°C.

Lui et al. [23] studied the Mg-Sn binary system, and further studied the microstructure, and mechanical properties of permanent- mould cast Mg-5Sn-(0-2.6 wt%) Di alloys [24]; Hasani et al. studied the mechanical properties of hot rolled sheets of a Mg-Sn-Ca alloy at elevated temperature [44]. Kang et al. studied a Mg-Sn-Al-Si die cast alloy [26] ; Cho et al. investigated Mg-Al-Sn alloys for high temperature applications[27]; and , Tang et Al. studied the extruded alloy Mg–5Sn–xZn, and evaluated their mechanical properties. [42]

Concerning age hardening response, Mendis et al. studied the age hardening response in Mg-Sn alloys with additions of zinc [25]; Their study showed that the addition of Zn,and combined addition of (Zn+Na) enhance the age hardening behavior substantially by change in Mg_2Sn particle morphology.

Sasaki et Al studied the effect of Zn additions on enhancing the age hardening behavior of Mg-Sn alloys (38). The Zn additions showed considerable improvement in the age hardening response of Mg-Sn system. The study showed the optimum amount of Zn that caused the largest improvement, and studied the precipitates variants, and microstructure extensively by transmission electron microscopy.

Sasaki et Al. studied the optimization of age hardening behavior of Mg-Sn by Zn microalloying additions, and has developed a high strength Mg-Sn-Zn-Al extruded wrought alloy based on the findings (39).

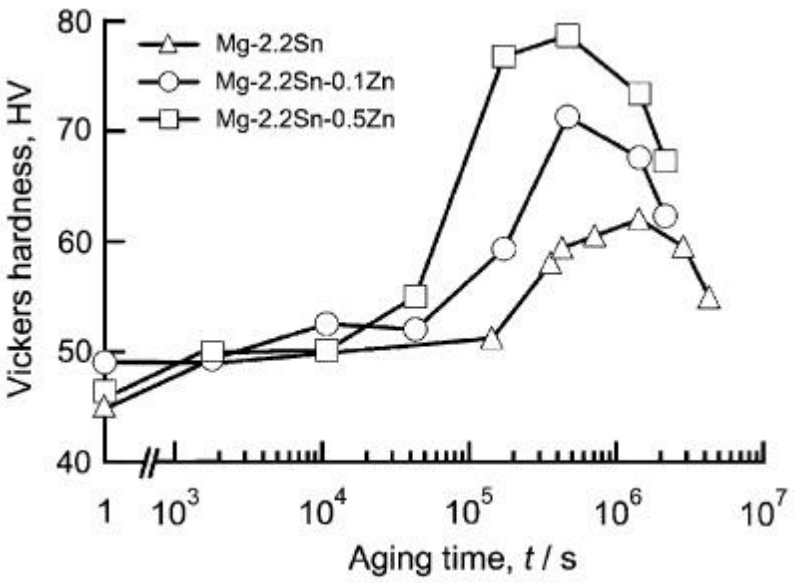

Figure 1.20: Age hardening behavior of Mg-Sn system micro-alloyed with Zn (38)

Also Bamberger et Al [14], based on review of various investigations, compiled a review study on age hardening response of some Mg-Sn alloys, and the microalloying additions selection for the Mg-Sn-X system.

Generally, an enhancement of the age hardening of the Mg-Sn system by further studies is crucial in order to be more competitive to replace the Mg-Al system as the most common alloy series used in wrought Mg alloys industrially.

References

1 K.U. Kainer, "Magnesium Alloys and Technology",Lectures from a workshop of the German Association for Material Science (DGM) in cooperation with the Institute for Material Research at the GKSS Research Center, Geesthacht GmbH, 2003

2 H. E. Friedrich, B. L. Mordike, "Magnesium Technology, Metallurgy, Design Data, Applications", Springer-Verlag Berlin Heidelberg 2006

3 R.E. Brown "Magnesium in the 21st century", ASM Advanced Materials & Processes magazine, January 2009

4 H.Friedrich, S.Schumann; "Strategy to overcome technological barriers to increase use of magnesium in cars" Volkwagen AG, Wolfsburg Germany

5 Al Wrigley, "American Metal Market" march 29, 2002

6 A. Fischerworring-Bunk, C. Landerl, A. Fent, J. Wolf "The New BMW Inline Six-Cylinder Composite Mg/Al Crankcase ", IMA 2005 World Mg Conference, Berlin. Proceedings of the 62nd Annual World Magnesium Conference in Berlin (2005) Intl. Magnesium Assoc., Wauconda, IL USA

7 M. Bauccio "ASM Metals reference book" 3rd edition.

8 Photo courtesy of "US AMP Magnesium Vision 2020" 2006 Report – "A North American automotive strategic vision for magnesium"

9 Photo courtesy of "http://www.gizmag.com/go/4377/picture/13537/"

10 Photo courtesy of "http://greatchange.org/footnotes-1-liter-car.html"

11 M. M.Avedesian, and Baker H.: "Magnesium and Magnesium alloys", ASM speciality Handbook, ASM International Metals Park Ohio, 1999.

12 D. Kevorkov, R.S. Fetzer, "Mg Alloy Database Construction: Investigation of Al-Ca Phase Equilibria", - Magnesium Alloys and their Applications", Kainer K. U. (ed), DGM, Wiley-VCH, Weinheim, 2000, p. 88-91.

13 E. F. Emely ; " Principles of Magnesium Technology " Oxford, Pergamon press,1966

14 M. Bamberger, and G. Dhem "Trends in the Development of New Mg alloys", Annual Review of Materials Research 2008, p. 505-533

15 N.Hort, Y. Huang, T. Abu Leil, P. Maier, K. U. Kainer "Microstructural Investigations of theMg-Sn-xCa System" Advanced Engineering Materials 2006, Vol.8 no.5, p.359-364

16 A. A. Nayeb-Hashemi, J. B. Clark, "Phase diagrams of binary magnesium alloys", eds., ASM International, Metals Park, USA, Ohio, 1998.

17 J. Van Der Planken,"Precipitation Hardening in Magnesium- Tin Alloys" J. Mater. Sci. 4 (1969) p. 927–929

18 R.T Wood., American Magnesium Corp. USA patent US 1831987, 1931

19 R.T Wood., and H.R. Block, American Magnesium Corp., British patent GB380669, 1932

20 S. Schumann,Von Buch, B. Bronfin ,Volkswagenwerk AG and Dead Sea Magnesium, European patent EP1308531, 2003

21 T. Uchinda, T. Abe, T. Hirane , Hitachi Ltd., European Patent EP1108799,2001

22 T. Horie, Toyota Central Research and Development Lab Inc. Japan Patent JP7003374, 1995

23 H. Liu , Y. Chen, Y. Tang , S. Wei, G. Niu "The microstructure, tensile properties, and creep behavior of as-cast Mg–(1–10) %Sn alloys", Journal of Alloys & Componds Vol.440, (2007) p.122-126

24 H. Liu , Y. Chen, Y. Tang , D. Huang, G. Niu "The microstructure and mechanical properties of permanent-mould cast Mg–5 wt. %Sn–(0–2.6) wt. %Di alloys" Materials Science and Engineering A Vol. 437 (2006) p.348–355

25 C.L. Mendis, C.J. Bettles, M.A. Gibson, C.R. Hutchinson "An enhanced age hardening response in Mg–Sn based alloys containing Zn " Materials Science and Engineering A Vol. 435–436 (2006) p.163–171

26 D. H. Kang, S.S. Park, N. J. Kim. "Development of creep resistant die cast Mg– Sn–Al–Si alloy" Materials Science and Engineering A Vol. 413–414 (2005) p. 555–560

27 W. C. Cho, Y. J. Chung, and K. S. Shin " Microstructure and High temperature Mechanical Properties of Mg-Al-Sn Alloys"- Proceedings of the 7th International Conference on Magnesium Alloys and Their Applications

28 W.W Park, I.S Chung, B.S You, "Suppression of Magnesium oxidation by Calcium addition" Proc. 2nd Israel Int`l Conf. On Magnesium science and Technology, MRI, Dead Sea Isreal 2000, p. 377-384.

29 K. Kubota, T. Ojiro, R. Ninomiya, "Improved Heat Resistance of Mg-Al alloys by calcium addition" Acta Mat. Vol 43, 1995, p.669-674

30 Y. Lee , A. K. Dahle, D. H. StJohn, "Grain Refinement of Magnesium", Magnesium Technology 2000,TMS, Nashville, Tennessee 2000, p. 211-218.

31 J. Gröbner, A. Kozlov, M. Hampl, R. Schmid-Fetzer, "Phase formation in Mg-Sn alloys modified by Ca and Ce", Magnesium 2006, Proceeding of the 7th international conference on magnesium alloys and their applications, ed. K.U. Kainer, Wiley-VCH, Weinheim, Germany, 2006, p.32-36.

32 N. Hort, K. P. Rao, T. Abu Leil, H. Dieringa, V.Y.R.K. Prasad and K.U. Kainer "Creep and hot working behavior of a new magnesium alloy Mg-3Sn-2Ca" Proceedings of Magnesium Technology 2008, The Minerals, Metals & Materials Society (TMS) annual meeting, 2008 p.401-406

33 W. D. Callister, "Materials Science and Engineering: An Introduction", 5th edition, John Wiley and sons.

34 ASTM G5-82 " Standard Reference Test Methods for making potentiostatic and potentiodynamic Anodic Polarization Measurements" ASTM international, West Conshohocken, PA, 2003, www.astm.org

35 ASTM B117 -07a G85 "Standard Practice for Operating Salt Spray (Fog) Apparatus" ASTM international, West Conshohocken, PA, 2003, www.astm.org

36 ASTM E92-82(2003) e2. "Standard Test Method for Vickers Hardness of Metallic Materials" ASTM International, West Conshohocken, PA, 2003, www.astm.org

37 T. Abu Leil "Development of New Magnesium Alloys for High Temperature Applications" Doctoral thesis, 2009, TU Clausthal

38 T. Sasaki, K. Oishi, T. Ohkubo, and K.Hono, “E nhanced age hardening response by the addition of Zn in Mg–Sn alloys, Scr ipta Materialia Vol 55 2006 p.251-254

39 T.Sasaki, K.Yamamoto, T.Honma, K. Hono, “A high -strength Mg–Sn–Zn– Al alloy extruded at low temperature” Scripta Mater ialia Vol 59 2008 p.1111-1114

40 G. Derge, A.R. Kommell, R.F. Mehl, Trans. AIME 124 (1937) 367.

41 C. L. Mendis; C. J. Bettles; M. A. Gibson; S. Gorsse; C. R. Hutchinson, "Refinement of precipitate distributions in an age-hardenable Mg-Sn alloy through microalloying" Philos.Mag. Lett Vol. 86, No. 7, July 2006, 443–456

42 W.N. Tang , S.S. Park , B.S. You "Effect of the Zn content on the microstructure and mechanical properties of indirect-extruded Mg–5Sn–xZn alloys" Materials and Design vol.32 2011 pp. 3537-3543

43 S.S. Park, and B.S. You, "Low-temperature superplasticity of extruded Mg–Sn– Al–Zn alloy" Scripta Materialia, Vol 65 2011 p.202-205

44 G.H. Hasani, R. Mahmudi, "Tensile properties of hot rolled Mg-3Sn-1Ca alloy sheets at elevated temperatures" Materials and Design vol.32 2011 pp. 3736-3741

45 K. Hono , C.L. Mendis, T.T. Sasaki, K. Oh-ishi “Towards the development of heat-treatable high-strength wrought Mg alloys” Scripta Mater ialia Vol 63 2010 p.710-715

46 J.F. Nie, X. Gao, S.M. Zhu, Scr. Mater. 53 (2005) 1049–1053.

47 J.C. Oh, T. Ohkubo, T. Mukai, K. Hono, Scr. Mater. 53 (2005) 675–679.

48 S. Celotto, Acta Mater. 48 (2000) 1775–1787

Chapter 2 - Alloy Design

2.1-Macro-Alloying-Effect of Al additions

2.1.1 Introduction

Research towards the development of magnesium alloys for various structural applications is gaining momentum by the lightweight construction trend in the transportation industry. Enhancing the strength levels of magnesium alloys is an important factor for determining whether or not they will be adapted to the industry. Among the various strengthening methods for metallic alloys, precipitation hardening has been widely used as an effective method to increase the strength of various structural alloys specially wrought alloys in the form of sheets, extrusions, and forgings. Nevertheless, precipitation hardening methods have not been investigated fully in structural magnesium alloys, and the available range of precipitation hardenable wrought Mg alloys is still very limited compared to aluminum alloys and steels. However, there has been an increasing interest these days in the research to improve the age hardening response of precipitation hardenable binary alloys such as Mg-Zn **[1,2]**, Mg-Al**[3]** , Mg-Ca**[4,5,6]**, Mg-Sn **[7,8]** and Mg-RE (RE: rare earth element) **[9-11]**.Although Mg-rare earth systems show remarkable age hardening responses and suitable creep resistance, recent issues surrounding rare earth metals such as resource scarcity, limited deposits, and escalating prices are causing the high use of rare earth metals in Mg alloys to become unpractical and undesirable. Tin costs lower than rare earth metals and shows good potential to be used in the development of cost effective heat resistant, and precipitation hardenable RE-free magnesium alloys**[13].**

The Mg-Sn system is a good candidate for precipitation hardening since the solid solubility at higher temperatures is as high as 3.35 at% (equivalent to 14.48 wt.%) at 561°C with a low solid solubility at room temperature at 0.035 at% (0.17 wt%). The phase diagram of the Mg_2Sn system shows the formation of an equilibrium stable phase of Mg_2Sn[12] with

an FCC structure, a=6.76A°, point group $m\bar{3}m$ [12], and a high melting point of ~770°C. The high temperature stability for the Mg_2Sn phase gives the alloys based on Mg-Sn huge potential to be used in higher temperature creep resistant applications [19].

Owing to these properties, there is much potential for the Mg-Sn system to be used in cast and wrought products due to its moderate to high strength, and excellent creep properties. The earliest work on the precipitation hardening of the Mg-Sn system was carried out by Van der Planken [14] on a Mg-1.6Sn (at%) binary alloy at various aging temperatures. However, the hardening response of the alloy was sluggish, and peak hardness that was reported was only about 62 HV since theMg_2Sn precipitates showed low number density, coarse size, and inhomogeneous distribution. More recently, Sasaki et al. [7] and Mendis et al. [8] reported the additions of Zn to Mg-Sn alloys enhanced the precipitation hardening response by the refinement of the precipitates. Further work by Sasaki et al [17] demonstrated that 1at%Al additions in a ternary Mg-2.2Sn-0.5Zn alloy led to a substantial enhancement of the hardening response. The extruded Mg-2.2Sn-1.0Al-0.5Znalloy showed low yield anisotropy with a yield strength comparable to Mg-Zn and some Mg-RE alloys [20].Although this work has shown the addition of 1.0at.%Al to Mg-.2.2Sn-0.5Zn cause enhancement of age hardening, the composition of Al has not been optimized. Hence, a systematic study of the Al additions on the ageing behavior of Mg-Sn system is valuable.

In this study the effect of systematic addition of Al and various microalloying elements to Mg-2.2 at% Sn alloy on the microstructure and age hardening response was investigated in order to explore the optimized composition with the highest age hardening response in Mg-Sn based alloys.

2.1.2Experimental

Alloy ingots were prepared by induction melting high purity magnesium, tin, aluminum and other alloying elements using steel crucibles under an argon atmosphere and by casting

into steel molds. Binary Mg-2.2Sn, ternary Mg-2.2Sn-(0.5,1,2,3,4)Al, and quaternary Mg-2.2Sn-3Al with various elements as microalloying additions (Ca, Ag, Zn, Cu, Mn, and their combination) were obtained (compositions in at%).In this paper, the all alloy composition are shown in at.%. The compositions of all the alloys used in this study are summarized in both at.% and wt% in Table 1.The ingots were homogenized at 500°C for 48 h in a He-filled Pyrex tube. Then small discs were cut from the ingots, solution heat treated for 1 h at 525°C in He-filled Pyrex tubes and water quenched. Samples were aged immediately after quenching in water. The aging heat treatment was carried out at 200°C in a silicone oil bath. The hardness values were measured by a micro Vickers hardness tester under a load of 0.5 kg, and were recorded as an average of minimum 8 measurements. Thin foil specimens for TEM observations were prepared by punching 3 mm diameter discs, mechanical polishing, twin-jet electro-polishing in a solution of 15.9 g LiCl, 33.48 g $Mg(ClO_4)_2$, 300 ml 2-butoxy-ethanol and 1500 ml methanol at(-45°C) at a voltage of 90 V, as well as ion milling using Gatan PIPS Precision Ion Polishing System Model 691 at room temperature. The microstructure characterization was carried out by transmission electron microscopy (TEM) using a FEI Tecnai 20 TEM operating at 200 kV, and the EDX measurements were performed using a field-emission scanning electron microscope (Carl Zeiss CrossBeam 1540EsB) using a TEM specimen mounted on special TEM specimen holder.

2.1.3 Results

The age hardening behavior of the binary Mg-2.2Sn, and the ternary Mg-2.2Sn-*x*Al alloys as a function of aging time at 200°C is shown in Fig.1. The hardness values of the as solution treated samples are all close ranging from ~43 ±6 HV in the binary alloy, to44± 1.2 HV in Mg-2.2Sn-2Al, and up to 49±2, HV and 51±3HV in the Mg-2.2Sn-3Al, and Mg-2.2Sn-4Al alloys, respectively.

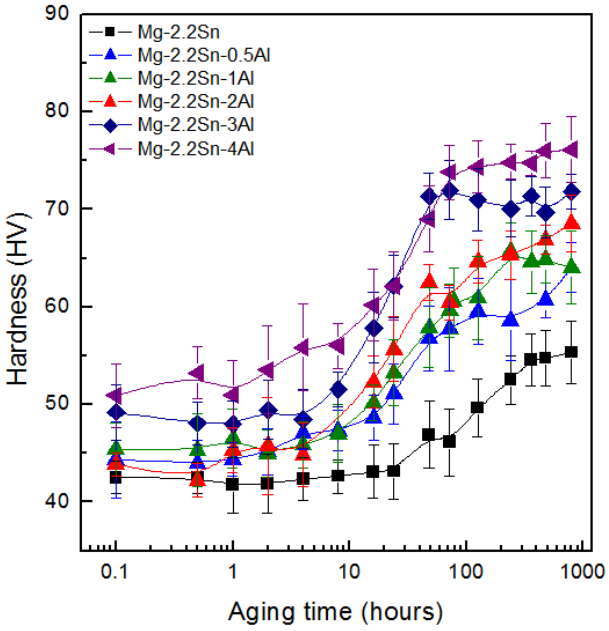

Figure 1: Age hardening behavior of various ternary Mg-2.2Sn-(0-4 at%)Al alloys at 200^{o}C

The Al additions increased the peak hardness substantially as shown in the figure. The peak hardness of the Mg–2.2Sn–4Al alloy was the highest among the ternary alloys with HV = 76±3, but was not much higher than in Mg-2.2Sn-3Al, and took longer time to reach peak age than the Mg-2.2Sn-3Al alloy which reached the peak hardness value of ~72±2.2 HV in the shortest time period of about 72h while the binaryMg-2.2Sn binary alloy took more than 360h to reach its peak hardness. The increment of the peak hardness in the Mg-2.2Sn-3Al alloy is ~23 HV, compared to about 10 HV in the Mg–2.2Sn binary alloy. A rapid increase in hardness was observed in the Mg–2.2Sn–3Al alloy after 6h, while the binaryMg-2.2Sn binary alloy took more than 360h to reach its peak hardness. Such rapid increase in hardness at early stages of aging was not apparent in the binary Mg-2.2Sn alloy.

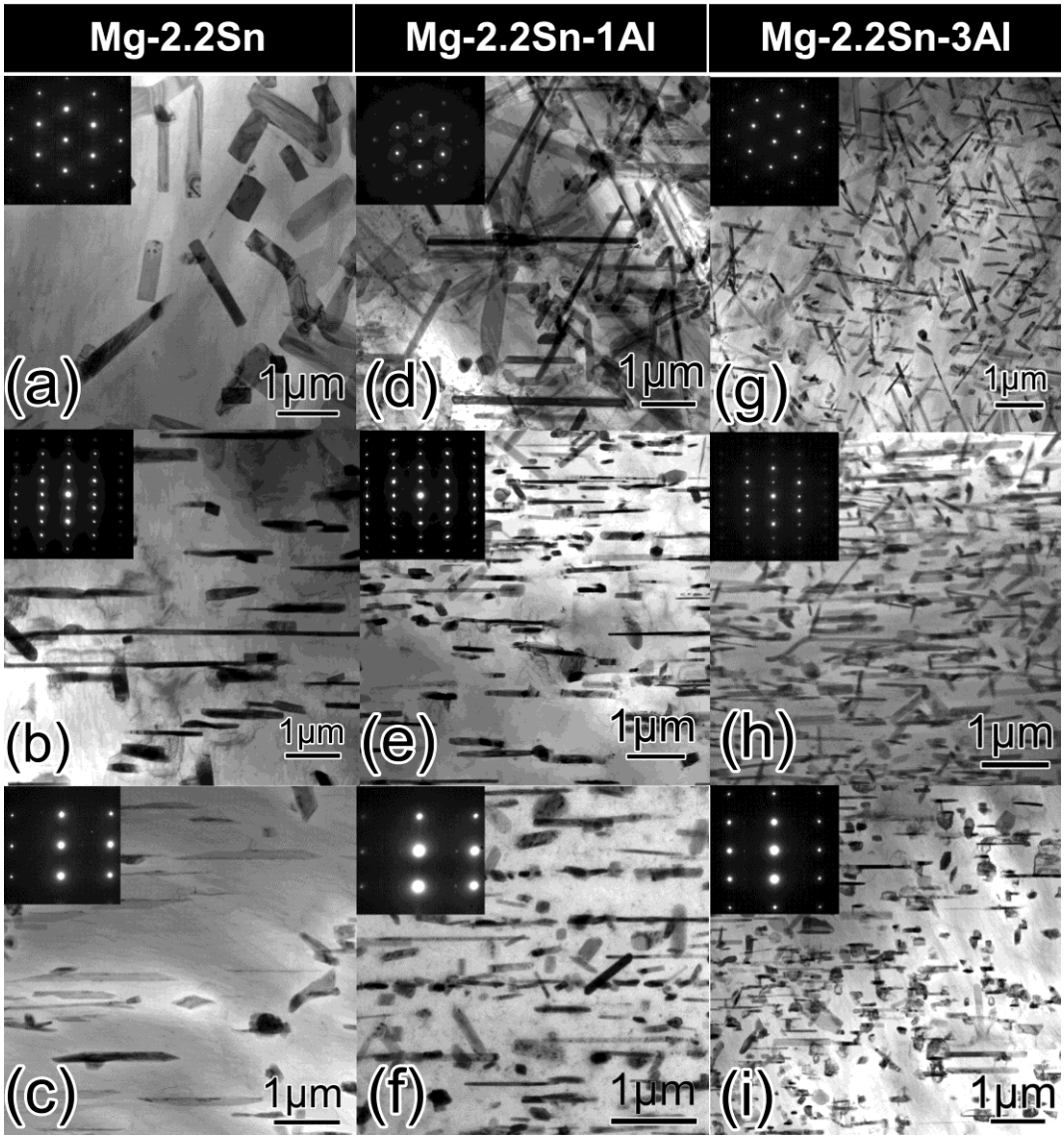

Figure 2: TEM bright field images of the peak-aged (a)-(c) Mg–2.2Sn at 200^{o}C (d)-(f) Mg–2.2Sn–1Al, and (g)-(i) Mg–2.2Sn–3Al alloys. Electron beam is parallel to (a, d,g) [0001], (b,f h) $<11\bar{2}0>$, and (c,f,i) $<10\bar{1}0>$ zone axis

Fig.2 shows the microstructures of the peak aged Mg-2.2Sn, Mg-2.2Sn-1Al, and Mg-2.2Sn-3Al alloys at 200°C. The TEM bright field micrographs, Fig. 2 (a)-(c), show the microstructure of theMg-2.2Sn alloy along the [0001], $<11\bar{2}0>$, and $<10\bar{1}0>$ zone axes. The microstructure consists of 2 types of precipitate morphologies, i.e., plate like and lath/rod like precipitates. The habit plane of the plate-like precipitates is the (0001) basal plane, with

growth in the<$11\bar{2}0$> direction. The precipitates are coarse with a size of ~1.6μm and show a heterogeneous distribution. Fig. 2 (d)-(f) show the bright field TEM images of the Mg-2.2Sn-1Al ternary alloy along the [0001],<$11\bar{2}0$>, and <$10\bar{1}0$> zone axes. The size of the precipitates is much finer than that of the binary alloy with a more uniform distribution. The average precipitate size was ~1.4 μm., and most of the precipitates show have basal (0001) habit plane with growth in the<$11\bar{2}0$> direction. The refined precipitate size and the increased homogeneity of dispersion can explain the increase of about~10HV in the hardeness of the ternary alloy compared to the binary alloy. Figure 2 (g)-(i) show the bright field TEM images of the Mg-2.2Sn-3Al ternary alloy along the [0001], <$11\bar{2}0$>, and<$10\bar{1}0$> zone axes. The addition of more aluminum in the Mg-2.2Sn-3Al alloy caused a further refinement in the precipitate size. The refinement is evident by the reduction in the average precipitate size to~0.6 μm. Most of the precipitates lie on the basal (0001) plane in the <$11\bar{2}0$> direction as in the Mg-2.2Sn-1Al alloy, although some of the precipitates have growth directions deviating from the <$11\bar{2}0$> direction as shown in Fig. 2(g). In addition, the <$11\bar{2}0$>, and<$10\bar{1}0$> zone axes bright field images, Fig.2 (h, i), indicate that non-basal precipitates appear more frequently in the Mg-2.2Sn-3Al alloy compared with the binary, Fig 2 (b,c).

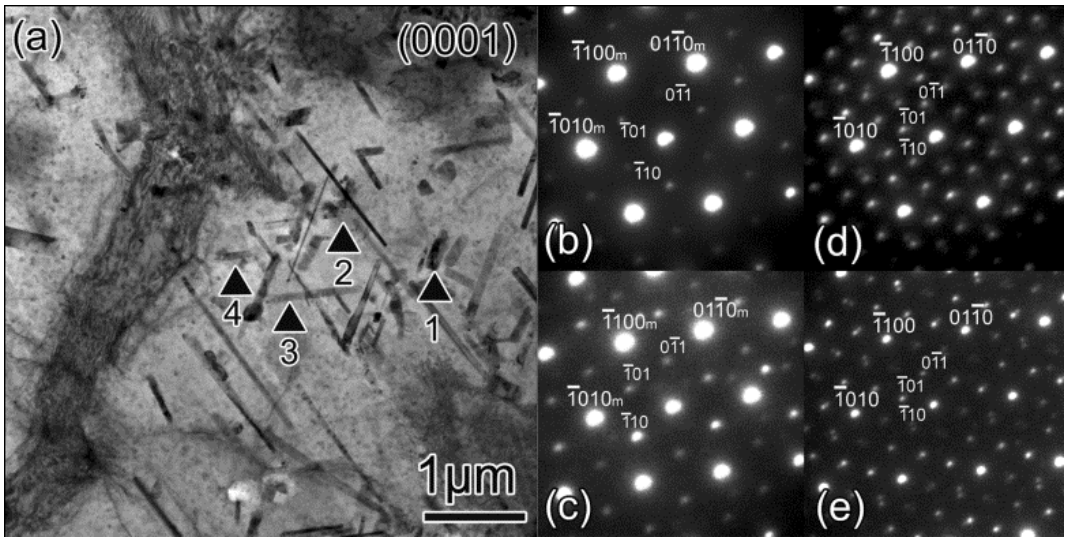

Figure 3: Bright field TEM image and selected area diffraction patterns represented by arrows (a,b): Mg_2Sn, (c,d) $Mg_{17}Al_{12}$ precipitates e of the peak-aged Mg–2.2Sn–3Al (at%) alloy at 200^{o}C along the [0001] zone axis

Fig.3 (a) shows the bright field TEM image of the peak aged Mg-2.2Sn-3Al alloy at 200°C. The image was taken along the [0001] zone axis. Fig.3(b) and (c) show the selected area electron diffraction (SAED) patterns of precipitates no.1 and 2 indexed as the Mg_2Sn phase. The selected area diffraction patterns reveals an orientation relationship (OR) between the magnesium matrix and Mg_2Sn of $(0001)_{\alpha}//\{111\}_{\beta}$, $<11\bar{2}0>_{\alpha}$ // $<\bar{1}01>_{\beta}$. Fig.3(d) and (e) show the SAED patterns from the precipitates 3 and 4 indexed as the $Mg_{17}Al_{12}$ phase with the same orientation relationship (OR) of $(0001)_{\alpha}//\{111\}_{\beta}$, $<11\bar{2}0>_{\alpha}$ // $<\bar{1}01>_{\beta}$. Meanwhile, another $Mg_{17}Al_{12}$ precipitate was identified to have the orientation relationship (OR) between the magnesium matrix and $Mg_{17}Al_{12}$ of $(0001)_{\alpha}//\{1\bar{1}0\}_{\beta}$, $<2\bar{1}\bar{1}0>_{\alpha}$ // $<222>_{\beta}$.

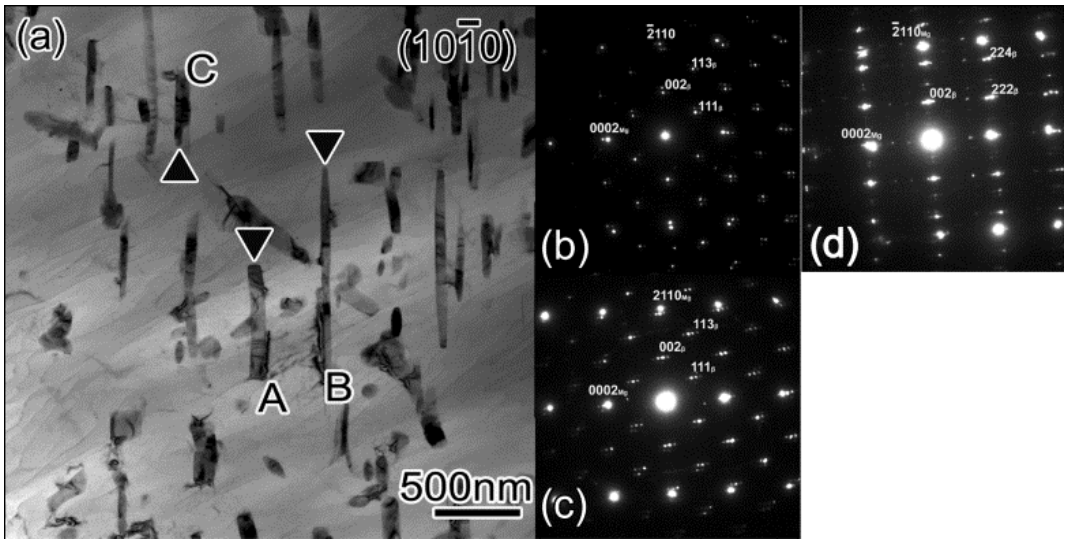

Figure 4: Bright field TEM image and selected area diffraction patterns of precipitates shown in the bright field image of the peak-aged Mg–2.2Sn–3Al (at%) alloy at 200^{o}C along the $<10\bar{1}0>$ zone axis

Fig.4(a) shows a bright field TEM image of the peak aged Mg-2.2Sn-3Al alloy at200°C taken at a higher magnification from the$<10\bar{1}0>$ zone axis. Fig.4 (b) shows the SAED from the lath precipitates shown in the bright field image. The precipitates were identified as the Mg_2Sn phase, and the orientation relationship (OR) between the magnesium matrix, and Mg_2Sn was shown to be: $(10\bar{1}0)_{\alpha}//\{1\bar{1}0\}_{\beta}$, $<2\bar{1}\bar{1}0>_{\alpha}$ // $<002>_{\beta}$.

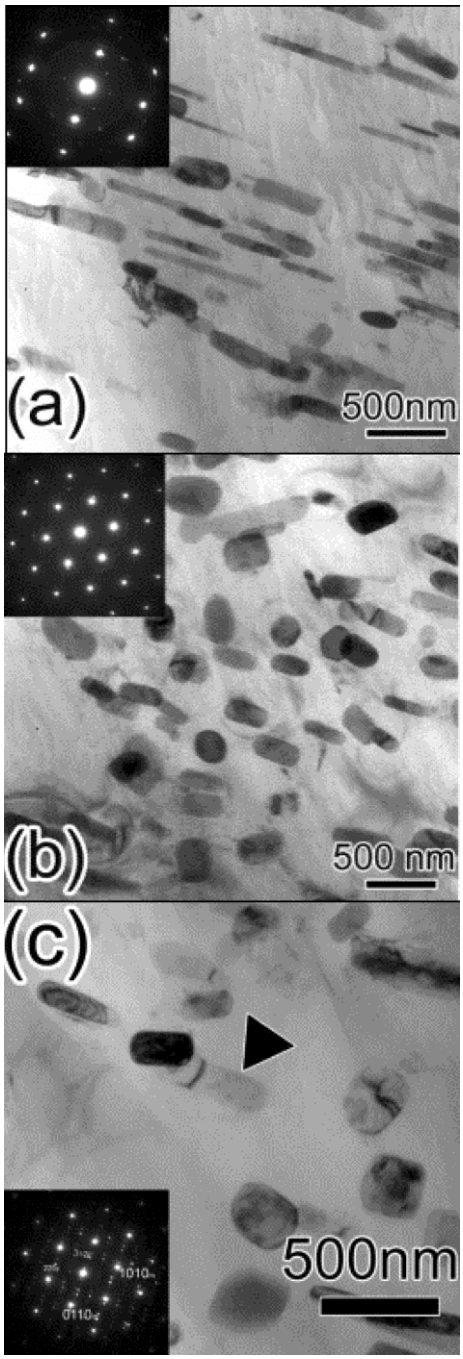

Figure 5:TEM bright field images of 6h aged Mg–2.2Sn–3Al (at%) alloy at 200^{o}C along the (a) $<10\bar{1}0>$, (b) [0001] zone axis, (c) representative selected area diffraction pattern (SADP) of precipitates

Fig.5 shows the TEM microstructure of the ternary Mg-2.2Sn-3Al alloy aged at 200^{o}C for 6h. The 6h period represents the onset of a rapid hardness increase in the alloy as indicated from the age hardening curve in Fig.1. Fig.5 (a) and (b) show the precipitates observed along

the $<10\bar{1}0>$, and <0001> zone axes. The microstructure of the precipitates shows some similarity to that observed in the peak aged condition with a difference in size and morphology as evident from the shape of the aspect ratio of the growing precipitates in Fig.5 (b). The majority of the precipitates are identified as Mg_2Sn while some are indexed as$Mg_{17}Al_{12}$.. Some of these precipitates were found to have an OR of $(0001)_{\alpha}//\{110\}_{\beta}$, $<11\bar{2}0>_{\alpha}$ // $<\bar{1}\bar{1}2>_{\beta}$ with the magnesium matrix, as shown by the selected area diffraction pattern inset in Fig.5c

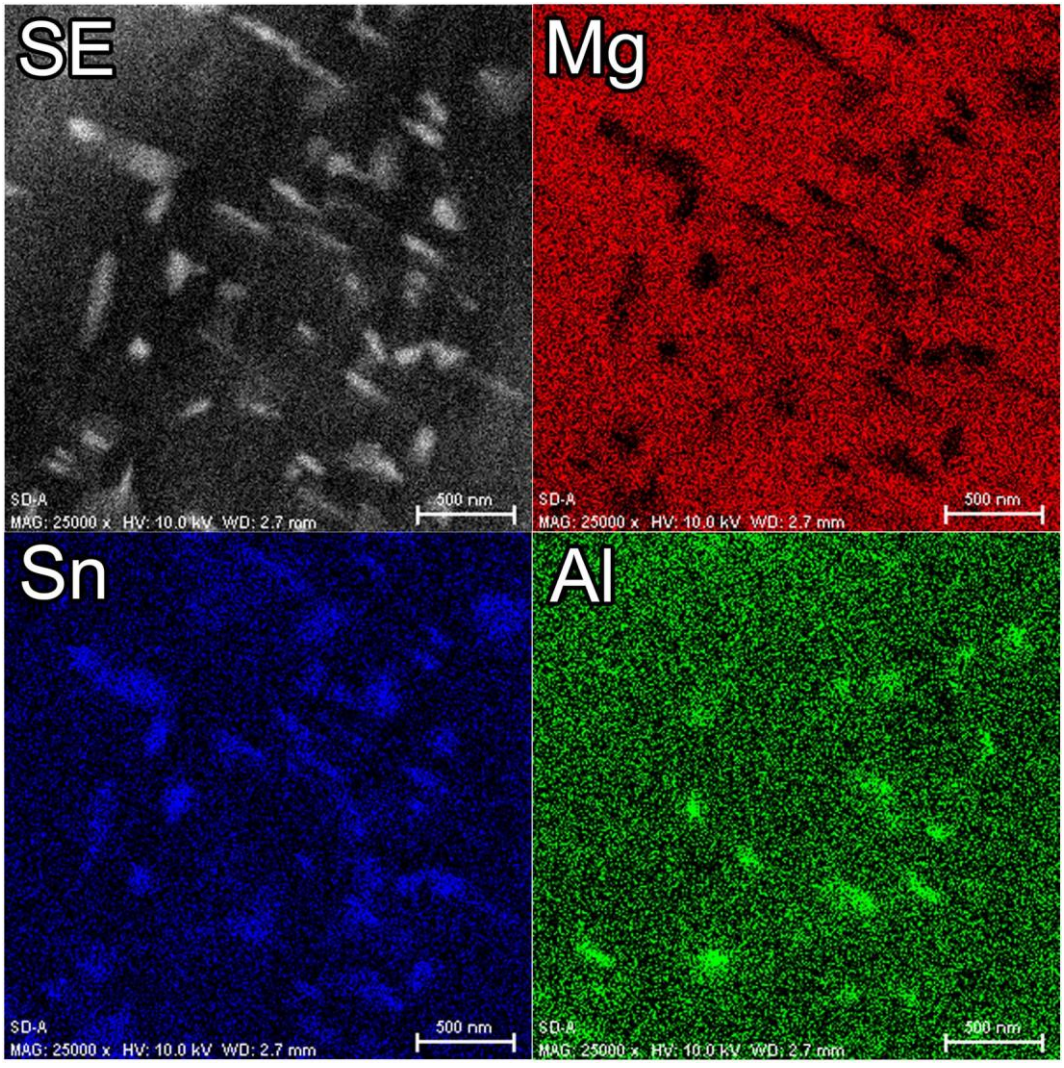

Figure 6: EDX area chemical mapping of peak aged Mg–2.2Sn–3Al (at%) alloy at 200^{o}C,(a) SE image, (b) Mg , (c) Sn, and (d)Al distribution

Fig.6 shows the energy dispersive x-ray spectroscopy (EDXS) area mapping of the peak aged Mg-2.2Sn-3Al alloy (a) SE image,(b) Mg map, (c) Sn map, (d) Al map. The Sn map in Fig.6(c) shows that the Sn concentration is very high at the precipitate sites where the precipitates were identified as Mg_2Sn. The Al rich regions on the Al map, Fig 6 (d) do not correspond to areas rich in Sn , Fig 6 (c). This confirms that there are no ternary precipitate phase found in this alloy.. So we conclude that there are only two types of precipitates, Mg_2Sn and $Mg_{17}Al_{12}$.

2.1.4 Discussions

Based on the expected positive effects of Al additions, and the micro alloying approach, as reported by Sasaki et al. **[17]** this work offered a systematic study on the precise effects of Al additions in different compositions on the age hardening response of the Mg-2.2Sn alloy. The age hardening behavior of Mg-2.2Sn alloys with the additions of 0.5, 1, 2, 3, and 4 at% Al were investigated and the microstructures of the Mg-2.2Sn,Mg-2.2Sn-1Al, and Mg-2.2Sn-3Al were examined to explain the effect of ternary aluminum additions on the precipitate morphology, size, and distribution. Al additions were found to have a positive effect on the precipitation hardening response increasing the hardness by about 17 HV compared to the binary Mg-2.2Sn alloy, and overall increment of 24 HV compared to the solution treated (T4) condition. Moreover the time to peak age was reduced significantly compared to the binary alloy, which is indicative of enhanced kinetics of precipitation as revealed by the substantially faster time to peak age of 72h instead of more than~600h to reach peak age for the binary alloy.

Most of the precipitates form on the (0001) basal habit plane which is typical of the Mg-Sn system with the $<11\bar{2}0>$ growth direction. An increase in the occurrence of non-basal precipitates with an increase in Al content is also evident from Fig. 2.The precipitates were shown to be mainly basal precipitates of the Mg_2Sn phase which have the

following OR with the Mg matrix: $(0001)_{\alpha}//\{111\}_{\beta}$, $<11\bar{2}0>_{\alpha}$ // $<\bar{1}01>_{\beta,}$ and

$\{10\bar{1}0\}_{\alpha}//\{1\bar{1}0\}_{\beta}$, $<2\bar{1}\bar{1}0>_{\alpha}$ // $<002>_{\beta.}$ This is consistent with the previously reported results **[7, 21, 22]**. This indicates that there is no change in terms of the nature of the precipitate phase, and that the main change is the refinement in the size and distribution of the main strengthening Mg_2Sn phase.Another type of precipitate was the $Mg_{17}Al_{12}$ phase (BCC structure, a=10.6A°, space group $I\bar{4}3m$) and were indexed to have the following OR with the

Mg matrix: $(0001)_{\alpha}//(110)_{\beta}$, $[11\bar{2}0]_{\alpha}$ // $[1\bar{1}2]_{\beta}$. .The OR is also consistent with the previously reported one for the $Mg_{17}Al_{12}$ phase in Mg-Al alloys **[4]**.The Mg-2.2Sn-3Al alloy was selected for a further optimization study on age hardening responses since it showed a faster peak aging time than that of Mg-2.2Sn-4Al.

2.1.5 Summary and Conclusions

The aluminum additions had a significant effect on the peak hardness values and the time to reach peak hardness. The increment in the hardening response was about 23HV in the ternary Mg-2.2Sn-3Al, and about~36HV in the quaternary Mg-2.2Sn-3Al-0.5Zn. These values are comparable to those of ternary Mg-2.2Sn-0.5Zn**[7]** and quaternary Mg-2.2Sn-0.5Zn-1Al **[17]**reported by Sasaki et al.

The mechanism of Al enhancing the age hardening response of Mg-Sn system might be (i) chemical in nature by changing the interfacial energy between Sn, and the Mg matrix, (ii) Al additions may cause a reduced solid solubility of Sn, thereby increasing the driving force for the precipitation, (iii) $Mg_{17}Al_{12}$ precipitates which may have acted as heterogeneous nucleation sites enhancing the Mg_2Sn precipitation.

2.2-Micro-Alloying

2.2.1 Results and Discussions

Microalloying elements were selected based on two main strategies to further enhance the possible strength level. The first is to use elements with negative enthalpy of mixing with Sn (−ΔH), which are thermodynamically more prone to co-segregate with the main alloying elements. The second is to use elements with positive enthalpy of mixing with Sn (+ΔH), which tend to be rejected by Sn and not segregate or form intermetallic compounds with the main solute elements. Both strategies have been successful on the ternary alloying scale in previous studies on Mg-Zn**[2]**, and Mg-Sn systems **[7,17]**. In this study Ca, Ag, and Mn are the elements which have a negative enthalpy of mixing with Sn, and Cu and Zn are the elements with a positive enthalpy of mixing with Sn.

Fig. 7 shows the age hardening behavior of various quaternary Mg-2.2Sn-3Al-X alloys aged at 200^{o}C. Different microalloying elements consisting of 0.1-0.5at%Ca, Cu, Ag, and Zn were added to the optimized composition of the ternary Mg-2.2Sn-3Al alloy for the reasons described in the discussion. Fig.7 (a) shows the age hardening response of the Mg-2.2Sn-3Al ternary alloy, along with quaternary alloys containing (0.1Ca, 0.1Cu, 0.1Ag, and 0.1Zn) micro-alloying additions. A maximum hardness of around~76HV was exhibited by the additions of 0.1Ca, 0.1Ag, 0.1Mn at%.. Fig.7 (b) shows the aging response from the additional microalloying elements, i.e., Ca, Zn, Mn, Ag, and the combined additions of some of these elements to the ternary Mg-2.2Sn-3Al alloy. A maximum hardness of ~81HVwas obtained in the Mg-2.2Sn-3Al-0.5Zn alloy, at 200^{o}C.

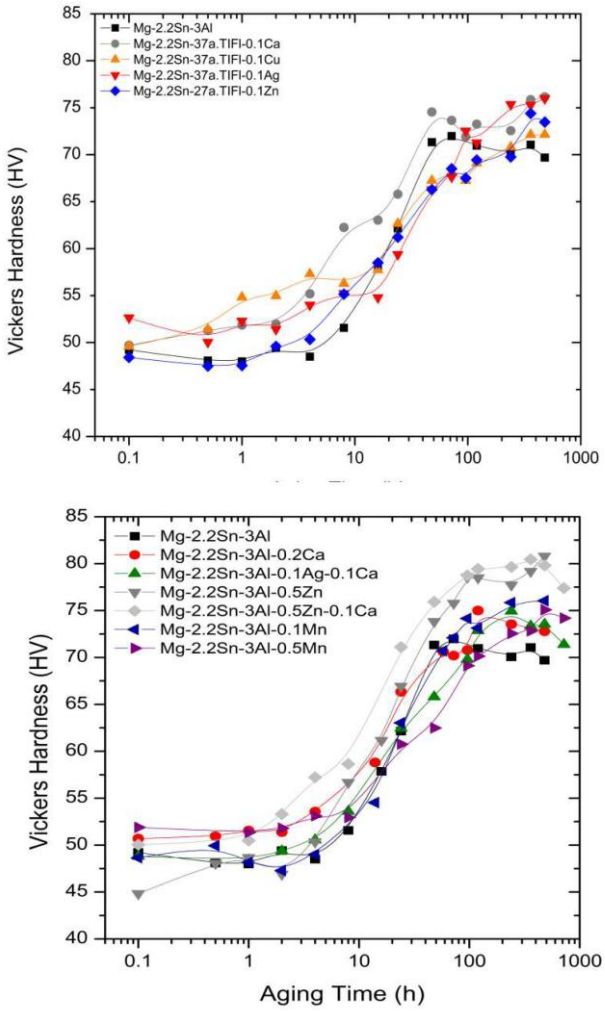

Figure 7: Age hardening behavior of various quaternary Mg-2.2Sn-3Al –X alloys at 200^{o}C

As shown in Fig. 7, Mg-2.2Sn-3Al-0.5Zn showed the highest hardness value among the age hardening responses of the various microalloyed compositions. Its microstructure showed the existence of the Mg_2Sn phase with the (0001) habit plane with a refined dispersion compared to that of the ternary alloy. Its precipitate size was substantially finer compared to that of the binary and ternary alloys. The precipitate length of the Mg-2.2Sn-3Al alloy was about ~65% compared to that of the binary Mg-2.2Sn alloy. Meanwhile, the average precipitate length of the Mg-2.2Sn-3Al-0.5Zn quaternary alloy was refined to about ~32% compared to that of the ternary Mg-2.2Sn-3Al alloy, and about ~76% overall compared to that of the base Mg-2.2Sn binary alloy.

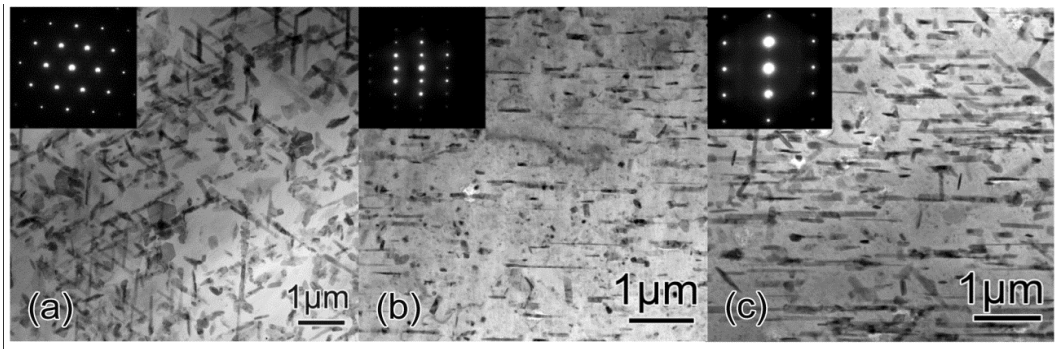

Figure 8: TEM bright field images of the peak-aged Mg–2.2Sn–3Al-0.5Zn alloy at 200^{o}C along (a) [0001] (b) $<11\bar{2}0>$, and (c) $<10\bar{1}0>$ zone axis

Fig.8 shows the bright field TEM images of the peak aged microstructure of the quaternary Mg-2.2Sn-3Al-0.5Zn alloy at 200^{o}C along (a) [0001], (b) $<11\bar{2}0>$, and (c) $<10\bar{1}0>$zone axes. The micrographs reveal the same kind of overall precipitate morphology in the form of Mg_2Sn lath and plate like precipitates that are similar to those of the ternary Mg-2.2Sn-3Al alloy. As in the ternary Mg-2.2Sn-3Al alloy, the majority of the precipitates form on the habit plane of (0001), with a $<11\bar{2}0>$ growth direction. However, there is an increased number of non-basal precipitates, and the micrographs show a further refinement of the precipitate size to about 0.38μm (380 nm) as well as a more homogenous dispersion of the precipitates.

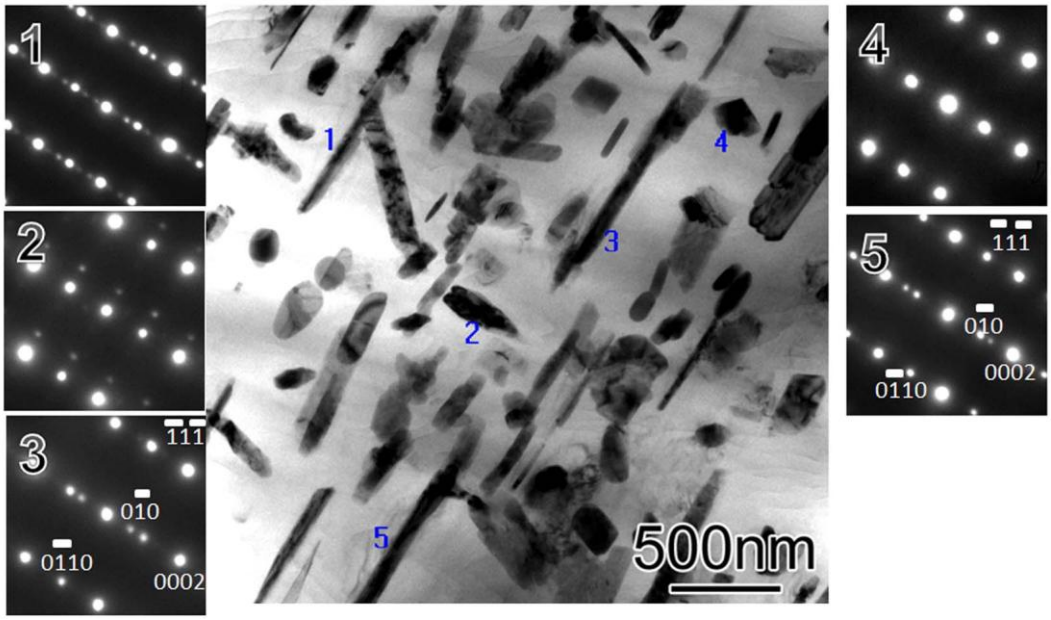

Figure 9 Bright field TEM image of the peak aged Mg-2.2Sn-3Al-0.5Zn alloy at 200^{o}C along $<11\bar{2}0>$ZA with SAD patterns from select precipitates

Fig.9 shows the bright field TEM images of the peak aged microstructure of the quaternary Mg-2.2Sn-3Al-0.5Zn alloy at 200^{o}C along $<11\bar{2}0>$, and corresponding SAD selected area diffraction patterns from select precipitates indexed as Mg_2Sn with similar morphology in the form of Mg_2Sn lath and plate like precipitates to the ternary Mg-2.2Sn-3Al alloy

2.2.2 Summary and Conclusions

The Zn micro-alloying additions might have a similar nature regarding the chemical change of interfacial energy, as both Al and Zn maintain a positive enthalpy of mixing ($+\Delta H$) with Sn atoms. The occurrence of $MgZn_2$ might possibly enhance the Mg_2Sn precipitation process, but was not identified in the quaternary alloy in this study.

The combined additions of aluminum, and microalloying with Zn enhanced the age hardening response of Mg-Sn alloys. The optimized alloy composition is Mg-2.2Sn-3Al-0.5Zn(at.%) or Mg-9.8Sn-3.0Al-1.2Zn (wt.%), i.e., TAZ1031. The mechanism of this is the substantial refinement of the precipitate microstructure consisting of mainly Mg_2Sn and minor $Mg_{17}Al_{12}$. Low cost elements such as Al and Zn can play a major role in enhancing the precipitation hardening and kinetic of Mg-Sn alloys and this may lead to a wider range of heat treatable Mg wrought alloys.

The age hardenable Mg-2.2Sn-3Al-0.5Zn alloy that was developed in this study may be a suitable alloy for extrusion, since this system can be extruded at a lower temperature than the other Mg alloys such as Mg-Zn based alloys as previously reported **[20,23-26]**. This allows for the possibility of obtaining higher strength due to grain refinement caused by the dynamic precipitation processes during extrusion. Also the solid solution strengthening effect from increased Al addition which is apparent from higher as-quenched hardness values of the alloy, might also enhance the total strength level achievable by the alloy.

References

[1] J.B. Clark, Acta Metall. 13 (1965) 1281–1289.

[2] C.L. Mendis, K. Oh-ishi, K. Hono, Scripta Mater. 57 (2007) 485–488.

[3] J.B. Clark, Acta Metall.16 (1968) 141–152

[4] S. Celotto, Acta Mater. 48 (2000) 1775–1787.

[4] J.F. Nie, B.C. Muddle, Scr. Mater.37 (1997) 1475–1481.

[5] J.C. Oh, T. Ohkubo, T. Mukai, K. Hono, Scr. Mater. 53 (2005) 675–679.

[6]K. Oh-ishi, R.Watanabe, C.L. Mendis, K. Hono, Mater. Sci. Eng. A 526 (2009) 177–184

[7] T.T. Sasaki, K. Oh-ishi, T. Ohkubo, K. Hono, Scr. Mater. 55 (2006) 251–254.

[8] C.L. Mendis, C.J. Bettles, M.A. Gibson, C.R. Hutchinson, Mater. Sci. Eng. A 435 (2006) 163–171.

[9] J.F. Nie, X. Gao, S.M. Zhu, Scr. Mater. 53 (2005) 1049–1053.

[10] B. Smola, I. Stulikov. a, F. von Bush, B.L. Mordike, Mater. Sci. Eng. A 324 (2002) 113–117.

[11] D.H. Ping, K. Hono, J.F. Nie, Scr. Mater.48 (2003) 1017–1022.

[12] Nayeb Hashemi A.A., and Clark J.B., Mg-Sn (Magnesium-Tin), Binary Alloy Phase Diagrams, II Ed., Ed. T.B. Massalski, Vol. 3, 1990, p 2549-2552.

[13] N. Hort, Y.D. Huang, T. Abu Leil, P. Maier, K.U. Kainer, Adv. Eng. Mater. 8 (2006) 359–364.

[14]K. Van der Planken, J. Mater. Sci. Lett.. 4 (1969) 927–929

[15] C.L. Mendis, C.J. Bettles, M.A. Gibson, S. Gorsse, C.R. Hutchinson, Philos. Mag. Lett. 86 (2006) 443–456

[16] M.Bamberger, G.Dehm, Annu. Rev. Mater. Res. 38 (2008) 505-533

[17] T.T. Sasaki, K. Oh-ishi, T. Ohkubo, K. Hono, Mater. Sci. Eng. A 530 (2011) 1–8

[18] P.Villars, L.D. Calvert, Pearson's Handbook of Crystallographic Data for Intermetallic Phases, ASM International, Materials Park, 1991.

[19] A.L. Bowles, H. Dieringa, C. Blawert, N.Hort, K.U. Kainer, Mater. Sci.Forum 488/489(2005) 135.

[20] T.T. Sasaki, K. Yamamoto, T. Honma, S. Kamado and K. Hono, Scr. Mater. 59 (2008) 1111–1114

[21] G. Derge, A.R. Kommell, R.F. Mehl, Trans. AIME 124 (1937) 367.

[22] S. Henes, V. Gerold, Z. Metallkunde 53 (1962) 743

[23] S.S. Park, and B.S. You, Scr. Mater. 65 (2011) 202–205

[24] S.S. Park, W.N. Tang, B.S. You, Mater. Lett. 64 (2010) 31–34

[25] W.L. Cheng , H.S. Kim , B.S. You , B.H. Koo , S.S. Park, Mater. Lett. 65 (2011) 1525–1527

[26] C.L. Mendis, K. Oh-ishi, Y. Kawamura, T. Honma, S. Kamado, K. Hono, Acta Mater. 57 (2009), 749-760.

[27] E. Doernberg, A. Kozlov, and R. Schmid-Fetzer, J. Phase Equilib. Diffus.28 (2007) 523-535

Chapter 3 - Na microalloying effect

3.1 Introduction

There are several reports on the effect of microalloying on the precipitation hardening. Sasaki *et al.* [1] reported the microalloying of Zn substantially improved the age hardening response of the Mg-Sn based alloys. Mendis *et al.* reported the trace addition of Na to Mg-Sn-Zn alloy further enhanced the age hardening response including the precipitation kinetics [2]. However, since the maximum hardness in the Mg-Sn based alloy was only ~85HV, which is much lower than that of the microalloyed Mg-Zn (95HV at 160°C) and Mg-Al-Zn alloys (100HV at 100°C) [3,4], further improvement of the hardening response is required to make the Mg-Sn system industrially attractive. In addition, the time to reach the peak hardness of the Mg-Sn based alloy is too long for practical applications (more than 240 h at 200°C). Recently, we have optimized the composition of Mg-Sn-Al-Zn alloys for attaining the highest age hardening response; *i.e.*, HV~ 81 after aging an Mg-9.8Sn-3.0Al-0.5Zn (wt.%) alloy for 360 h at 200° C [5]. Thus, in this work, we employed the microalloying of Na to examine the cumulative effects of microalloying Mg-Sn with Al, Zn, and Na in an attempt to explore possible synergistic effect of enhancing both precipitation hardening and kinetics of the Mg-9.8Sn-3.0Al-0.5Zn (wt.%) alloy further

3.2 Experimental

Experimental alloy ingots with nominal composition of Mg–9.8Sn-3Al-1.2Zn (wt.%) (TAZ1031) and Mg–9.8Sn-3Al-1.23Zn-0.1Na (wt%) (TAZ1031-0.1Na) were prepared by induction melting using steel crucibles under an Ar atmosphere and were cast into steel molds. Chemical analysis of cast billets was performed using ICP-OS including Fe

trace analysis to ensure sound chemical composition. Na additions were produced in the form of Sn-Na master alloy induction melted inside inert Quartz tubes also under Ar atmosphere, and later added in master alloy form. The nomenclatures of the alloys and their compositions in both at.% and wt.% are shown in Table 1. Hereafter, all alloy compositions are described in wt.%. The ingots were homogenized at 500^{o}C for 48 h in a He-filled Pyrex tube. Small section-samples were cut out from the ingots, and were solution treated at 525^{o}C for 1 h, and water quenched. Artificial aging was performed at 200^{o}C and 160^{o}C in a silicone oil bath for various aging times immediately after solution treatment. The age hardening response was measured by a Vickers hardness tester under a 500g load, and a minimum of 8 indentations where measured to obtain the aging curves. Transmission electron microscope (TEM) specimens were prepared by punching 3 mm discs, mechanical polishing, and ion-milling using the Precision Ion Polishing System (GATAN691). TEM observation was carried out using FEI Tecnai 20 TEM operating at 200 kV. Three dimensional atom probe (3DAP) analysis was carried out with a locally built laser assisted wide angle atom probe using a femtosecond laser pulse at a wavelength of 343 nm. Square bars with dimensions of ~0.5 × 0.5 × 15 mm^3 were cut from the bulk samples and electro polished to prepare sharp needle-like specimens for atom probe analyses. The 3DAP analyses were performed in an ultrahigh-vacuum condition (<1×10^8 Pa) at a temperature of 25 K.

3.3 Results

3.3.1 Age hardening response

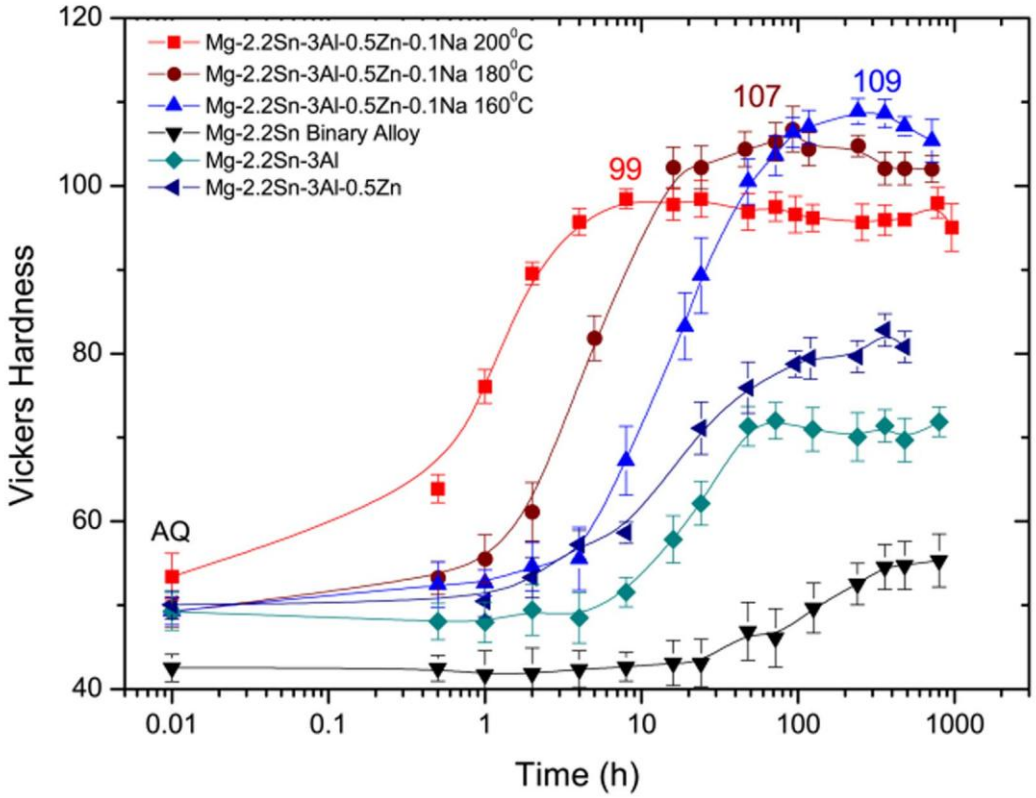

Fig.1: Age hardening behavior of studied Mg-9.9Sn, Mg-9.9Sn-3.1Al, Mg–9.8Sn-3Al-1.2Zn at200^{o}C, and Mg–9.8Sn-3Al-1.23Zn-0.1Na alloys at various temperatures

Fig. 1 shows the age hardening behavior of the binary Mg-10Sn (T10), quaternary Mg-10Sn-3Al-1Zn (TAZ1031) and Mg-10Sn-3Al-1Zn-0.1Na (TAZ1031-0.1Na) alloys as a function of aging time at various temperatures. The hardness values of the as solution treated samples ranges from 50 to 53 ±2 HV. The peak hardness of the quaternary Mg-10n-3Al-1Zn alloy aged at 200°C is around 81 ±2 HV, but it takes as long as 120 h to reach the peak hardness. Surprisingly, the addition of 0.1Na to the Mg-10Sn-3Al-1Zn alloy increased the peak hardness up to 99±1.2 HV within 8 h at 200 °C. Lower temperature aging at 160^{o}C and 180^{o}C enhanced the peak hardness further to 107 ±2.7HV, and 109±1.55 HV while

shifting the peak age time to 100 h and 120 h respectively. The increment of the peak hardness in the Mg-10Sn-3Al-1Zn-0.1Na alloy is ~46 HV, compared to about 26 HV for the Mg-10Sn-3Al-1Zn-0.1Na alloy. A rapid increase in hardness was observed after 30 min aging at 200^{o}C, and an incubation time of ~1 h before the start of hardening was also observed at lower aging temperatures of 160 and 180^{o}C. It was found that both the kinetics and the hardening increment are significantly enhanced by the trace addition of Na, leading to the unprecedented hardness to rare earth free Mg-based alloys.

3.3.2 Precipitate characterization

Figure 2 shows the microstructures of the peak aged Mg-10Sn-3Al-1Zn and Mg-10Sn-3Al-1Zn-0.1Na alloys at 200°C. Figure 2 (a) and (b) show the bright field TEM images of the Mg–10Sn-3Al-1Zn alloy taken along the $[0001]$ and $<11\bar{2}0>$ zone axes. The microstructure consists mainly of lath/rod like precipitates. Most of the precipitates lie on the (0001) basal plane with the growth direction of $<11\bar{2}0>$. In the Mg-10Sn-3Al-1Zn-0.1Na alloy, the precipitate length is about 380 ±174 nm. Figure 2 (c) and (d) show the bright field TEM images of the Mg-10Sn-3Al-1Zn-0.1Na alloy along the $[0001]$ and $<11\bar{2}0>$ zone axes with similar precipitate morphology lying on the (0001) plane. The precipitates in the Na containing alloy were significantly refined to ~70 ± 4 nm in length, 25 ±9 nm in width, and 16 ±9 nm in thickness. The refined size of the precipitates can explain the increase of about ~20 HV in the peak hardness of the Na containing alloy as compared to the quaternary Mg-10Sn-3Al-1Zn alloy. Figure 2 (e) and (f) show higher magnification bright field TEM images

of the same peak aged condition along the [0001] and <11$\bar{2}$0 > zone axes, where the refined nanometer scale Mg_2Sn laths are clearly dispersed uniformly on the basal plane.

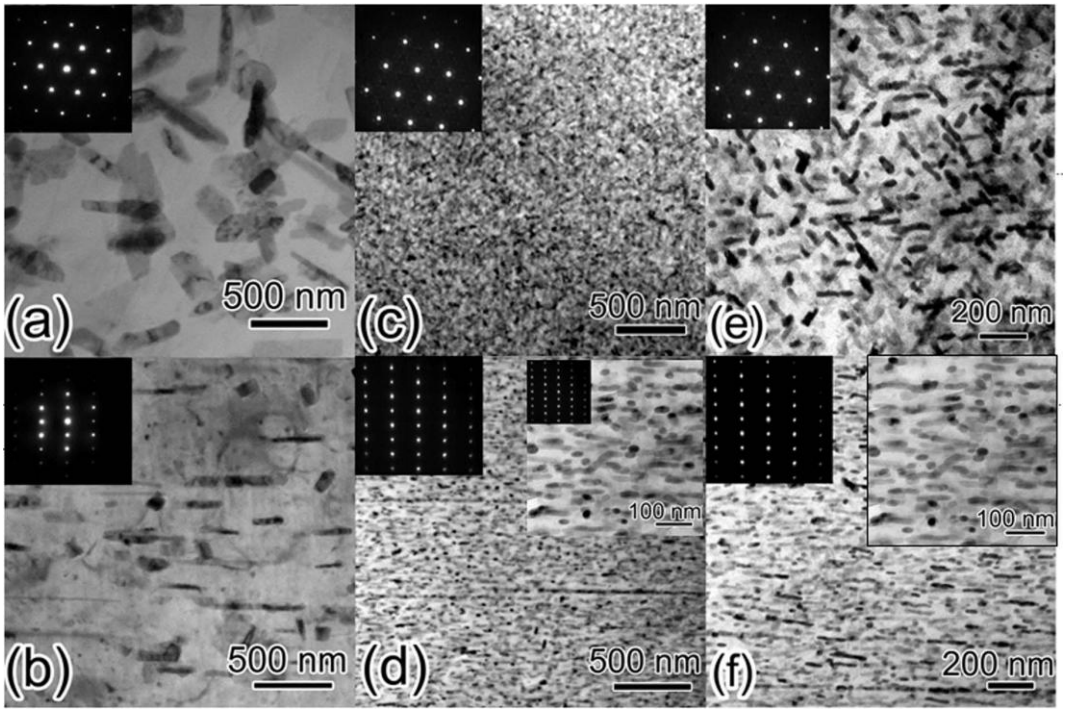

Fig.2: TEM bright field images of (a)-(b) Mg–10Sn-3Al-1Zn alloy peak aged at 200^{o}C, (c)-(d) Mg–10Sn-3Al-1Zn-0.1Na alloy peak aged at 200^{o}C along the [0001], [11$\bar{2}$0],]zone axis, (e)-(f) Higher magnification bright field images of Mg–10Sn-3Al-1Zn-0.1Na alloy peak aged at 200^{o}C along the [0001], [11$\bar{2}$0],]zone axis respectively.

Fig.3 (a) shows a high angle dark field scanning transmission electron microscopy (HAADF-STEM) image of the Mg-10Sn-3Al-1Zn-0.1Na alloy peak aged at 160^{o}C, showing a uniform distribution of fine lath like Mg_2Sn precipitates along the <11$\bar{2}$0 > zone axes. In addition to the lath like precipitates, fine spherical particles are observed with a brighter contrast, suggesting higher concentration of Sn in these particles compared to the lath like precipitates. EDX maps from the same area in Fig. 3 (b) and (c) present the distributions of Sn and Na. Fig3.(d) shows a superimposed (Sn, Na) EDX map at a higher magnification of the outlined area in the HAADF-STEM image in Fig.3 (a) where the Na atoms co-cluster in

the vicinity of the basal Mg_2Sn lath precipitate. Fig.3 (e) show HAADF-STEM image of a Sn cluster that is ~4 nm in diameter and fully coherent with the Mg matrix.

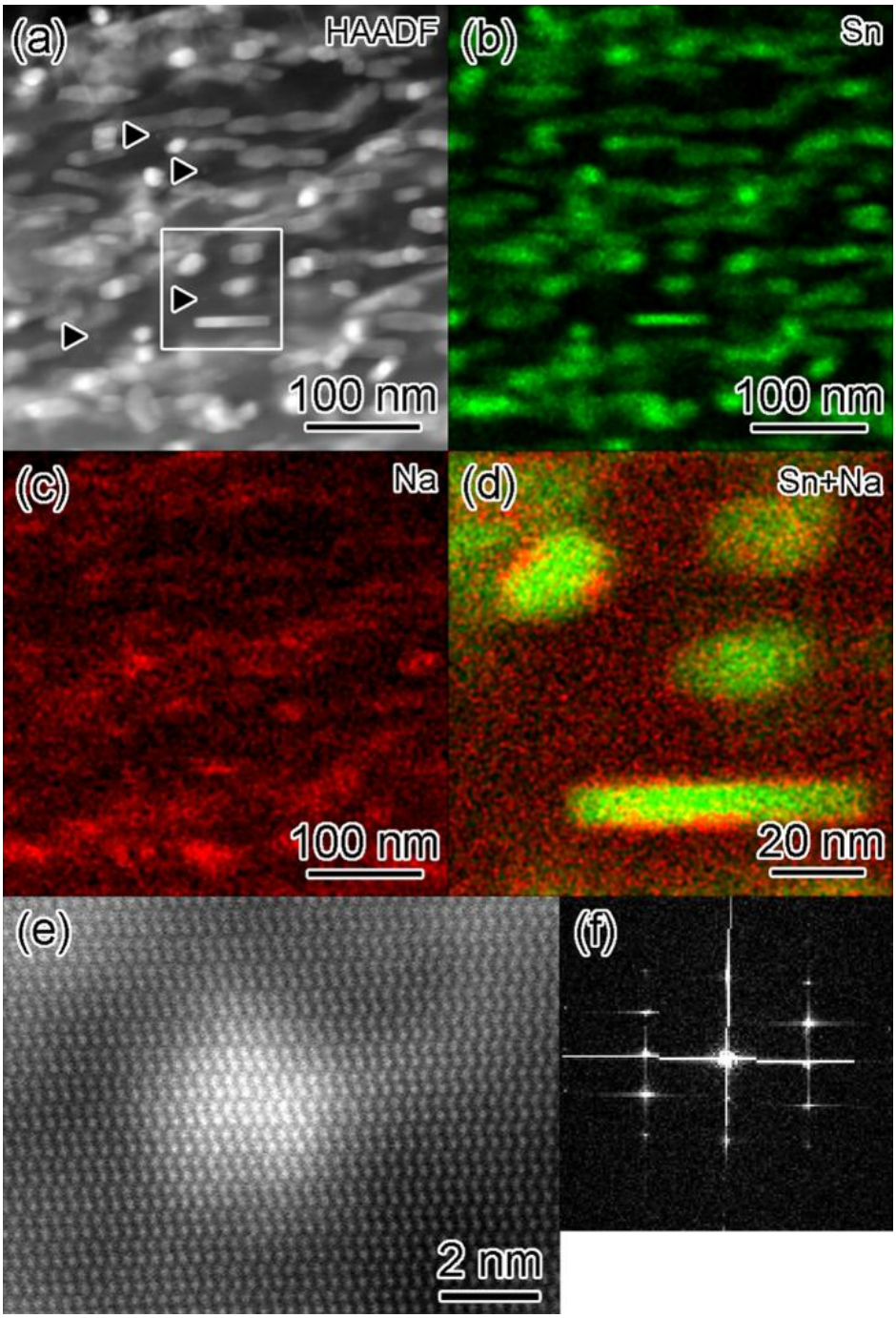

Fig.3-(a) HAADF-STEM images of Mg–10Sn-3Al-1Zn-0.1Na alloy peak aged at 160^{o}C taken along <11$\bar{2}$0 > zone axes, and EDX mapping of (b)Sn distribution,(c)Na distribution, (d) higher magnification Sn-Na superimposed map, (e) -HAADF-STEM image of Sn nano cluster as indicated by arrows positions in Fig.3(a), (f) Fourier transform image of Fig.3(e)

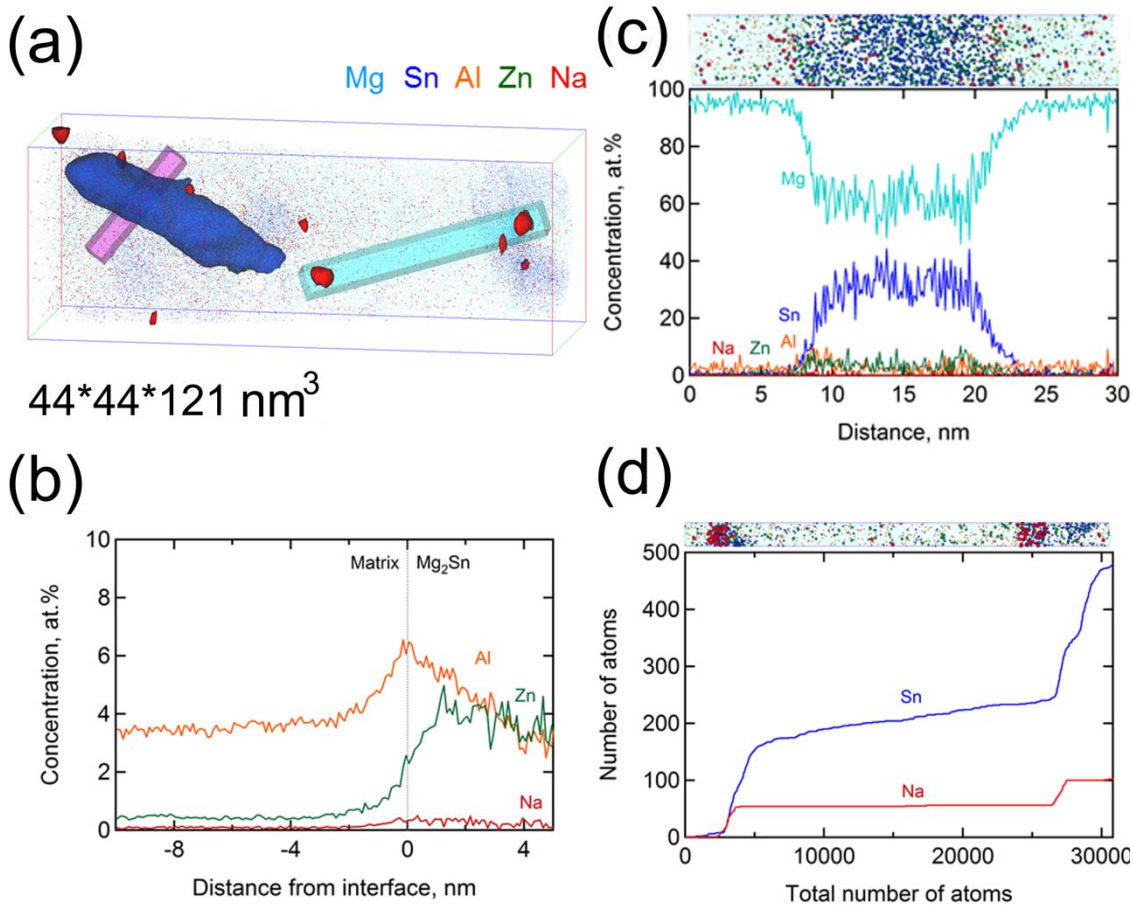

Fig.4: Three dimensional atom probe mapping of peak aged Mg-10Sn-3Al-1Zn-0.1Na at 160^{o}C (a) Sn-rich Mg_2Sn zones, with different alloying elements distribution, (b) magnified map showing the composition of a Sn rich region, (c) compositional profile of main alloying elements at the matrix/precipitate interface, (d) corresponding ladder diagram for Na and Sn atoms across selected volume.

The 3DAP analysis result of the Mg-10Sn-3Al-1Zn-0.1Na alloy peak aged at 160^{o}C is shown in Fig. 4. Two Sn enriched regions are recognized from the density of Sn atoms in Fig. 4(a). To visualize the lath-like shape of the Sn-enriched phase, iso-concentration surface of 9.at,%Sn was created for one of the Sn-enriched phases (represented by the blue region).

Figure 4 (b) is a magnified 3DAP map obtained from the selected volume displayed in purple. The composition of the Sn rich region of ~33% is consistent with that of Mg_2Sn phase. The proximity diagram across the matrix/Mg_2Sn interface is shown in Fig. 4(c) where a strong enrichment of Al atoms at the Mg/Mg_2Sn interface is evident while Zn and Na atoms are enriched in the precipitates. In addition, Na-enriched particle are also observed as shown by the red iso-concentration surface. They are in the proximity of the Mg_2Sn lath like precipitate as shown in Fig. 4 (a). A selected volume (shown in light blue) in Fig. 4 (a) includes two Na-enriched particles, confirming the clustering tendency. Fig. 4 (d) shows the corresponding ladder diagram for Na and Sn which clearly demonstrates the co-clustering feature of Sn and Na atoms. The analysis of the ladder diagram shows that the composition of the cluster is Mg-12.8Sn-5.1Na-1.3Zn-3.6Al. These Sn-Na clusters shown in the AP data are in consistent with the cluster like feature observed by HAADF-STEM in Fig.3(e)

3.4 Discussions

Previous investigations have shown that Al and Zn are moderate precipitate refiner for the Mg-Sn system, and the composition for the highest precipitation hardening has been optimized to Mg-10Sn-3Al-1Zn **[5]**. Mendis *et al*. have reported that Na addition substantially enhance the peak age hardness as well as the precipitation kinetic of Mg-Sn and Mg-Sn-Zn alloys without clarifying the underlying mechanism **[2,6]**. Based on these investigations, we have added Na to the optimized Mg-10Sn-3Al-1Zn to find the unprecedentedly high peak hardness for the magnesium alloy without rare earth element additions. Noteworthy observation is that not only the peak hardness but also the kinetics for the precipitation is substantially accelerated. One of the drawback for the application of Mg-Sn based alloys as heat-treatable wrought alloy was its slow kinetics to reach the peak

hardness. However, the newly developed Mg-10Sn-3Al-1Zn-0.1Na alloy reaches the peak hardness only after 8 and 90 hs at 200 and 180°C.

The presence of Na clusters as well as the segregation of Al atoms at the precipitate/matrix interface explain the mechanism of refining the Mg_2Sn precipitates to the 70 nm size range, which is a scale not attained previously in the Mg-Sn system. Mg and Na have a very large positive enthalpy of mixing (ΔH=+10 kJ/mol)**[7]**, virtually immiscible each other. So there is a very strong driving force for Na to precipitate out from the supersaturated solid solution with Mg even in a very small amount of addition. On the other hand, Na has a negative enthalpy of mixing with Sn (ΔH=–8 kJ/mol) **[7]**. Hence, on phase separating from Mg, Na will co-segregate with Sn atoms, which could act as heterogeneous nucleation sites for precipitation as seen in Fig. 3 and 4. From Fig. 4 (c), we can see Al atoms tend to be rejected from the Mg_2Sn phase, which cause the segregation of Al at the Mg/Mg_2Sn interface. This would control the growth of the precipitate due to the solute-drag like effect, and this would be another reason why substantially fine precipitates are observed in the Mg-10Sn-3Al-1Zn-0.1Na alloy.

Since significant strengthening has not been expected upon T6 treatment (solution heat treatment and artificial aging) in the extruded Mg-Sn alloys **[8,9]**, the Mg-Sn system has not been recognized as suitable heat treatable alloy for high strength application up to now. However, the significantly high age hardening response achieved in the Mg-10Sn-3Al-1Zn-0.1Na alloy can open up a possibility of the development of heat treatable alloy with relatively cheap alloying elements. In addition, the Mg-Sn system is extrudable at a lower temperature compared to other Mg alloys such as Mg-Zn based alloys **[10,11-14]**. Further investigations may lead to the development of the heat treatable Mg-Sn based wrought alloys, which can substantially increase the strength upon T6 or T5 aging treatment.

.3.5 Summary and Conclusions

In summary, the Na micro-alloyed Mg-9.8Sn-3.0Al-0.5Zn-0.1Na alloy (TAZ1031-0.1Na) showed the highest age hardening response with the fastest kinetics among the Mg-Sn based alloys reported so far. The peak hardness exceeding 100 HV that is usually unachievable in magnesium alloys without rare earth elements, has been confirmed in the alloy after aging for 10 h at 180°C. The successful improvement in the aging response was made possible by introducing Na clusters as heterogeneous nucleation sites for the Mg_2Sn precipitates, which substantially refine the aged microstructure.

References

[1] T.T. Sasaki, K. Oh-ishi, T. Ohkubo, K. Hono, Scr. Mater. 55 (2006) 251–254.

[2] C.L. Mendis, C.J. Bettles, M.A. Gibson, C.R. Hutchinson, Mater. Sci. Eng. A 435(2006) 163–171.

[3] C.L. Mendis, K. Oh-ishi, K. Hono, Scr. Mater. 57 (2007) 485–488

[4] S. Celotto, Acta Mater. 48 (2000) 1775–1787.

[5] F. R. Elsayed, T.T. Sasaki, C.L.Mendis, T. Ohkubo, and K. Hono, Mater. Sci. Eng. A, 566 (2013) , pp. 22-29.

[6] C. L. Mendis, C.J. Bettles, M.A. Gibson, S. Gorsse, C.R. Hutchinson, Philos. Mag.Lett. 86 (2006) 443–456

[7] F.R. de Boer , R. Boom , W.C.M. Mattens , A.R. Miedema , A.K. Niessen,, Cohesion in Metals- Transition Metal Alloys (Cohesion and Structure), , North Holland Publications, 1989, I S B N : 0444870989

[8] T.T. Sasaki, J.D. Ju, K. Hono, and K.S. Shin, Scr. Mater. 61 (2009) 80–83

[9] J.R. TerBush, M. Setty, N. Stanford, M.R. Barnett, A.J. Morton, and J.F. Nie, proceedings of 9th International Conference on Magnesium Alloys and their Applications (eds W.J. Poole and K.U. Kainer) p 579

[10] T. Sasaki, K. Yamamoto, T. Honma, S. Kamado and K. Hono, Scr. Mater. 59 (2008) 1111–1114

[11] S.S. Park, and B.S. You, Scr. Mater. 65 (2011) 202–205

[12] S.S. Park, W.N. Tang, B.S. You, Mater. Lett. 64 (2010) 31–34

[13] W.L. Cheng , H.S. Kim , B.S. You , B.H. Koo , S.S. Park, Mater. Lett. 65 (2011) 1525–1527

[14] C.L. Mendis, K. Oh-ishi, Y. Kawamura, T. Honma, S. Kamado, K. Hono, Acta Mater. 57 (2009), 749-760

Chapter 4 - Extruded TAZ alloys processing-property relationship

4.1-Introduction

Mg-Sn alloys are known to be extrudable at a wide range of extrusion temperatures and speeds as high melting temperature (~780°C) of the Mg_2Sn intermetallic phase prevent the occurrence of hot shortness as compared to Mg-Zn and Mg-Al based alloys **[1]**. Sasaki et al. **[2]** demonstrated high strength in Mg-9.8Sn-1.2Zn-1.0Al wt% alloy at lower extrusion temperature of 250°C and ram speed of 0.1mm/s. Cheng et al. **[1]** also showed a relatively high extrusion ram speed window of 1.3 - 6.7 mm/s using a similar Mg-8Sn-1Al-1Zn wt% alloy (TAZ811). The strength-ductility combinations of these alloys are strongly dependent on extrusion conditions **[1,3-4]**.

Based on our optimized alloy design work to produce the composition of Mg–Sn–Al–Zn alloys with high age-hardening response, i.e. HV ≈ 81 after aging for 360 h at 200 °C for the Mg–9.8Sn–3.0Al–0.5Zn (wt.%) (TAZ1031) alloy **[5]**.and the Na microalloyed TAZ10310.1Na alloy with enhanced precipitation kinetics and peak hardness **[6]**; we have extended the study to thermo-mechanically processed form by extruding the TAZ1031 and TAZ1031-0.1Na alloys at different temperatures and extrusion speeds, and the resulting microstructure, texture, and mechanical properties were investigated by comparing with those of AZ31 commercial Mg alloy as benchmark.

4.2-Experimental

Alloy ingots were prepared by induction melting high purity magnesium, tin, aluminum and other alloying elements using steel crucibles under an argon atmosphere and by casting into steel molds. In this study Mg-9.8Sn-3.0Al-1.23Zn wt% (TAZ1031), Mg–9.8Sn-3Al-1.23Zn-0.09Na (TAZ1031-0.1Na), and Mg-3Al-1Zn (AZ31) alloys were prepared. The alloy nomenclatures and their chemical compositions in both wt.% and at.% are summarized in **Table 1**. The cast TAZ1031 and TAZ1031-0.1Na billets were homogenized using a vacuum box furnace under argon gas flow at 350°C for 24 h, ramped at a heating rate of 5Kh^{-1} to 525°C, then water quenched. AZ31 billets were homogenized at 400°C for 3 h, followed by water quenching.

Solution treated billets were machined into ϕ42.8 mm extrusion billets. The billets were soaked at respective extrusion temperatures for 10 min along with the die assembly prior to extrusion. Indirect extrusion experiments were performed on a 100 t vertical hydraulic press with an extrusion ratio of 20 to produce ϕ9.6 mm extruded bars. The extrusion conditions employed in this study as well as the mechanical properties are summarized in **Table 2**. Tensile and compressive samples were machined along extrusion direction, and the mechanical properties of the extruded bars were evaluated by tensile and compression tests performed at an initial strain rate of 1×10^{-3}.

Optical microscopy was performed on polished samples etched with acetic picral solution to reveal grain structure. EBSD analysis was carried out using HKL EBSD detector and HKL Channel 5 acquisition software on a field-emission scanning electron microscope (Carl Zeiss CrossBeam 1540EsB). Thin foil specimens for TEM observations were prepared by punching 3 mm diameter discs, mechanical polishing, dimple grinding, as well as ion milling using Gatan PIPS Precision Ion Polishing System Model 691 at room temperature.

The microstructure characterization was carried out by transmission electron microscopy (TEM) using a FEI Tecnai 20 TEM operating at 200 kV, and the EDX measurements were performed using an EDAX detector on FEI Tecnai 20 TEM .

Table 1: Nomenclature and Chemical composition of alloys in this study

Alloy Designation	**Atomic%**				**Weight%**			
	Sn	**Al**	**Zn**	**Na**	**Sn**	**Al**	**Zn**	**Na**
AZ31	-	2.73	0.38	-	-	3	1	-
TAZ1031	2.2	3.0	0.5	-	9.8	3.0	1.23	-
TAZ1031-0.1Na	2.2	3.0	0.5	0.1	9.8	3.0	1.23	0.09

Table 2- Experimental matrix of extrusion conditions employed in this study

Alloy	**T_{ext} ^{o}C**	**Ram speed mm/s**
AZ31	250	0.1
AZ31	300	0.1
AZ31	300	1
AZ31	300	2
AZ31	400	2
TAZ1031	250	0.1
TAZ1031	300	0.1
TAZ1031	300	1
TAZ1031	300	2
TAZ1031	400	2
TAZ1031-0.1Na	300	0.1
TAZ1031-0.1Na	300	2
TAZ1031-0.1Na	400	2

4.3- Results

4.3.1 Results AZ31 extruded alloys as benchmark Mg wrought alloys

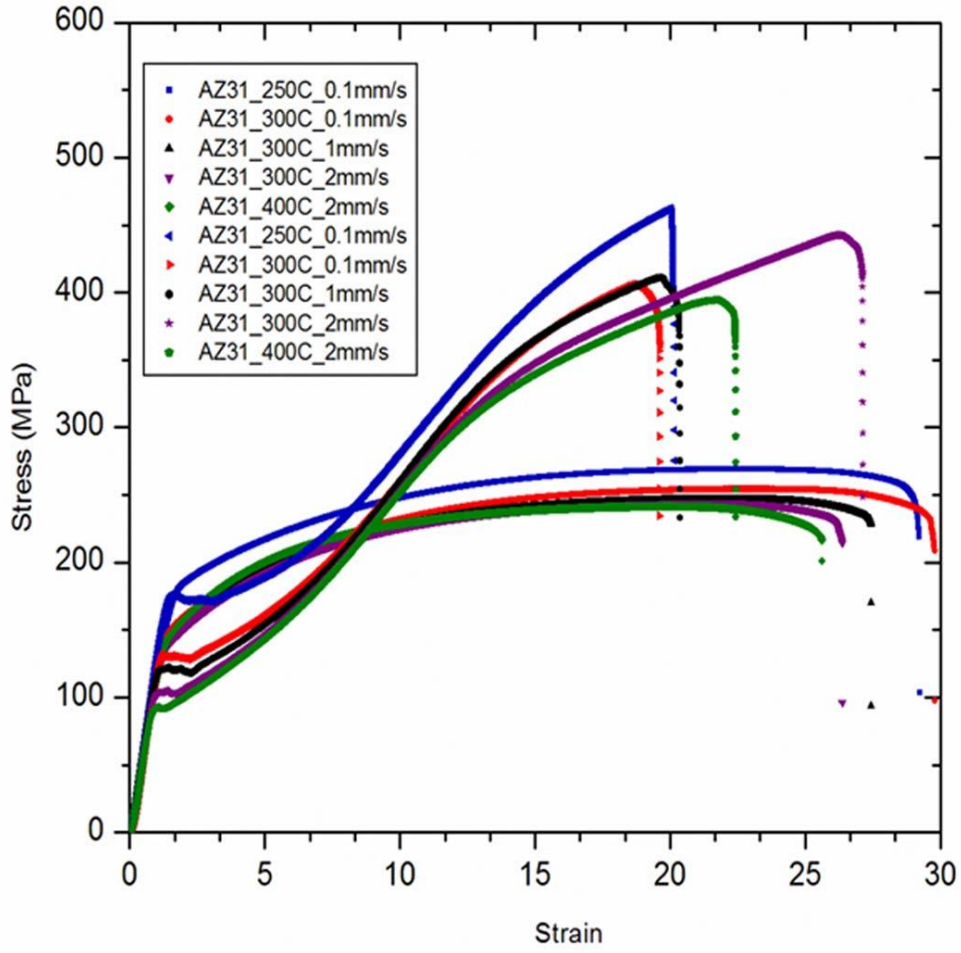

Fig. 4.1 shows Tensile and compression stress-strain curves of AZ31 alloys extruded with different conditions.

Figure 4.1 shows tensile and compressive stress-strain curves of as extruded AZ31, alloys. The AZ31 alloy shows the highest tensile yield strength σ_{ty} with the extrusion temperature at T=250°C and ram speed= 0.1mm/s. σ_{ty} decreases as temperature and ram speed increases except when extrusion temp is increased to 400°C and ram speed to 2mm/s.

Compressive yield strength, σ_{cy} follows the same trend as σ_{ty}, while tensile elongations, ε_t, values are lower at slower extrusion speed and temperature

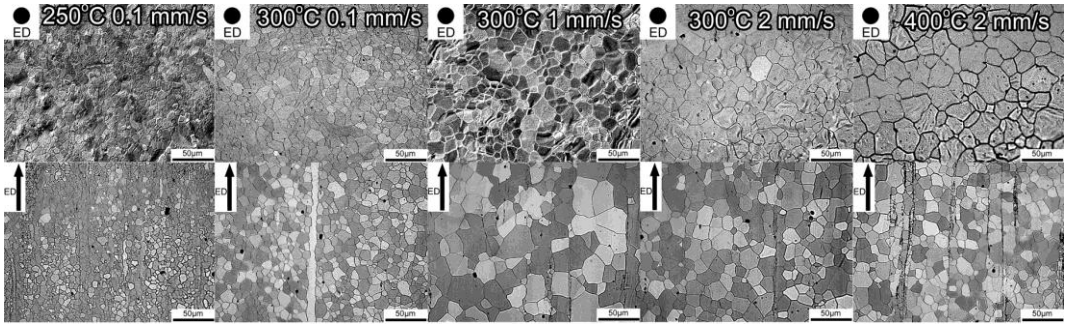

Fig. 4.2 shows optical micrographs of AZ31 alloy extruded in the range of conditions in Table 2

Figure 4.2 shows the microstructure of the AZ31 alloys extruded at 300°C at different ram speeds ranging from 0.1 to 2 mm/s. The grain size increases as the ram speed is increased from 0.1 to 1 mm/s suggesting that frictional heat rise is sufficient to cause grain growth on increasing extrusion speed; however, there is no significant change on further increasing the ram speed to 2 mm/s. The extruded microstructure appears to be mostly recrystallized due to dynamic recrystallization (DRX) during extrusion; nevertheless a tiny fraction of un-recrystallized grains elongated along ED are seen in the samples extruded at 0.1 mm/s with a much lower occurrence and the formation of deformation twins were not seen at the extrusion conditions at 300°C in the overall microstructure of AZ31 extruded samples. These findings related to suppressed twinning are in line with previous study on indirectly extruded AZ31 alloy at lower ram speeds ranging between 1.3-6.7 mm/s and temperatures between 250°C to 300°C **[7].**

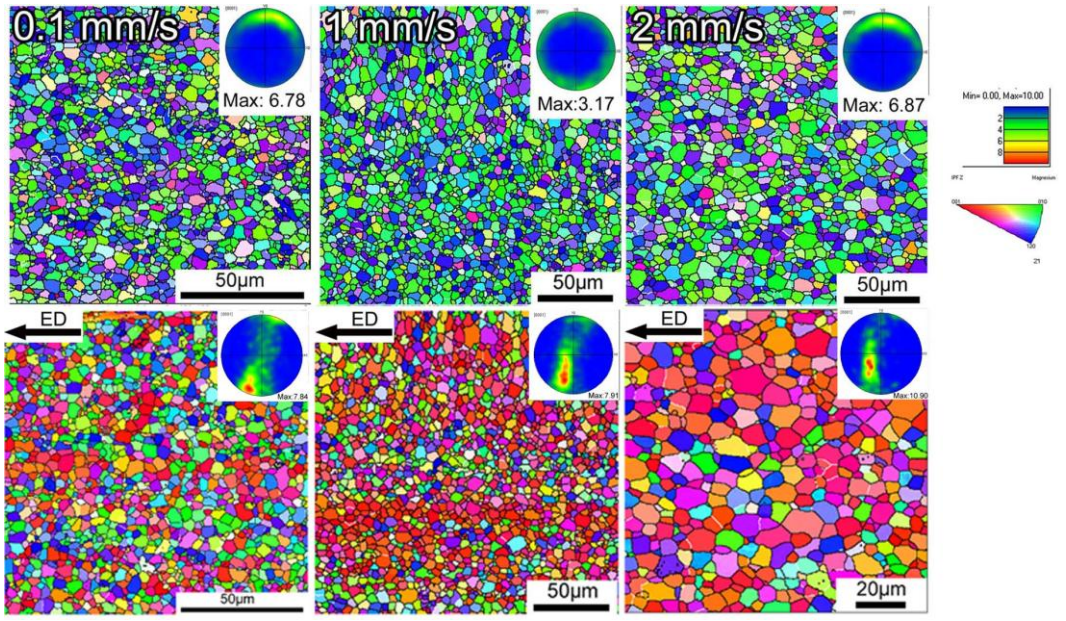

Fig. 4.3 shows EBSD IPF-Z orientation maps of AZ31 alloy extruded at different ram speeds at 300°C

Figure 4.3 shows EBSD inverse pole figure orientation maps (IPF-Z) of AZ31 alloys extruded at 300°C at different ram speeds. The grain size dependence is clearly visible from the orientation maps with grain growth with the ram speed. The average grain sizes were 2.3, 4.3, 5.3 μm for the ram speeds of 0.1, 1, and 2 mm/s, respectively. The maps show typical extrusion fiber texture in all conditions in which basal planes are preferentially oriented parallel to the extrusion direction as highlighted in the corresponding inset (0001) pole figures. Based on the peak intensity values of the pole figures, the texture does not seem to vary significantly depending on the ram speed within the range of 0.1 - 2 mm/s; however, a slight increase in maximum intensity was observed as ram speed increased. The texture-dependence on ram speed at 300°C does not seem strong within the relatively lower speed range of 0.1-2 mm/s employed

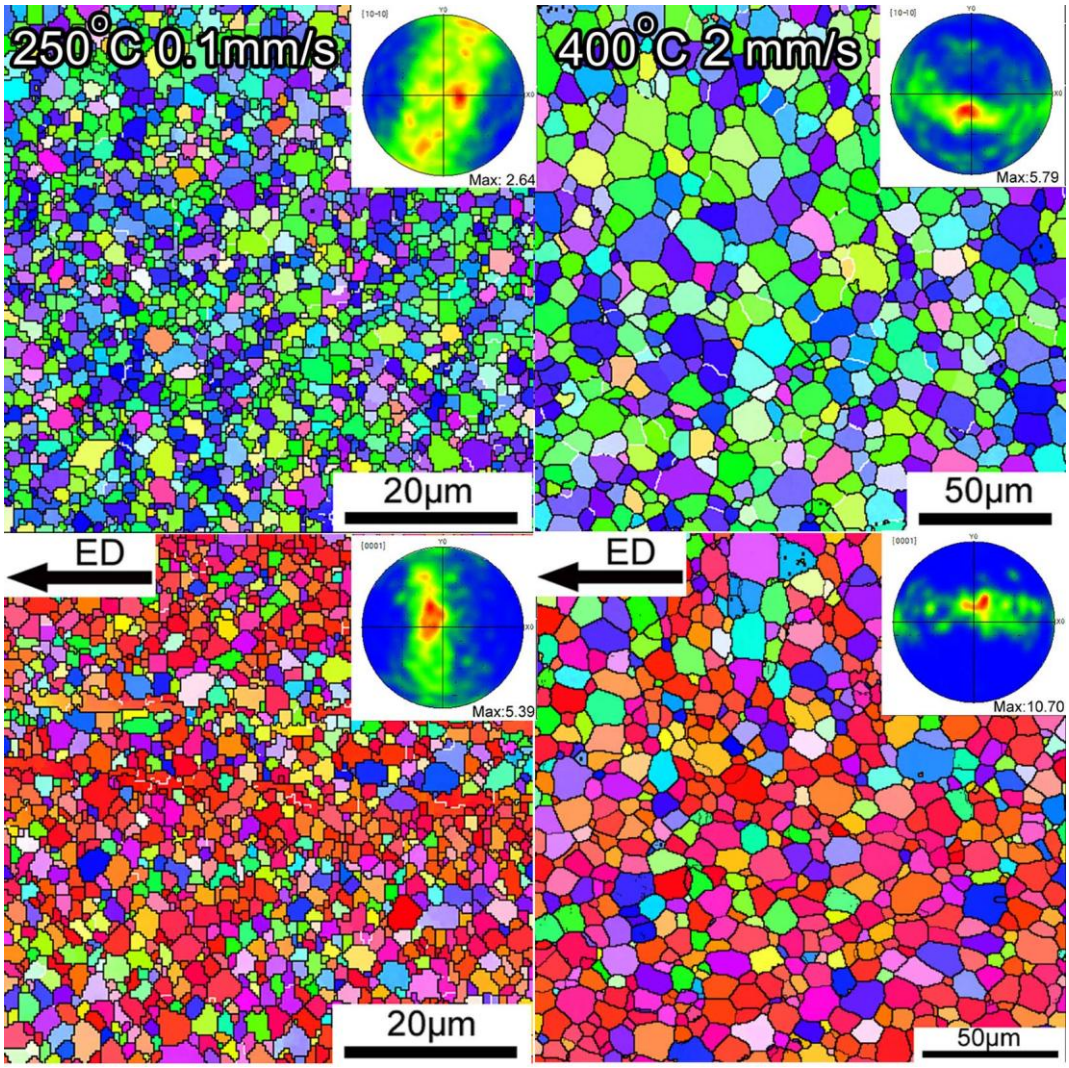

Fig. 4.4 shows EBSD IPF-Z orientation maps of AZ31 alloy extruded at 250°C and 400°C with inset pole figures showing maximum texture intensities.

Figure 4.4 shows EBSD inverse pole figure orientation maps (IPF-Z) of AZ31 alloys extruded at lower temperature 250°C, ram speed of 0.1 mm/s and at 400°C, ram speed of 2 mm/s. A significant grain growth is apparent from the maps upon increasing temperature to 400°C. The maps show typical extrusion fiber texture in both conditions in which basal planes are preferentially oriented parallel to the extrusion direction as highlighted in the

corresponding inset (1010), and (0001) pole figures. Based on the peak intensity values of the pole figures, the texture is strengthened at the higher extrusion temperature.

4.3.2 Results TAZ1031 extruded alloys

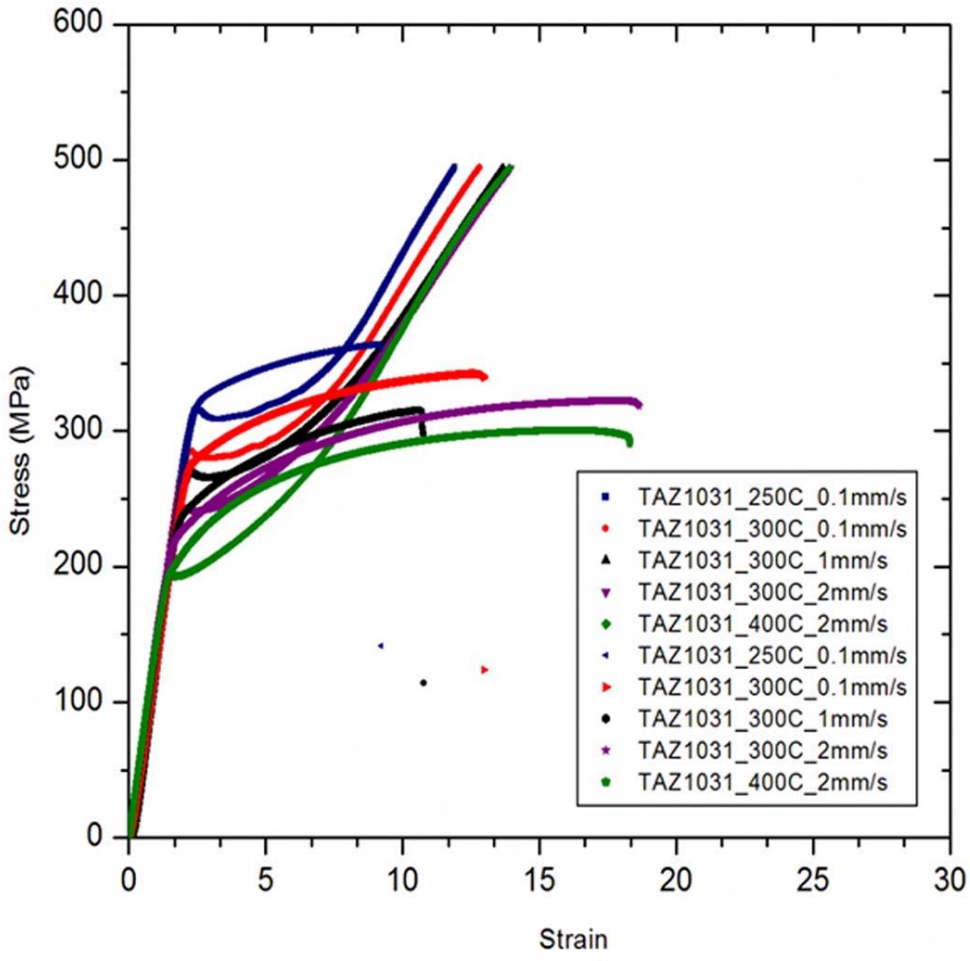

Fig. 4.5 shows Tensile and compression stress-strain curves of TAZ1031 alloys extruded with different conditions.

Figure 4.5 shows stress-strain curves for both tension and compression of TAZ1031 extruded alloys. The TAZ1031 alloys show much higher strength compared to AZ31 with reduced ductility. σ_{ty} is reaches the highest value of 320 MPa for the extrusion conditions at T=250°C and ram speed= 0.1mm/s with ε_t=6.1% and σ_{ty} decreases to 214 MPa as the extrusion temperature is increased to 400°C and ram speed =2 mm/s with improved ε_t=11%.

Compressive yield strength, σ_{cy}, follow the same trend as σ_{ty} decreasing from 318 MPa at low extrusion temperature of 250°C and ram speed of 0.1mm/s to 206MPa at the extrusion temperature of 400°C and ram speed= 2 mm/s. The highest ε_t was 14.5% for T=300°C and ram speed= 2 mm/s.

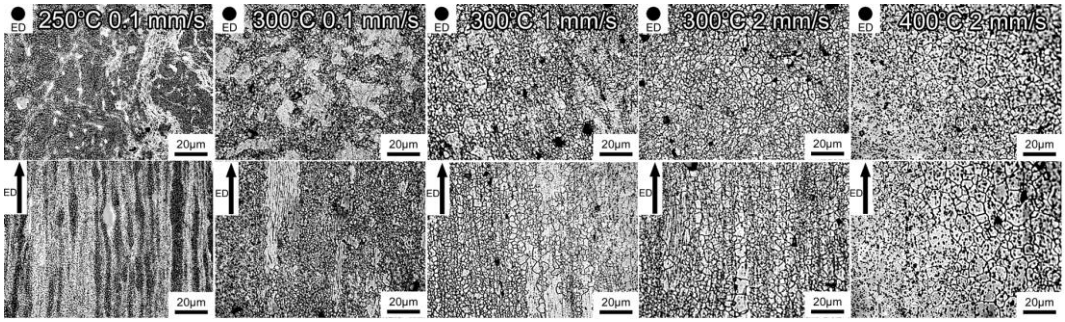

Fig. 4.6 shows optical micrographs of TAZ1031 alloy extruded in the range of conditions in Table 2

Figure 4.6 shows optical micrographs of the TAZ1031 alloys extruded at 300°C at different ram speeds ranging from 0.1 to 2 mm/s. In contrast to the extruded AZ31 alloys, microstructure is composed of both coarse un-recrystallized grains and dynamically recrystallized (DRX) grains. The fraction of un-recrystallized grains is higher at lower ram speed of 0.1mm/s and is reduced as extrusion ram speed is increased. For T=300°C and ram speed= 0.1 mm/s, a larger volume fraction of un-recrystallized grains is observed, and the microstructure becomes fully recrystallized as the ram speed is increased to 2 mm/s. The TAZ1031 alloys exhibit significantly finer grain size than those of AZ31, and the grain size grows with increasing the extrusion temperature but its ram speed dependence is much smaller compared to that of AZ31 alloy.

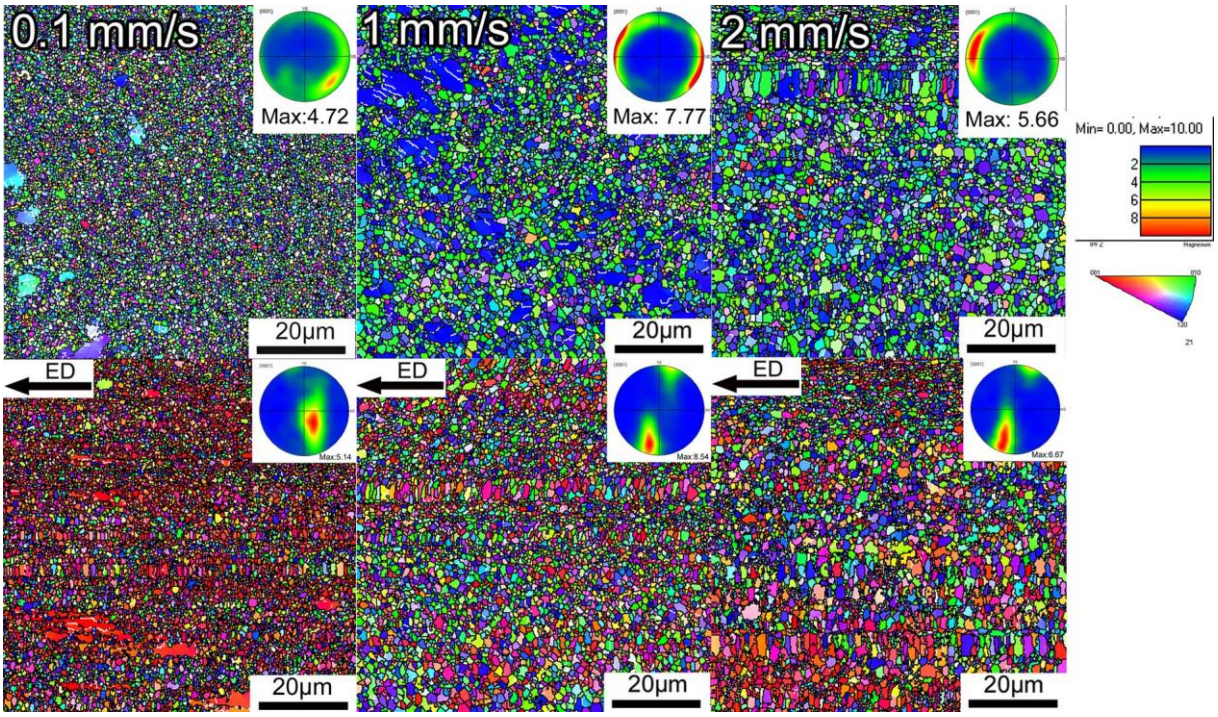

Fig. 4.7 shows EBSD IPF-Z orientation maps of TAZ1031 alloy extruded at different ram speeds at 300°C.

Figure 6 shows EBSD IPF-Z orientation maps of TAZ1031 alloy extruded at 300°C at different ram speeds. The maps were again taken from the cross section perpendicular to the extrusion direction. The orientation maps reveal average grain sizes of 0.7,1.0,1.0 μ m for the ram speeds of 0.1, 1, 2 mm/s, respectively showing grain size dependence on ram speed is weaker than that observed in the AZ31 alloy. At 0.1 mm/s and 1mm/s, fine (DRX) dynamically recrystallized grains as well as un-recrystallized coarser regions can be seen, while at 2mm/s the microstructure is mostly recrystallized. At ram speed of 1 mm/s a larger volume fraction of un-recrystallized grains and a stronger overall intensity of the fiber texture is observed. The general trend is weakening texture as extrusion ram speed is increased and the microstructure becomes more fully recrystallized.

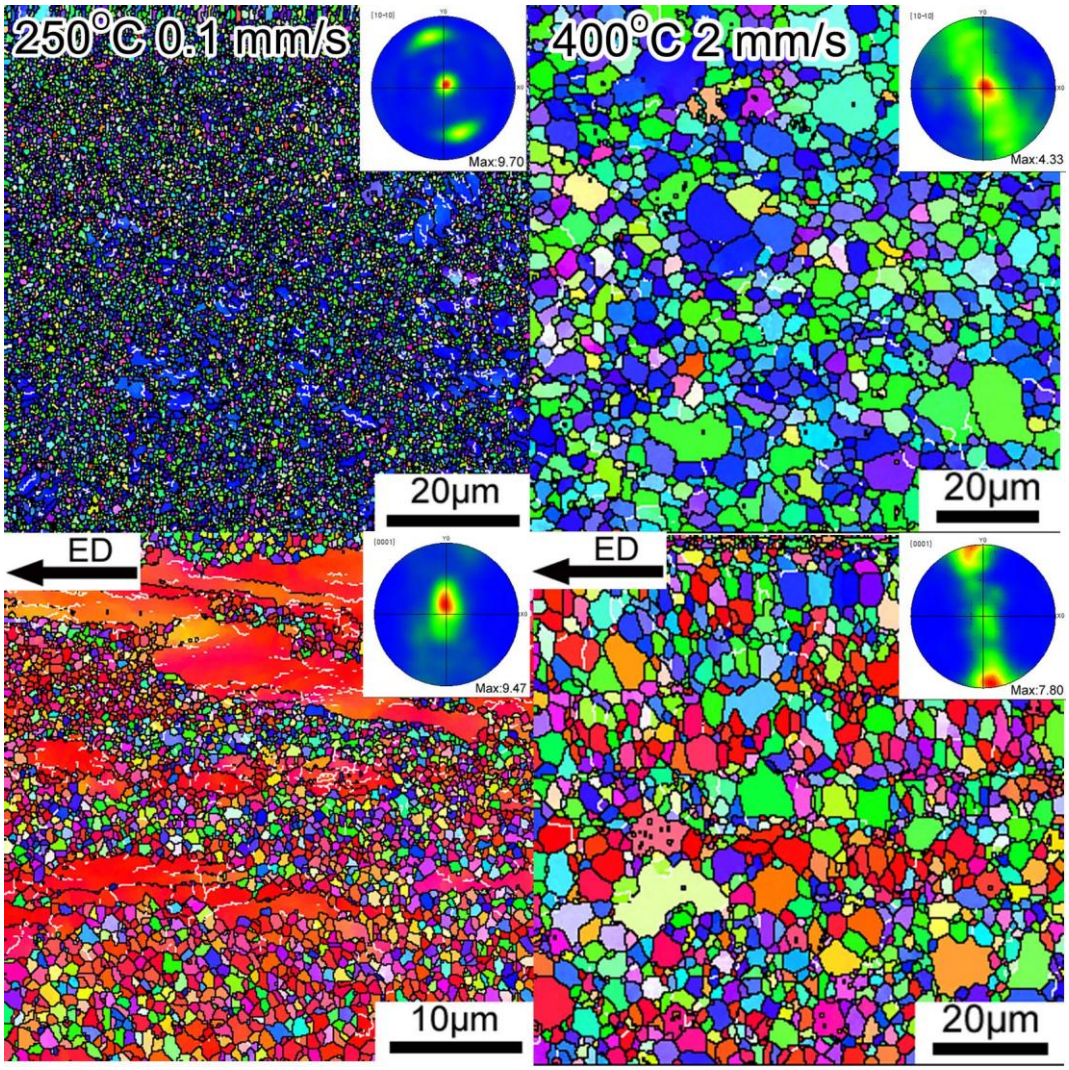

Fig. 4.8 shows EBSD IPF-Z orientation maps of TAZ1031 alloy extruded at 250°C and 400°C with inset pole figures showing maximum texture intensities.

Figure 4.8 shows EBSD inverse pole figure orientation maps (IPF-Z) of TAZ31031 alloys extruded at lower temperature 250°C, ram speed of 0.1 mm/s and at 400°C, ram speed of 2 mm/s. The microstructure and grain size difference is clearly visible from the orientation maps. Microstructure is bimodal with coarser un-recrystallized grains and refined DRX dynamically recrystallized grains at the lower extrusion temperature, while it's fully recrystallized at 400°C. The maps show typical extrusion fiber texture in both conditions in which basal planes are preferentially oriented parallel to the extrusion direction as

highlighted in the corresponding inset (1010), and (0001) pole figures. A strong grain growth is apparent from the maps. Based on the peak intensity values of the pole figures, the lower abundance of coarse strongly textured un-recrystallized grains at higher temperature led to lower texture intensity.

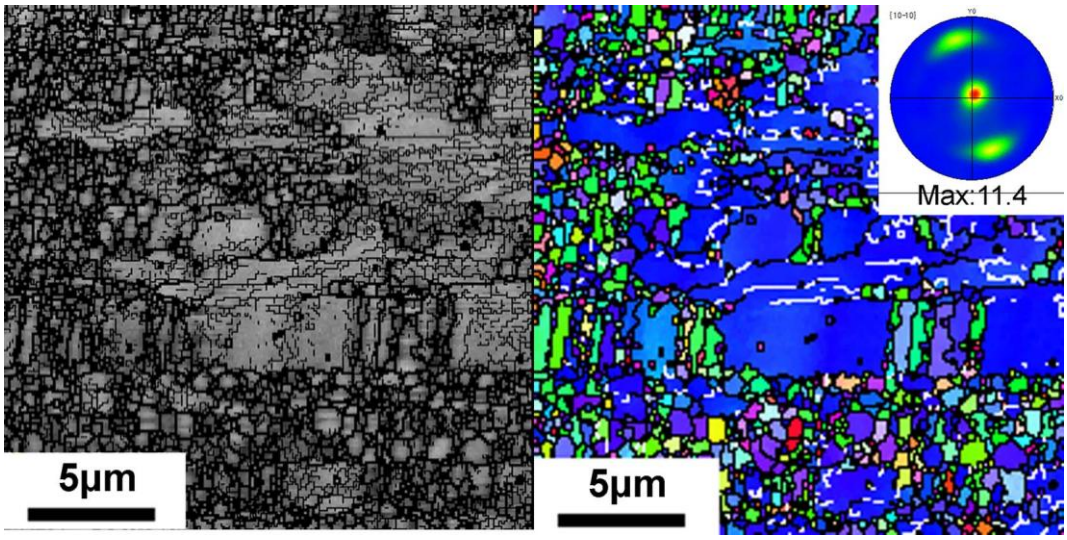

Fig. 4.9 shows higher magnification band contrast image and EBSD IPF-Z orientation maps of TAZ1031 alloy extruded at 250°C and ram speed of 0.1 mm/s and showing coarse strongly textured un-recrystallized grains.

The bimodal grain structure consisting of coarse strongly textured un-recrystallized grains and dynamically recrystallized DRX fine grains of TAZ1031 alloy extruded at low speed and temperature (250°C and ram speed of 0.1 mm/s) is shown in **Figure 4.9**

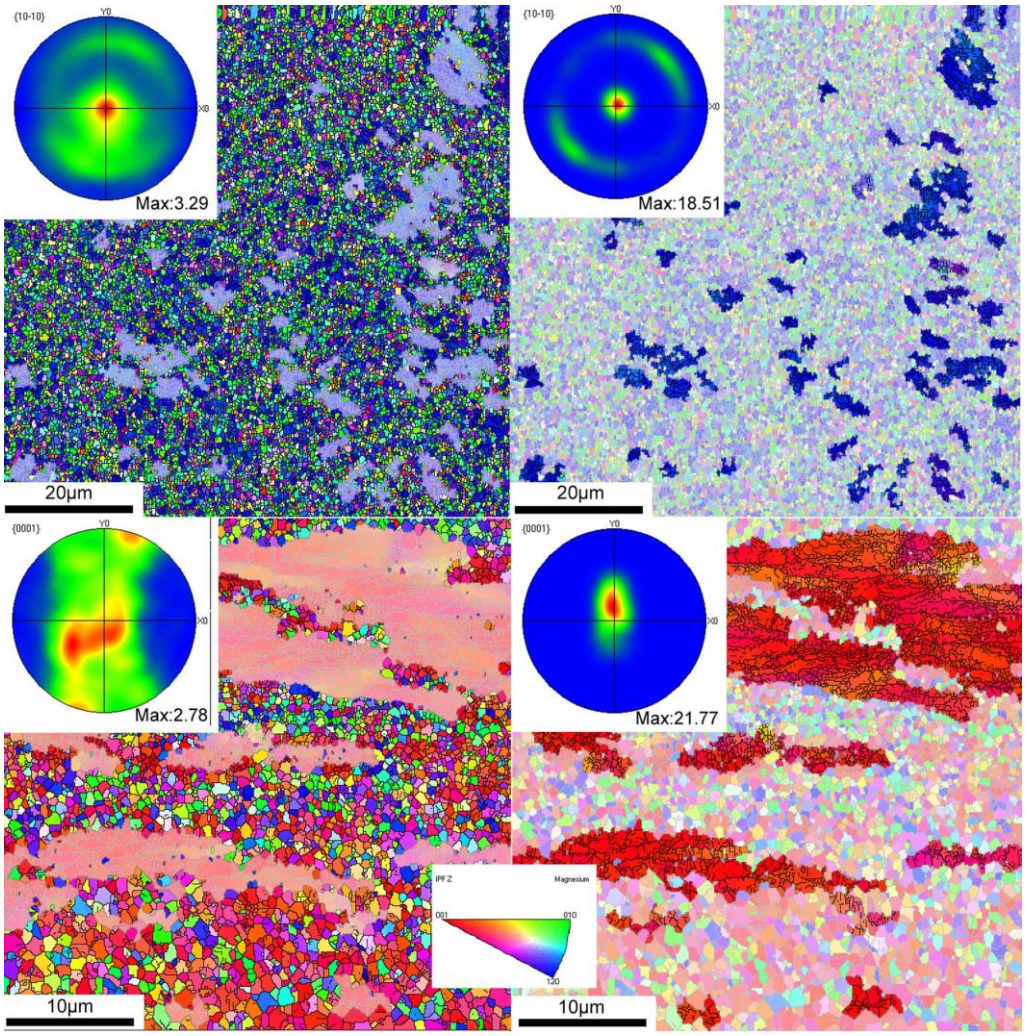

Fig. 4.10 shows EBSD IPF-Z orientation maps of TAZ31 alloy extruded at 250°C and ram speed of 0.1 mm/s showing texture intensities of dynamically recrystallized grains DRX and un-recrystallized grains with inset pole figures showing maximum texture intensities.

The coarse strongly textured un-recrystallized grains exhibit a very strong texture as compared to the dynamically recrystallized DRX fine grains of TAZ1031 alloy extruded at low speed and temperature (250°C and ram speed of 0.1 mm/s). This is shown in the huge difference in texture intensity shown in the inset pole figures.

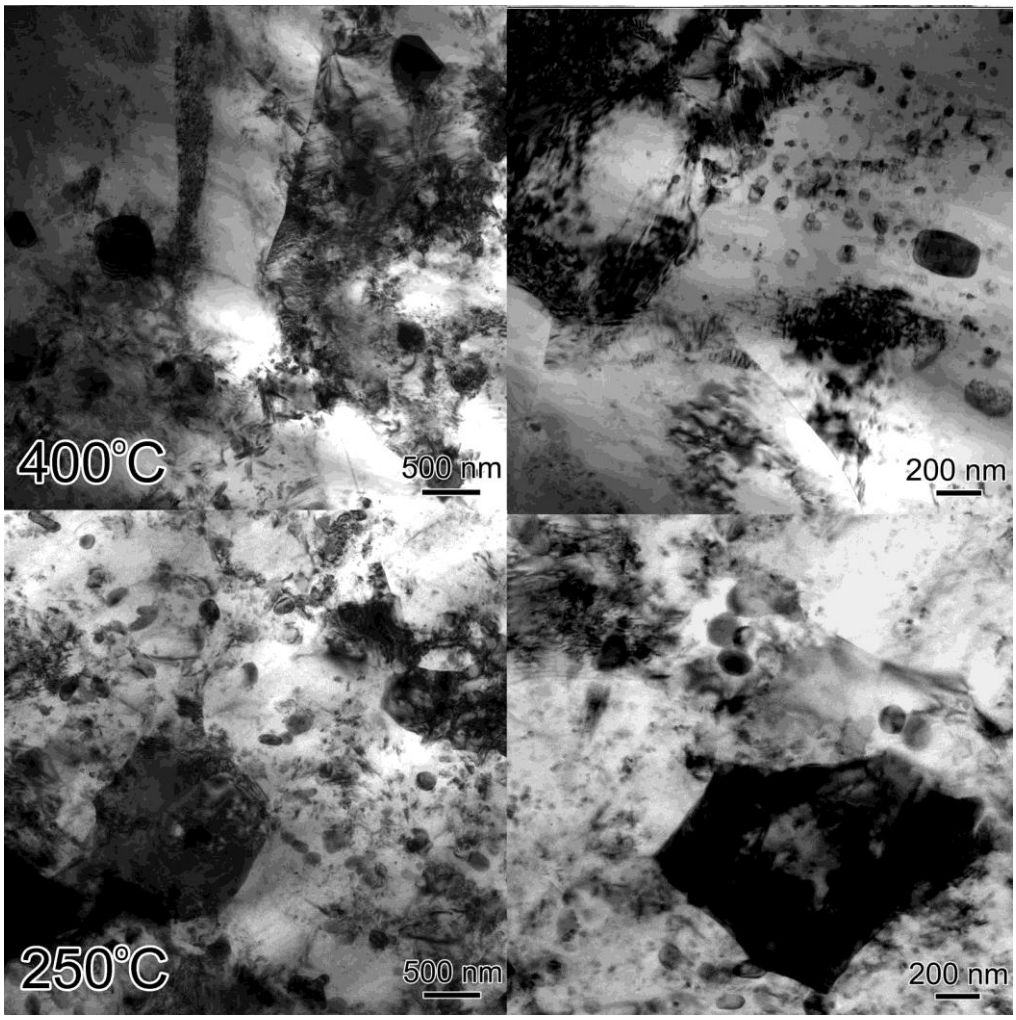

Fig. 4.11 shows TEM micrographs of TAZ1031 alloy extruded at (400°C, 2mm/s) and at (250°C, 0.1mm/s)

The TEM bright field micrographs show the submicron intermetallic Mg_2Sn particles. Mostly the morphology of the precipitates appear globular with a size 50-200nm. The TAZ1031 alloy extruded at condition 1 (250°C, 0.1mm/s) (lower speed/ lower temperature) exhibit the refined submicron grain size shown in figure-13-d. Also the precipitates are refined as compared to TAZ1031 alloy extruded at condition 5(400°C, 2mm/s) shown in figure 4.11

The strong formation of fine precipitates is attributed to dynamic precipitation during extrusion process; especially at lower extrusion speeds, and temperatures where a greater chance

is available for the dynamic precipitation process to take place. The existence of fine Mg_2Sn precipitates assist in pinning grain growth at higher temperatures resulting in the extra effect of refining grain size significantly as compared to AZ31 Mg alloy.

4.3.3 Results TAZ1031-0.1Na extruded alloys

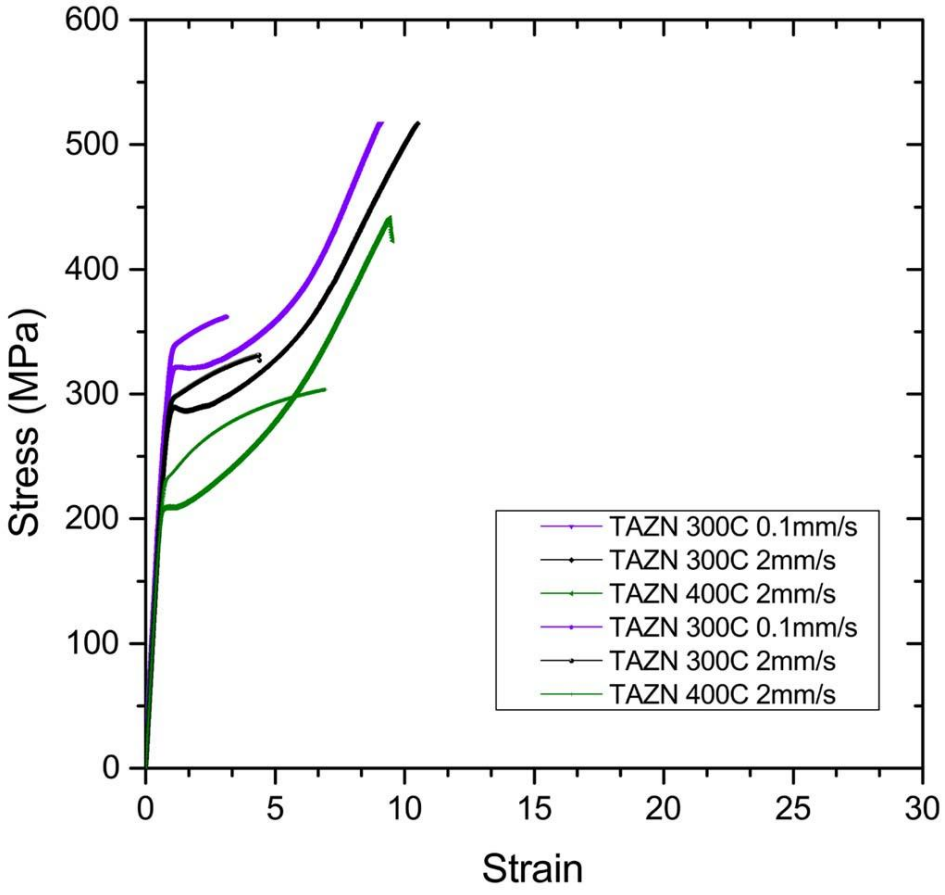

Fig. 4.12 shows Tensile and compression stress-strain curves of TAZ1031 alloys extruded with different conditions

Figure 4.12 shows stress-strain curves for both tension and compression of TAZ1031-0.1Na alloys extruded at T=300°C-400°C, ram speed= 0.1-2mm/s. The σ_{ty} of TAZ1031-0.1Na for T=300°C, ram speed= 0.1 mm/s is enhanced to ~336 MPa but with loss of ε_t to 3.1%. At T=300°C with ram speed of 2 mm/s, σ_{ty} was 292 MPa with ε_t=4.4%, while the extrusion condition of T=400°C and ram speed= 2 mm/s (400°C, 2 mm/s), σ_{ty} was 232 MPa with ε_t=6.9%. The σ_{cy} values range from 209 MPa for T=300°C and ram speed of 2 mm/s to 317 MPa at T=250°C and ram speed= 0.1 mm/s . Compressive elongation values for the TAZ1031-0.1Na alloy were ~10%.

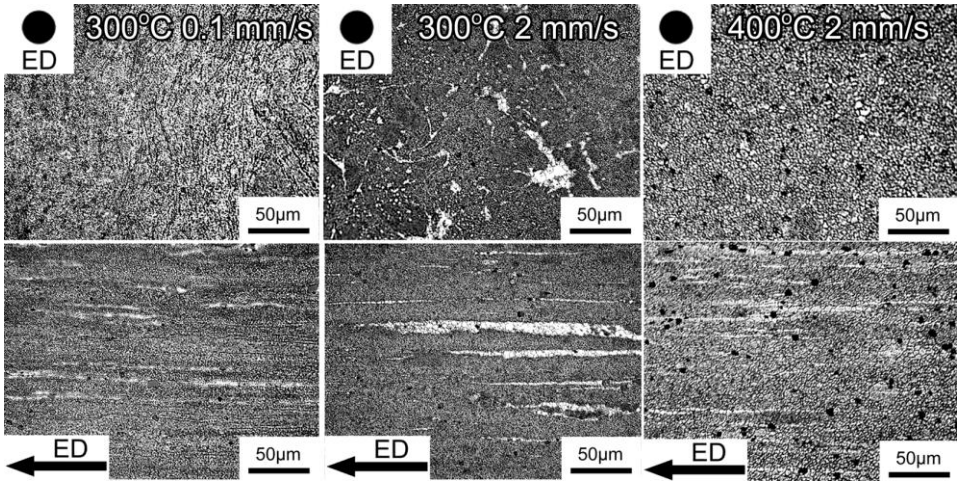

Fig. 4.13 shows Optical micrographs of TAZ1031-0.1Na alloy extruded in the range of conditions in Table 2

Figure 4.13 shows optical micrographs of the TAZ1031-0.1Na alloys extruded at 300°C and 400°C with a ram speed of 2 mm/s to demonstrate the effect of extrusion temperature change. The grain size of the sample extruded at 300°C at a ram speed of 2 mm/s is much smaller than that of the TAZ1031 alloy extruded with the same condition. A slight difference in the grain size is observed between the samples extruded at 300°C to 400°C. The microstructure is similar to that of the TAZ1031 alloy with a refined grain size of dynamically recrystallized (DRX) grains but with a considerably higher fraction of coarse un-recrystallized grain in TAZ1031-0.1Na.

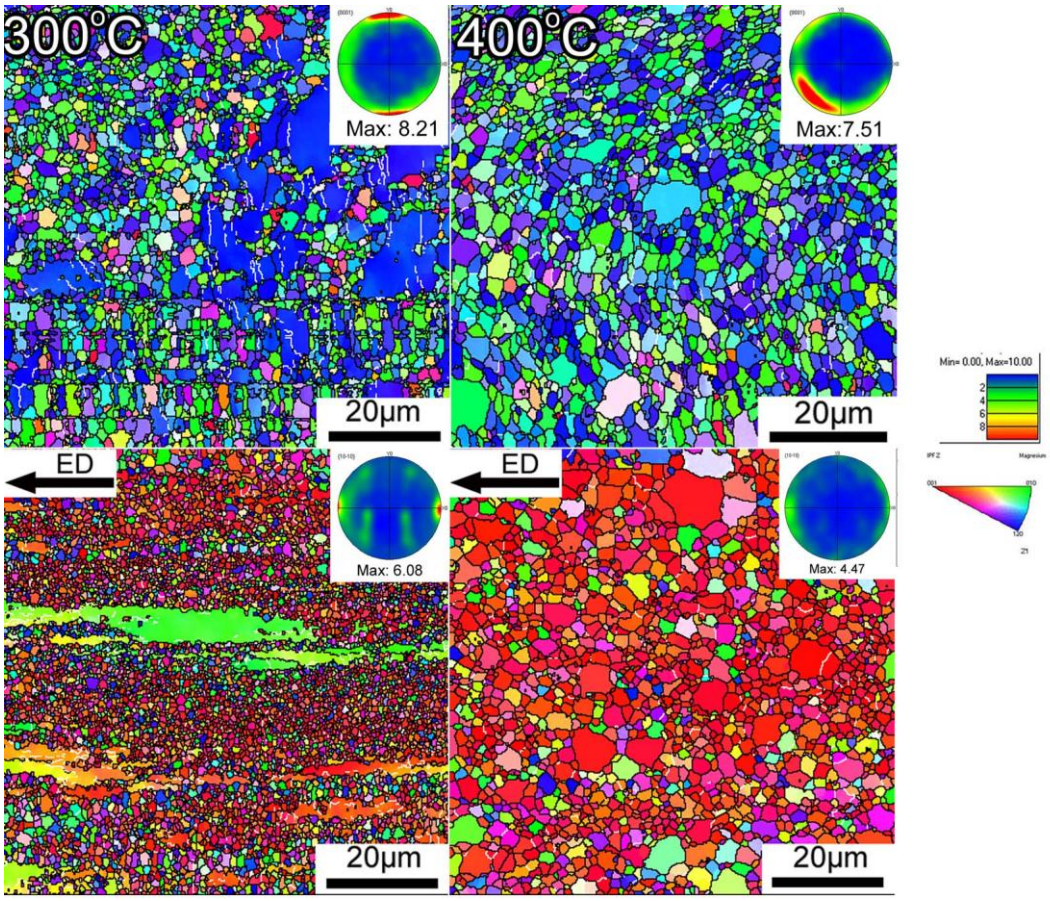

Fig. 4.14 shows EBSD IPF-Z orientation maps of TAZ1031-0.1Na alloy extruded at 300°C and 400°C with a ram speed of 2 mm/s

Figure 4.14 shows EBSD IPF-Z orientation maps of TAZ1031-0.1Na alloy analyzed along extrusion direction ED and extruded at different extrusion temperatures of 300°C and 400°C with a ram speed of 2 mm/s. The orientation maps reveal average grain sizes of 1.0 and 1.6 μm for the extrusion temperatures of 300 and 400°C. It is demonstrated that the fraction of strongly textured un-recrystallized grains at 300°C is higher in the TAZ1031-0.1Na alloy when compared to the TAZ1031 alloy extruded with the same condition. The grain structure at higher extrusion temperature of 400°C is fully dynamically recrystallized (DRX) with no coarse un-recrystallized grains. In similar trend to TAZ1031 alloy, (0001) pole figures show the highest fiber texture intensity at the lower extrusion temperature, and the maximum

intensity is weakened as temperature is increased to 400°C with a more randomly textured dynamically recrystallized (DRX) microstructure. The un-recrystallized grains with the strong prismatic texture are the main source of the strong texture in alloys extruded at lower temperature and speed.

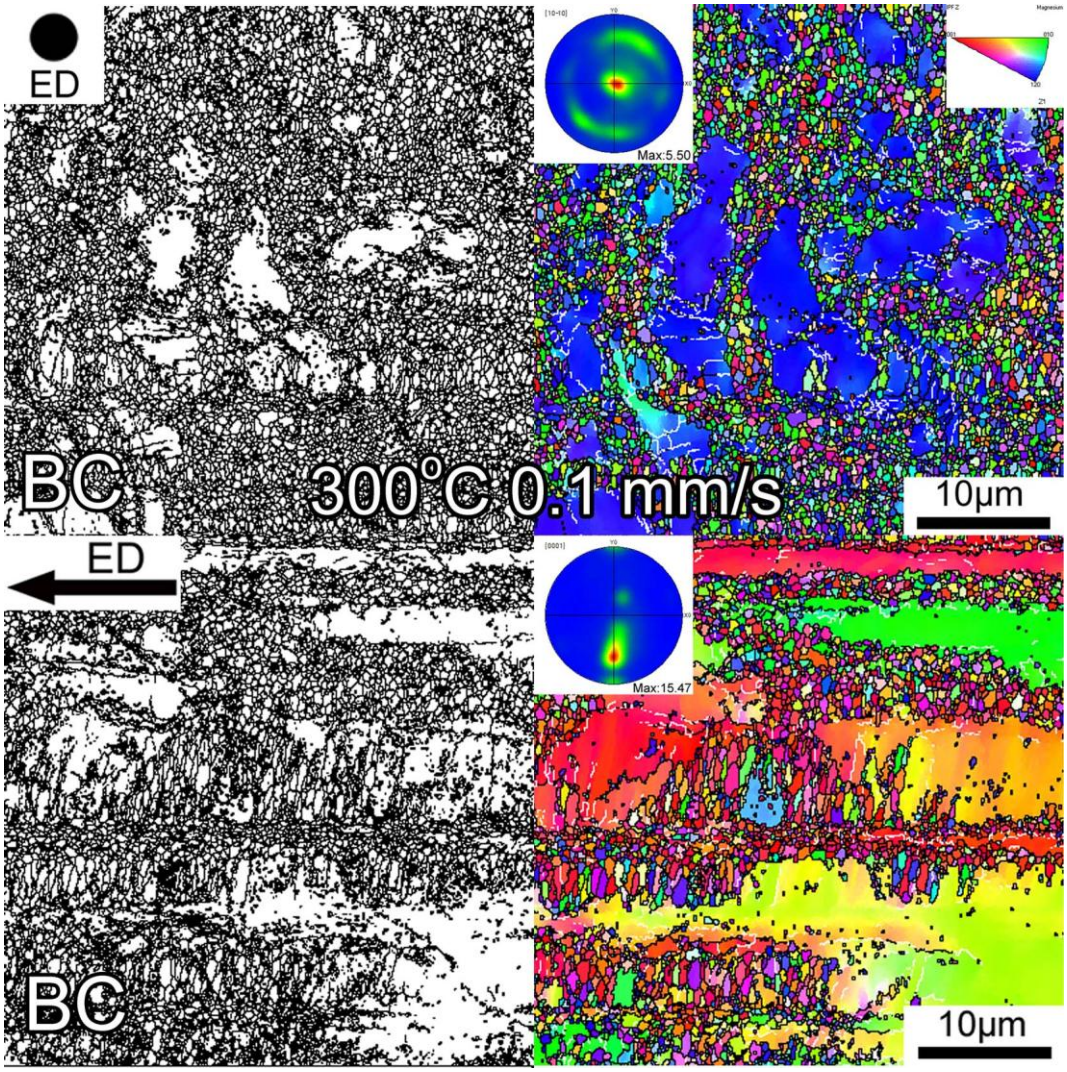

Fig. 4.15 shows band contrast image s and EBSD IPF-Z orientation maps of TAZ1031-0.1Na alloy extruded at 300°C and slow ram speed of 0.1 mm/s

Figure 4.15 shows the strong bimodal grain structure consisting of coarse strongly textured un-recrystallized grains and dynamically recrystallized DRX fine grains of TAZ1031-0.1Na alloy extruded at low speed and temperature (300°C and ram speed of 0.1 mm/s). The

volume fraction of un-recrystallized grains is higher than in the Na free alloy and grain size is refined.

Fig. 4.16 shows TEM micrographs of as extruded TAZ1031-0.1Na alloy extruded at 400C and , ram speed of 2mm/s

Figure 4.16 shows TEM micrographs of TAZ1031 alloy extruded at 400°C and 2 mm/s.

The TEM bright field micrographs show the submicron intermetallic Mg_2Sn particles. The morphology of the precipitates is a combination of cuboidal lath like particles and globular ones with a size 50-200 nm. Note that both grain size and precipitate size are refined in the Na containing alloy with a higher number density of precipitates as compared to TAZ1031 alloy. This is expected since Na clusters act as heterogeneous nucleation sites for Mg_2Sn as reported by previous study **[14].** The formation of the fine precipitates is attributed to dynamic precipitation during extrusion process. The existence of fine Mg_2Sn precipitates assists in pinning grain growth resulting in the extra effect of refining grain size significantly as compared to AZ31 Mg alloy where $Mg_{17}Al_{12}$ phase is not thermally stable at temperatures above 200°C to play a role in pinning grain growth.

4.4- Discussions

Experimental TAZ1031 and TAZ1031-0.1Na were successfully extruded at a variety of extrusion conditions, and the resulting microstructure and mechanical properties were benchmarked with those of AZ31 alloy. The extrusion conditions ranged from 250°C to

400°C with different extrusion speeds ranging from 0.1mm/s to 2mm/s. The AZ31 showed a large grain size change depending on extrusion conditions with notable grain growth with extrusion speed and temperature. On the other hand, the grain size of TAZ1031 and TAZ1031-0.1Na alloys was not so sensitive to the extrusion conditions. This resistance to grain coarsening in the TAZ alloys is attributed to the pinning effect of grains at higher temperature by the dynamic precipitation of Mg_2Sn that occurs during the extrusion process.

Concerning texture evolution, for the AZ31 extruded alloy, the IPF-Z orientation maps as well as the pole figures reveal the typical fiber texture of extruded Mg alloys in which basal poles are preferentially oriented parallel to extrusion direction. The intensity of the fiber texture did not change significantly depending on the ram speed within the range of 0.1-2 mm/s in this study; however, a slight trend of increased intensity with increasing temperature was seen. This could be understood by comparing the Zener-Hollomon parameter, Z, where texture becomes stronger as Z-parameter is decreased at higher extrusion temperature for AZ31. The expected trend is a stronger texture with increasing extrusion temperature based on previous studies on AZ31. **[7,8]**

However, in TAZ1031 and TAZ1031-0.1Na alloys, the texture evolution is more complicated because of the strong effect of un-recrystallized grains in addition to finer dynamically recrystallized grains. When extrusion temperature and speed is increased, the texture intensities are weakened because of the weaker texture in dynamically recrystallized grains, and less abundance of the strongly textured un-recrystallized regions. The huge volume fraction of precipitates in TAZ1031 and TAZ1031-0.1Na alloys play a major role in refining the grain size by pinning the grains preventing grain growth at higher temperature and therefore affecting the texture significantly as a consequence of the refined dynamically recrystallized (DRX) grains and strongly textured un-recrystallized ones.

The mechanical properties of AZ31, TAZ1031and TAZ1031-0.1Na alloys were strongly dependent on extrusion conditions. A summary of the mechanical properties and grain sizes are indicated in **Table 3**.

Table 3 - Mechanical properties of as extruded alloys

Alloy	**T_{ext} °C**	**Extrusion ram speed mm/s**	**TYS**	**UTS**	**ε_T**	**CYS**	**UCS**	**ε_C**	**CYS/TYS**	**d_o µm**
AZ31	250	0.1	189	274	24.9	184	431	15.1	0.97	1.8
AZ31	300	0.1	154	360	23.9	132	386	16.4	0.86	2.3
AZ31	300	1	137	250	23.1	121	379	16.2	0.88	4.3
AZ31	300	2	137	246	21.7	106	368	17	0.77	5.3
AZ31	400	2	154	244	15.7	95	354	17	0.62	9.5
TAZ1031	250	0.1	319	358	6.1	318	523	10.8	1.00	0.5
TAZ1031	300	0.1	289	353	9.1	284	507	11	0.98	0.7
TAZ1031	300	1	241	339	14.5	266	495	11.4	1.10	1.0
TAZ1031	300	2	228	329	13.3	246	476	11.2	1.08	1.0
TAZ1031	400	2	214	315	11.0	206	487	11.2	0.96	2.9
TAZ1031-0.1Na	300	0.1	336	362	3.1	317	532	9.1	0.94	0.4
TAZ1031-0.1Na	300	2	292	331	4.4	284	529	10.4	0.97	1.0
TAZ1031-0.1Na	400	2	232	304	6.9	209	442	9.3	0.90	1.6

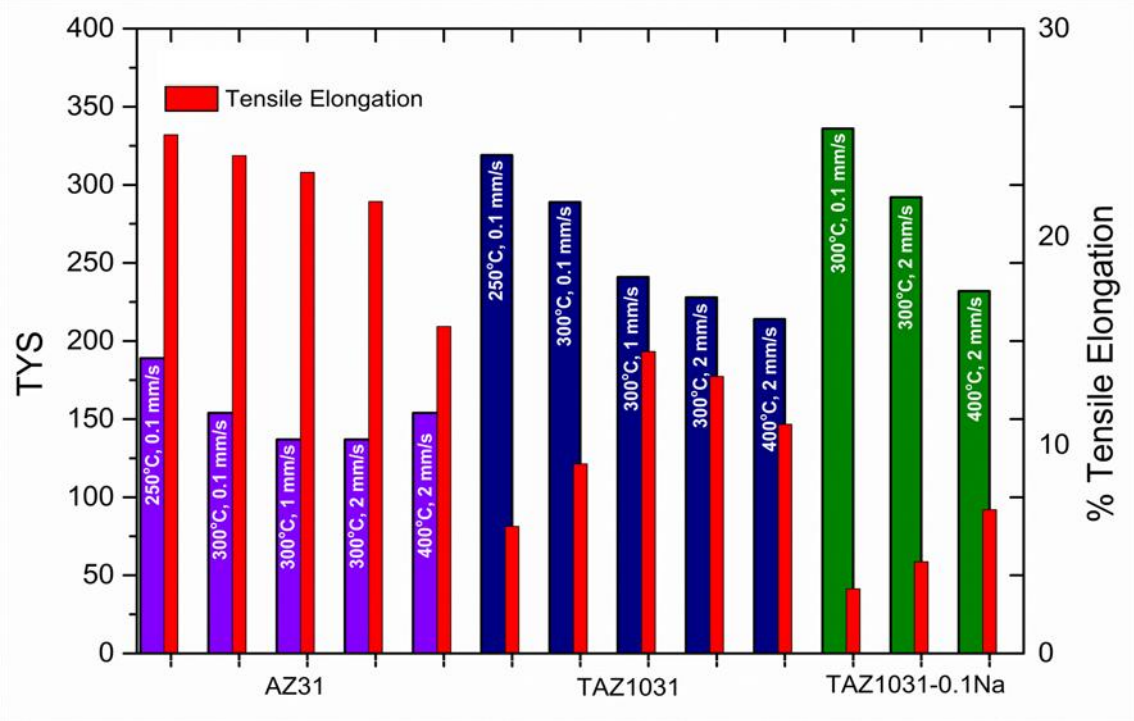

Fig. 4.17 shows summary of mechanical properties in tension for all extrusion conditions in **Table-3**

The resulting higher strength in TAZ1031 and TAZ1031-0.1Na is attributed to several factors: grain refinement, stronger texture, precipitation hardening, as well as solid solution strengthening. The summary of mechanical properties in tension is presented in **figure 4.17**, and the Hall-Petch plot of all the alloys extruded at the different conditions is shown in **figure 4.18**.

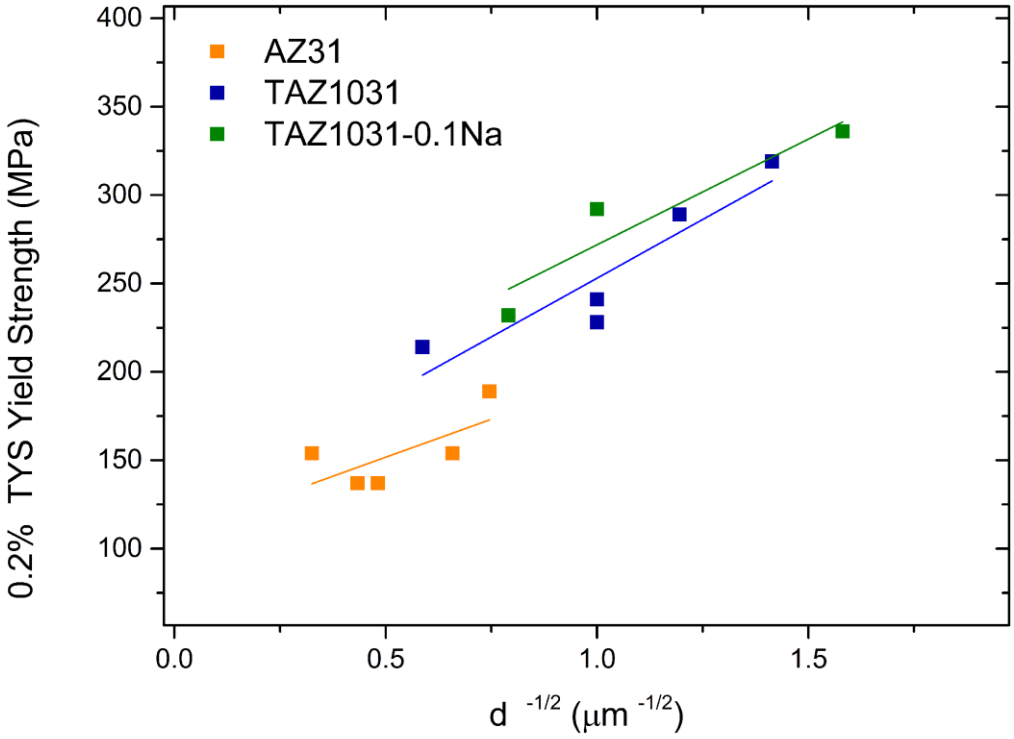

Fig. 4.18 shows Hall-Petch plot of tensile yield strength of all alloys extruded at the different conditions in Table-1

They fall on three parallel Hall-Petch plots for the different alloy families with a clear significant gap between AZ31 and TAZ1031 alloy families data points highlighting the strengthening contributions of precipitation hardening as well as solid solution strengthening. The higher strength of TAZ1031-0.1Na alloys is mainly due to enhanced precipitation hardening. This fact can be demonstrated by the 64 MPa difference between TAZ1031 and TAZ1031-0.1Na both extruded at 300°C, 2mm/s with a similar grain size.

The significant strengthening increment of ~105 MPa between TAZ1031 extruded at 250°C and 0.1mm/s and that extruded at 400°C and 2mm/s can be attributed to grain refinement and precipitation hardening as a significant volume of the fine precipitates are located at grain boundaries in the sample extruded at 250°C and 0.1mm/s. The solid solution strengthening contribution of Sn dissolved in matrix is not expected to exceed 24 MPa based on the c^n power-law estimate in Mg-Sn alloys **[9]**

Yield asymmetry dependence on grain size of all alloys extruded at the different conditions in **Table 3** is illustrated in **Figure 4.19**.

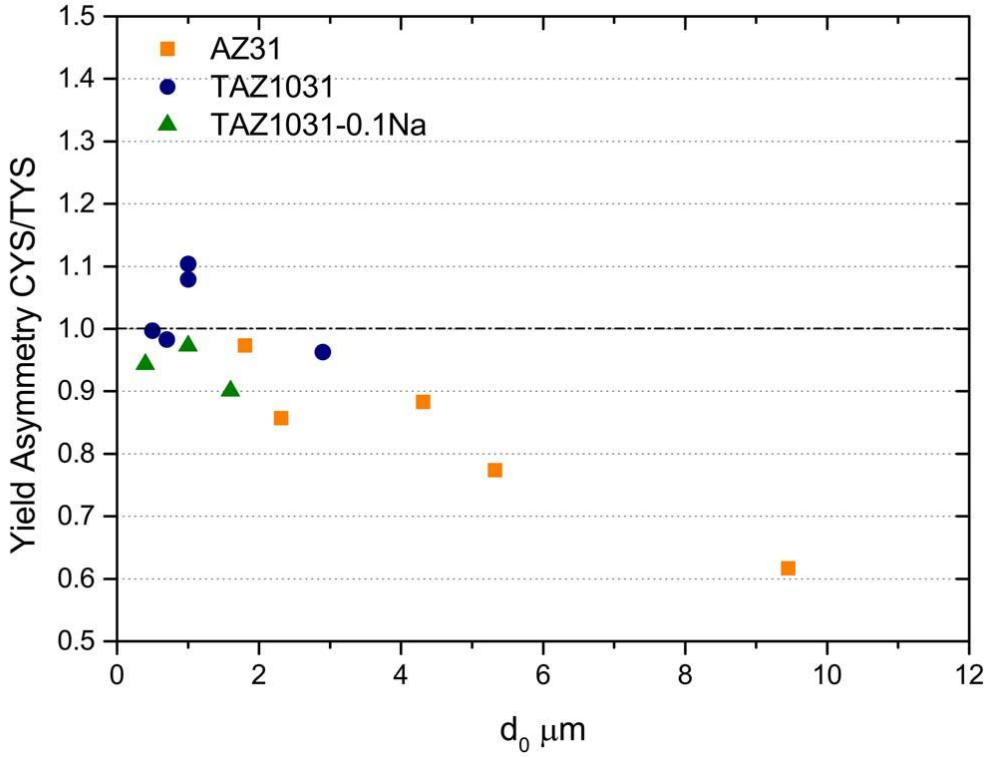

Fig. 4.19 shows Yield asymmetry dependence on grain size of all alloys extruded at the different conditions in Table-2

The asymmetry values denoted as R= σ_{cy}/σ_{ty} exhibited by TAZ1031 and TAZ1031-0.1Na at the different extrusion conditions are all close to unity and all conditions showed asymmetry values R>0.90. For TAZ1031 extruded at T=250°C and ram speed= 0.1 mm/s exhibited R=1 exactly. Yield asymmetry values close to unity of TAZ1031 and TAZ1031-0.1Na alloys are an attractive feature in forming of wrought Mg alloys. The yield asymmetry between compression and tension σ_{cy}/σ_{ty} values for extruded AZ31 range between ~0.62 for T=400°C and ram speed= 2 mm/s and is increased to a value closer to unity ~0.97 for T=250 °C and ram speed= 0.1 mm/s. It is widely known that yield asymmetry in extruded Mg alloys

are highly dependent on texture and grain size as well as presence of precipitates. **[10].** The yield asymmetry variation in AZ31 alloy is in line with previous studies **[7]**; nevertheless in this study, an interesting observation is the reduction of yield asymmetry in AZ31 to a value very close to unity at lower extrusion temperature of 250°C and slower extrusion speed of 0.1 mm/s as shown in **Figure 11**. This is attributed to the strong grain refinement at lower extrusion speed and temperature suppressing twining activity, which is the main cause for amplifying the yield asymmetry. **[10,11]**

In the TAZ1031-0.1Na alloy, the number density of the precipitates is larger, and the precipitate size is clearly refined as compared to the TAZ1031 alloy. The increased occurrence of finer precipitates in the TAZ1031-0.1Na gave a stronger grain-pinning effect, and prevented grain growth at higher extrusion temperature of 400°C as clearly observed from the TEM micrographs. The strong effect of Na on enhancing Mg_2Sn precipitation has been demonstrated as Na clusters act as nucleation sites for Mg_2Sn precipitation and enhance the kinetics significantly. **[6]**

The precipitate morphology in the TAZ1031 alloy is more spherical than in the TAZ1031-0.1Na alloy where a huge occurrence of cuboidal block-shaped precipitates is seen in addition to the spherical precipitates; The first might be attributed to only dynamic precipitation, whereas in the later it might be also enhanced static precipitation in the Na containing alloy within the billet soaking time just after extrusion. This could be understood in line with the fact that Na additions greatly enhance the precipitation kinetics. These observations are in agreement with previous studies of Na containing Mg-Sn alloys **[12,13]**. The enhanced strength levels in the TAZ1031-0.1Na alloy is easily attributable to the enhanced dynamic precipitation phenomena caused by Na micro-alloying additions.

Since a huge loss in ductility was observed in the Na-doped alloy, failure analysis was performed to examine failure mode by carrying out fractography of tensile samples of

the (highest strength- least ductile) conditions showing 3~6% tensile elongation for the Na-doped and Na-free samples respectively. The fracture surfaces of tensile test samples prepared from extruded bars of TAZ1031 extruded at (250°C and 0.1mm/s) and TAZ1031-0.1Na extruded at (300°C and 0.1mm/s) are shown in **Figure 4.20**. The fracture surface of the TAZ1031 alloy exhibits ductile fracture features with cracks and ductile dimples formed by coalescence of micro-voids clearly visible at higher magnification. On the other hand the fracture surface of TAZ1031-0.1Na alloy show features of inter-granular failure with clear edges of fracture, multiple fine ridges, and river marks in between coarser un-recrystallized grains. All these features indicate a strong brittle failure in line with the low tensile ductility of 3.1% exhibited by the Na-doped alloy in this low speed and lower temperature extrusion condition.

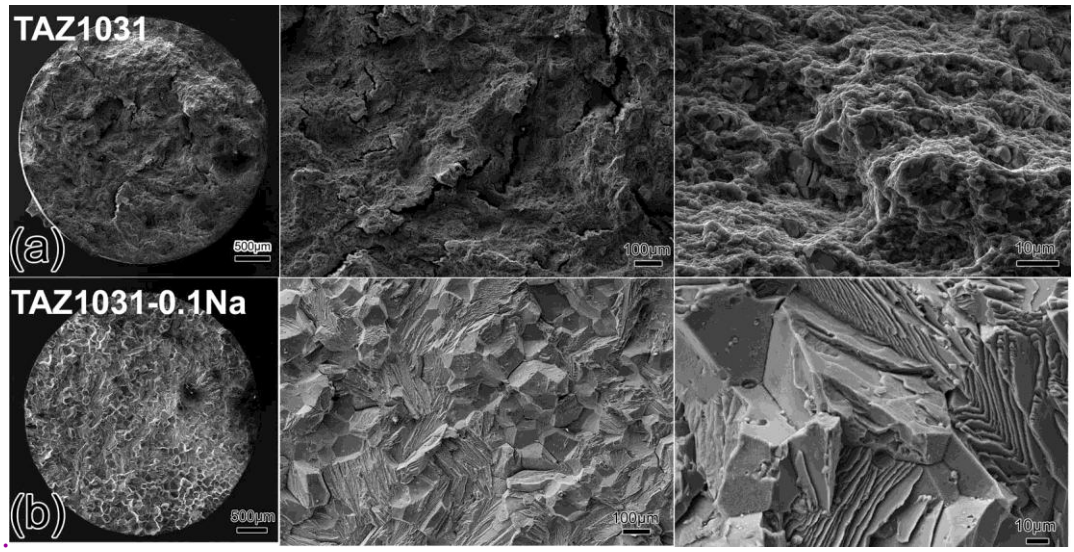

Fig. 4.20 shows Fractography of tensile samples of a) TAZ1031 alloy extruded at Condition 1 (250C, 0.1mm/s),b) TAZ1031-0.1Na alloy extruded at Condition 2 (300C, 0.1mm/s)

The possible explanation for the reduced ductility in the extruded TAZ1031-0.1Na is the Na embrittlement effect; whereas the most probable mechanisms are either grain boundary segregation or crack facilitation by Na atoms adsorbing on internal crack surfaces

and defects facilitating crack propagation, and reducing ductility during deformation. **[14]** The effect is known in Al alloys due to presence of Na trace levels, but the Na embrittlement can by suppressed in commercial Al alloys as silicon immobilizes Na by forming ternary Na-Al-Si compound. In the case of our micro-alloyed Mg-Sn alloys, it appears that the level of 0.09 wt% Na employed is high enough to leave sufficient amount of elemental Na free to adsorb on internal free surfaces and cause the harmful embrittlement effect; even-if a high fraction of the micro-alloying addition is co-clustering with Sn atoms enhancing the nucleation of Mg_2Sn precipitates.

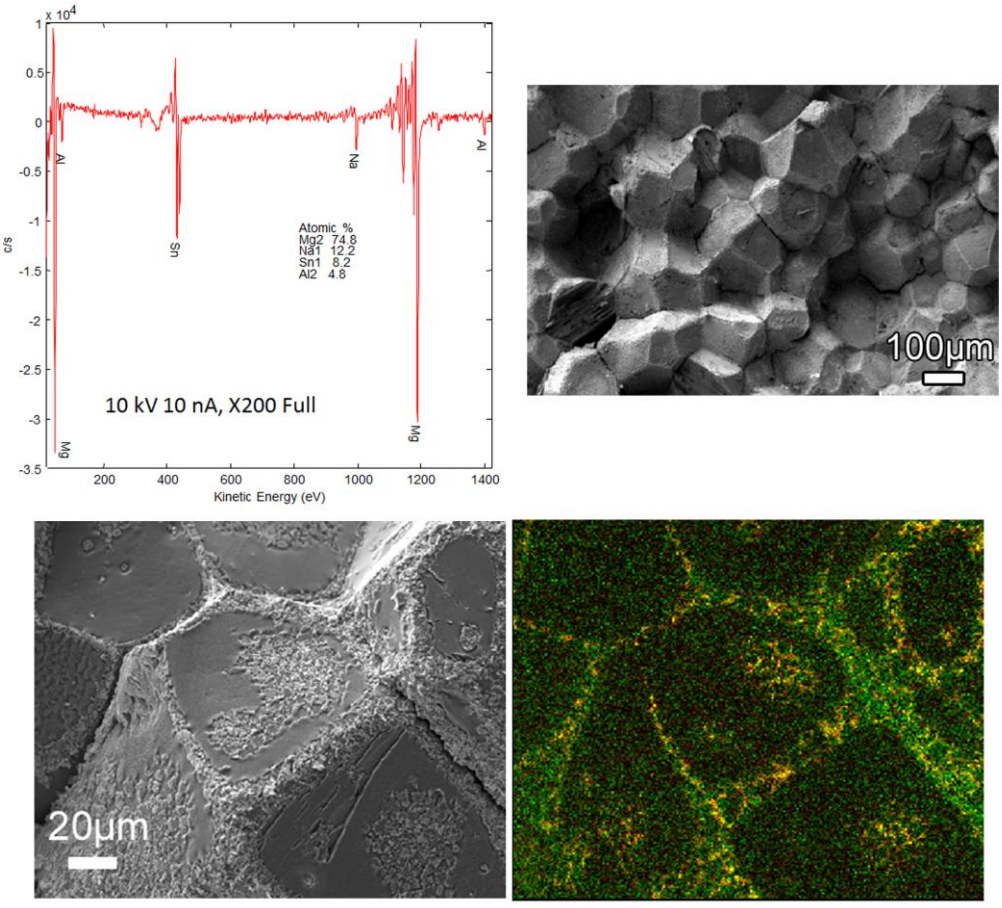

Fig. 4.21 shows Auger spectroscopy analysis of fractured surface of post extrusion T6 treated TAZ1031-0.1Na alloy of the lowest ductility extrusion condition (300C, ram speed of 0.1mm/s)

In order to elucidate the role of Na in causing the embrittlement effect and reduced ductility, Auger Electron spectroscopy was performed on fracture surface under high vacuum on a post extrusion-T6 treated TAZ1031-0.1Na sample that showed a severe reduction in ductility in as extruded state. The results shown in figure 4.21 give evidence of Na segregation at grain boundaries confirming the hypothesis. The Na segregation trend was confirmed by examining the Na compositions of multiple analysis points as well as chemical mapping of the surface directly after fracture in addition to 20nm in depth area after Ar-ion milling 20nm off the fracture surface. The result confirms Na segregation into grain boundaries.

4.5- Summary and conclusions

The effect of different extrusion conditions on AZ31, TAZ1031, and TAZ1031-0.1Na has been studied, and correlated to the final microstructure, texture, and mechanical properties. The TAZ1031 alloy showed low yield asymmetry and a versatile strength-ductility combination ranging from medium to high strength tailored by the extrusion processing conditions. The TAZ1031-0.1Na alloy shows further enhanced tensile yield strength of~336 MPa, which is a new strength milestone for a low cost RE-free Mg-Sn alloy without using expensive alloying elements, but the absence of sufficient ductility may be detrimental to commercial attractiveness as to mainstream structural components. For a future strategy to further improving the strength-ductility combination, it might be useful to explore the potent effect of Na micro-alloying in enhancing the age hardening without sacrificing too much ductility. Adjusting Sn composition as well as adding other alloying elements that could act as scavengers for Na or interact with free Na could be a strategy to explore in future works to alter the strength-ductility combinations attainable.

References

[1] W.L. Cheng , H.S. Kim , B.S. You , B.H. Koo , S.S. Park, Mater. Lett. 65 (2011) 1525–1527

[2] T.T. Sasaki, K. Yamamoto, T. Honma, S. Kamado and K. Hono, Scripta Mater. 59 (2008) 1111–1114

[3] S.S. Park, and B.S. You, Scripta Mater. 65 (2011) 202–205

[4] S.S. Park , W.N. Tang, B.S. You, Mater. Lett. 64 (2010) 31-34

[5] F. R. Elsayed, T.T. Sasaki, C.L.Mendis, T. Ohkubo, and K. Hono, Mater. Sci. Eng. A, 566 (2013) , pp. 22-29

[6] F. R. Elsayed, T.T. Sasaki, C.L.Mendis, T. Ohkubo, and K. Hono, , Scripta Mater. 68 (2013) 797–800

[7] S.S.Park, B.S.You, and D.J.Yoon, J. Mater. Process. Technol.209 (2009) 5940-5943

[8] K. Hazeli, A. Sadeghi, M.O. Pekguleryuz, A. Kontsos, Mater. Sci. Eng. A, (2013) http://dx.doi.org/10.1016/j.msea.2013.04.101

[9] B.Q. Shi, R.S. Chen, W.Ke, J. Alloys Compd. 509 (2011) 3357-3362

[10] M.R. Barnett, Scripta Mater. 59 (2008) 696–698

[11] J. Jain, W.J. Poole, C.W. Sinclair, and M.A. Gharghouri, Scripta Mater. 62 (2010) 301–304

[12] C.L. Mendis, C.J. Bettles, M.A. Gibson, C.R. Hutchinson, Mater. Sci. Eng. A 435 (2006) 163–171

[13] N. Stanford, J.R. TerBush, M. Setty, M.R. Barnett, Metall. Mater. Trans. A 44 (2013) 2466-2469

[14] D.E.J. Talbot ,and C.E. Ransley. Metall. Trans. A 8A (1977) 1149-1154

Chapter 5 - Further Mg-Sn-Zn-Al Alloy optimization

5.1-Introduction

The prospect of further strengthening the alloys post extrusion by (T5)-[cooled and artificially aged] or (T6)-[solution treated and artificially aged] treatments was examined. However examining the relatively high solution treatment (T4) temperature of 525°C **[1-3]** in the high –Sn containing (10 wt %) alloys as shown in Figure 5.1 was necessary to make the the process more industrially practical by avoiding excessive surface oxidation and by minimizing excessive grain growth during the solution treatment.

For this reason and with the aim to reduce the solution treatment temperature required to have a supersaturated solid solution, Sn composition was reduced, and Zn macroalloying was performed by increasing the Zn content to substitute for less strengthening due to lower Sn content by larger precipitation of the $MgZn_2$ strengthening precipitate in addition to the Mg_2Sn precipitate. As a result T4 solution treatment temperature could be lowered to 450°C as shown in Figure 5.1.

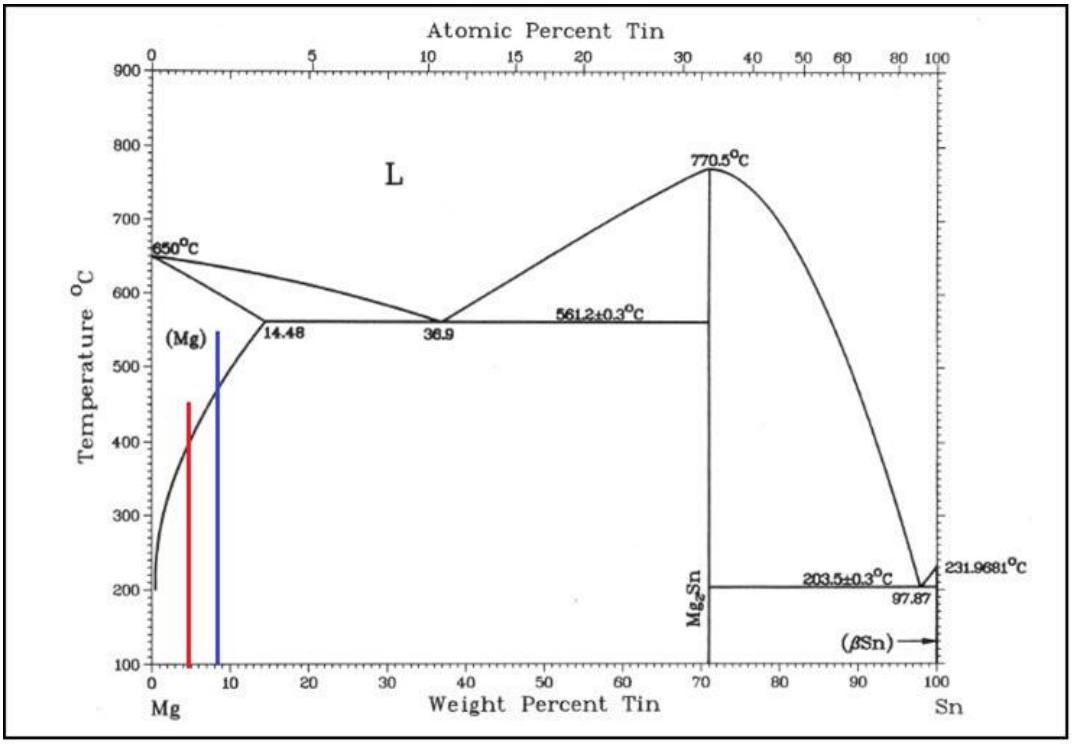

Figure 5.1: a) Mg-Sn phase diagram showing the corresponding T4 solution treatment temperatures for the high Sn (2.2 at %) in blue-525°C, and low Sn (1.2at %) in red-450°C C alloys respectively.

Unlike Mg-Zn and Mg-Al based precipitation hardenable wrought alloys, the Mg-Sn based alloy is difficult to strengthen by T5 aging since Mg_2Sn phase precipitates out during extrusion **[4]**. The T6 aging comprised of solution treatment and artificial aging does not work effectively either for the Mg-Sn system **[5]**. Since the previously studied Mg-9.8 wt% Sn based alloy needed to be solution treated above 500 °C **[1, 2]**, the grains abnormally grow during the solution treatment, and thereby precipitation hardening step is not effective. Therefore, a research attempt was undergone focused on achieving high strength level by inhibiting excessive grain growth during solution treatment in conjunction of an enhanced age hardening response using the macro/microalloying previously used strategy with the final aim of enhancing the yield strength by subsequent artificial aging.

5.2 Experimental

Experimental alloy ingots were prepared by induction melting using steel crucibles under an Ar atmosphere and were cast into steel molds. Chemical analysis of cast billets was performed using ICP-OS including Fe trace analysis to ensure sound chemical composition. Na additions were produced in the form of Sn-Na master alloy induction melted inside inert Quartz tubes also under Ar atmosphere, and later added in master alloy form. The nomenclatures of the alloys and their compositions in both at.% and wt.% are shown in Table 1. Hereafter, all alloy compositions are described in wt.%. The ingots were homogenized at 500^{o}C for 48 h in a He-filled Pyrex tube. Small section-samples were cut out from the ingots, and were solution treated at 525^{o}C for 1 h, and water quenched. Artificial aging was performed at 200^{o}C and 160^{o}C in a silicone oil bath for various aging times immediately after solution treatment. The age hardening response was measured by a Vickers hardness tester under a 500g load, and a minimum of 8 indentations where measured to obtain the aging curves. Transmission electron microscope (TEM) specimens were prepared by punching 3 mm discs, mechanical polishing, and ion-milling using the Precision Ion Polishing System (GATAN691). TEM observation was carried out using FEI Tecnai 20 TEM operating at 200 kV.

5.3 Results and Discussions

5.3.1 Post Extrusion Heat Treatment

T5 Treatment

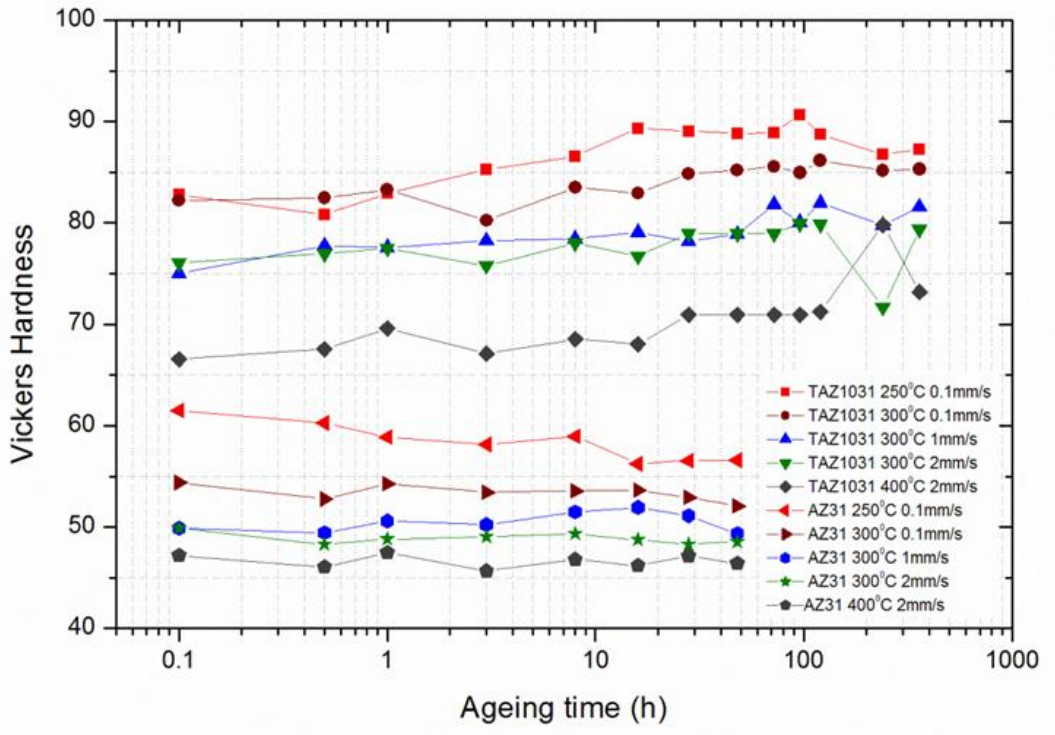

Figure 5.2: a) T5 ageing curves for TAZ1031 and AZ31 extruded alloys,

Figure 5.2 shows TAZ1031 and AZ31 extruded alloys subjected to T5 treatment post extrusion. The post extrusion heat treatments applied are shown in Figure 5.2 with the Vickers hardness curves of different alloys in T5 and T6 conditions. Both TAZ1031 and AZ31 alloys showed no improvement in hardness values when subjected to the T5 treatment at 200ºC. For the TAZ1031 alloy, some extruded samples showed a very small increment of ~5 HV upon the T5 treatment.

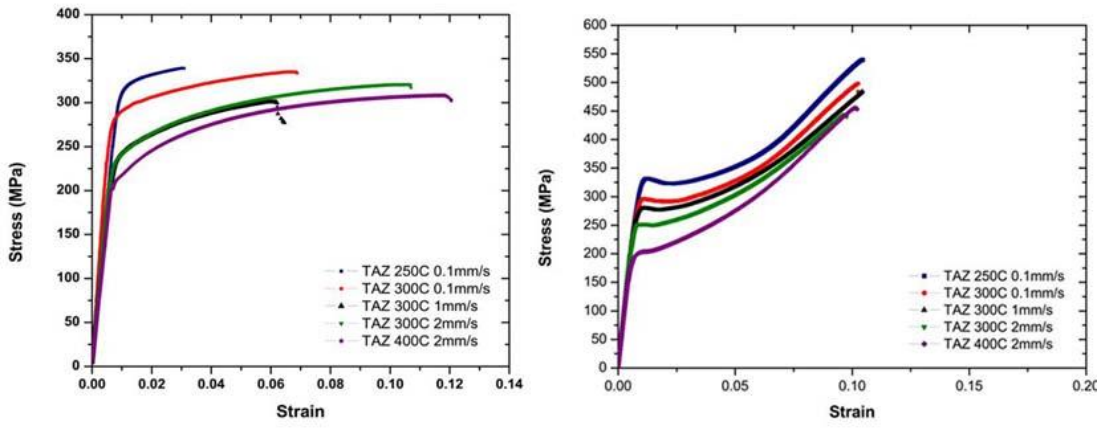

Figure 5.3: Mechanical properties of T5 treated TAZ1031 extruded alloys at 200ºC.

This observation was confirmed after examining the mechanical properties of T5 treated TAZ1031 alloy at 200ºC shown in Figure 5.3 where no improvement in mechanical properties was shown. The result show that the hardening response is quiet poor ~5HV or non-existent leading to conclude that the TAZ1031 alloys do not respond to T5 treatment favorably.

T6 Treatment

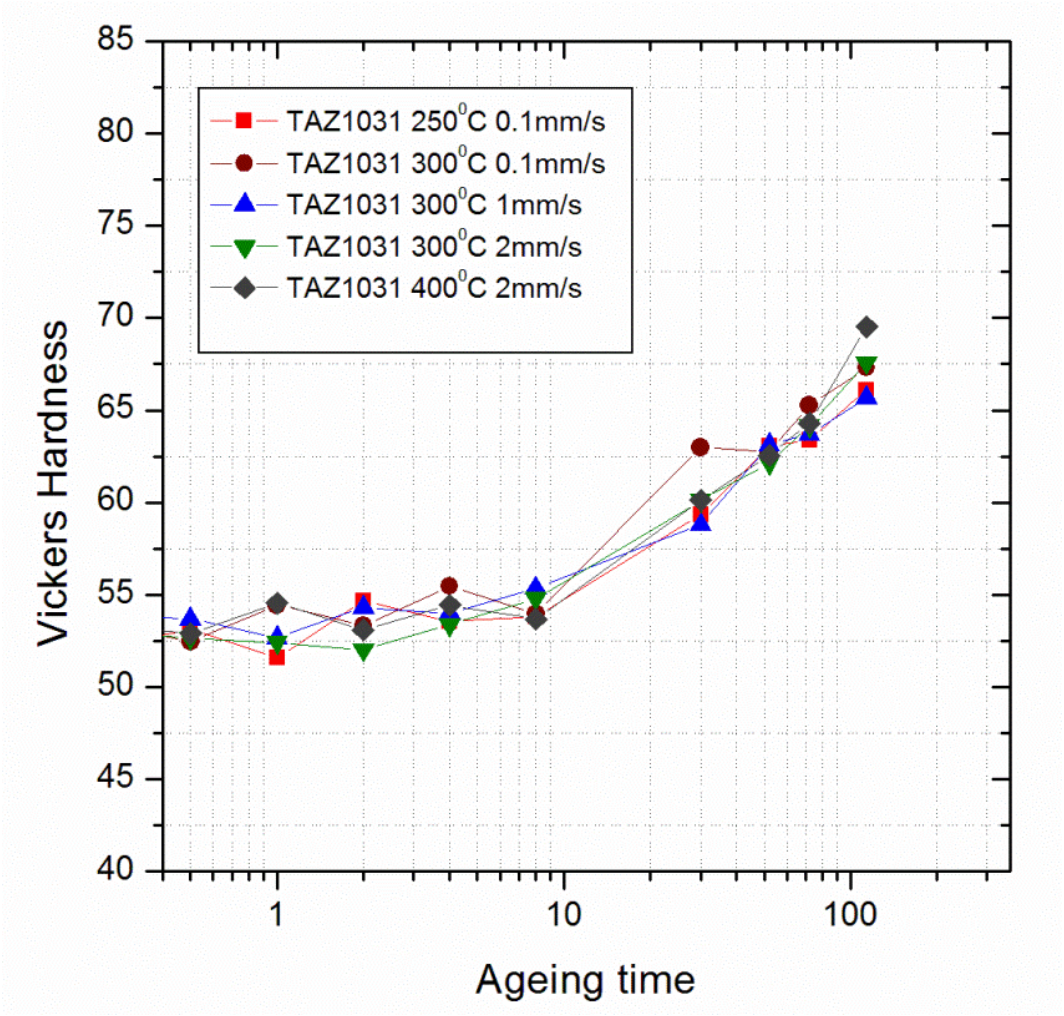

Fig 5.4: ageing curve for heat treated different extrusion samples of TAZ1031 alloy aged at 200ºC

Figure 5.4 show the post extrusion T6 treatment performed on TAZ1031 extruded alloys at 200ºC to examine any improvement in property. The solution treatment was performed at 525ºC for 30 min followed by quenching in water. The as quenched hardness values were reduced from the as extruded higher values shown in Figure 5.1 to~53 HV for all alloys. Upon ageing hardness values were increased only to~70HV after 100h of ageing, which is

not as high as~ 84HV as in the case of low temperature extruded condition of 250ºC. This suggests that TA1031 alloys do not respond well to T6 treatment post extrusion.

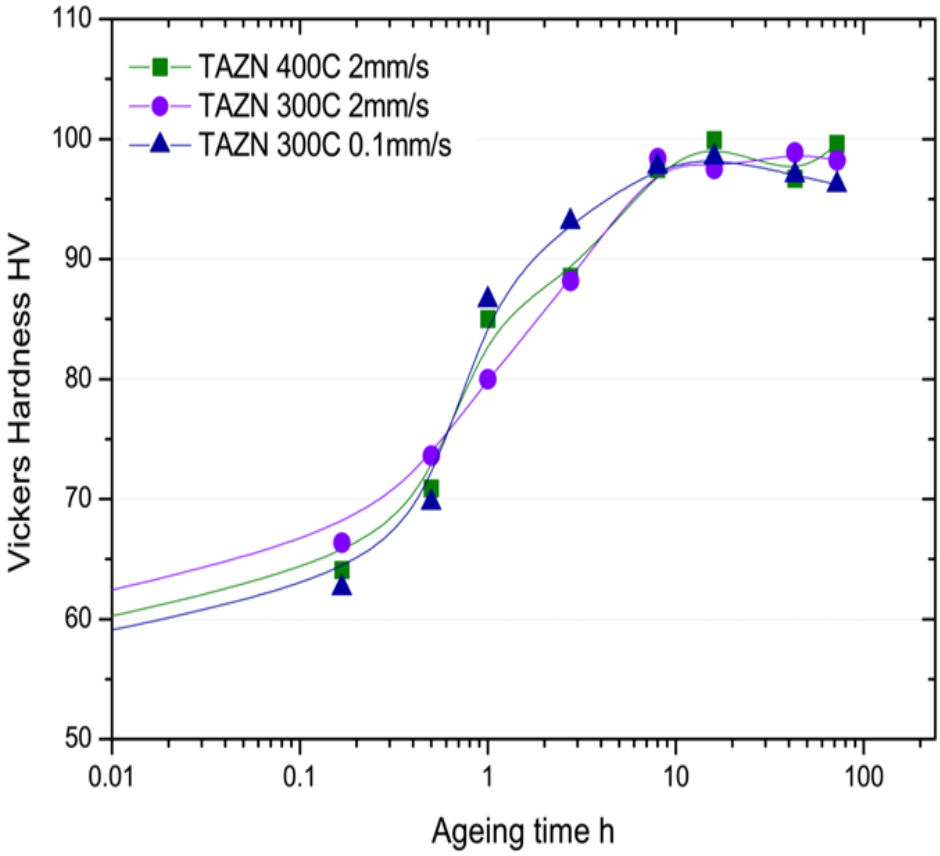

Fig 5.5:Ageing curve for heat treated different extrusion samples of TAZ1031-0.1Na alloy aged at 200ºC

In a similar approach, post extrusion T6 at 200ºC treatment was performed on the Na micro-alloyed (TAZ1031-0.1Na) extruded alloys to examine if Na additions can enhance the age hardening response post extrusion. The solution treatment was performed at 525ºC for shorter time of 15 min in an attempt to avoid excessive grain growth, followed by quenching

in water. The results shown in figure 5.5 showed significant enhancement in the ageing response up to~100 HV in a relatively short time of 10h.

5.3.2 Low Sn alloy optimization

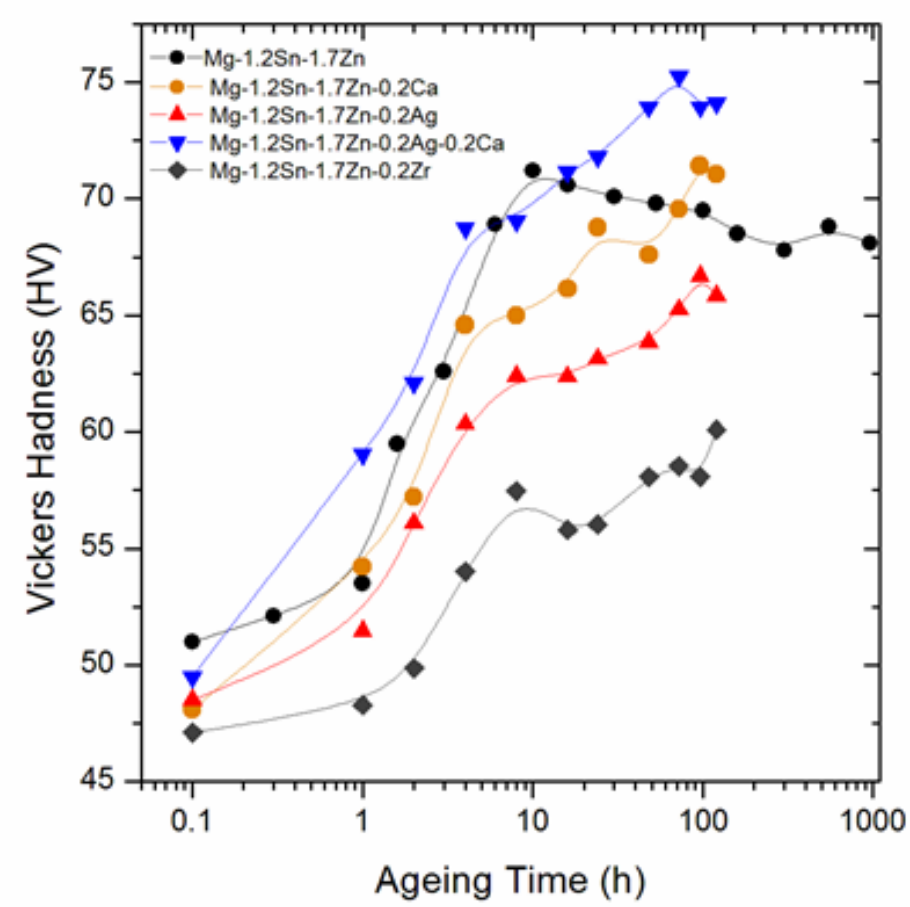

Fig 5.6: Ageing curve at 200C for heat treated different quaternary microalloying additions to the Mg-1.2Sn-1.7Zn at% alloy (T6 at 200ºC)

The alloy design approach for developing low Sn alloy was undergone in a similar fashion as in chapter (2) with the high Sn alloy (TAZ1031). The Mg-1.2Sn-1.7Zn at% was micro-alloyed with several microalloying elements, as well as macro-alloyed with Al to investigate positive effect on ageing response. The ageing curves are shown in figure 5.6 –(micro-alloying effect) and figure 5.7- (macro-alloying with Al).

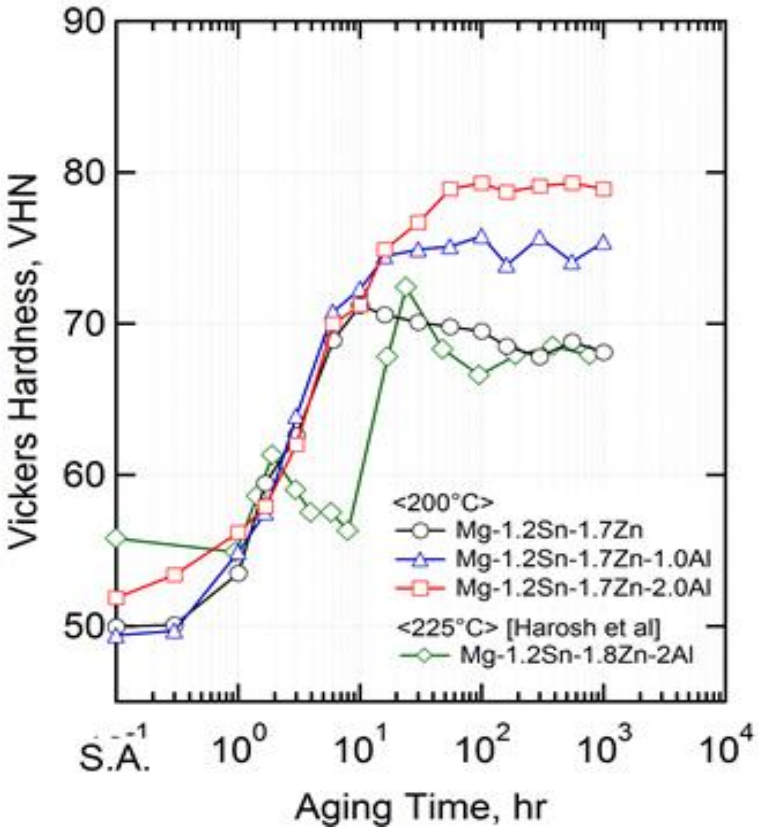

Fig 5.7: Ageing curve at 200ºC for Mg-1.2Sn-1.7Zn at% alloy macro-alloyed with Al

As shown in Figure 5.7, macro-alloying with 2at% Al was successful in enhancing the ageing response to ~ 80 HV, very similar level to formerly developed high Sn- TAZ1031 alloy.

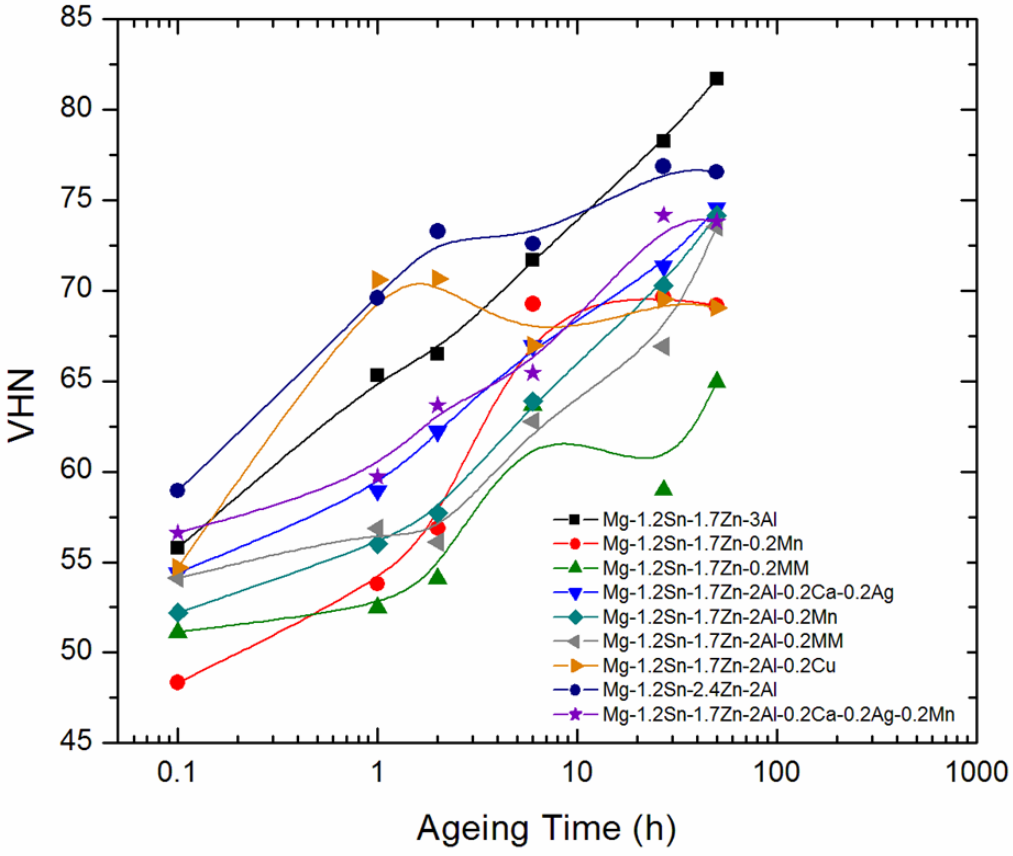

Figure 5.8: Ageing Curves at 200°C of Mg-Sn-Zn-Al alloy with different micro-alloying elements

Various amounts of microalloying elements such as combinations of Ca+Ag, MM (Misch Metal), Mn, Cu as well as higher Zn and Al macro-alloying content were added to investigate their effect on enhancing the peak age achievable. Increasing the Al content up to 3at% gave the highest peak hardness level among all the other elements micro-alloying attempts. However a decision to not increase the Al content above 2at% was taken to keep the alloy from being excessively alloyed in an attempt to enhance extrudability taking into consideration peak age level was not significantly superior comparing the 3at% additions to the 2at%. Instead a decision to increase the Sn content slightly to 1.5at%Sn and Zn content to 2.4at% Zn to increase strength level achievable was undergone to give the final alloy composition of Mg-1.5Sn-2.4Zn-2Al at%.

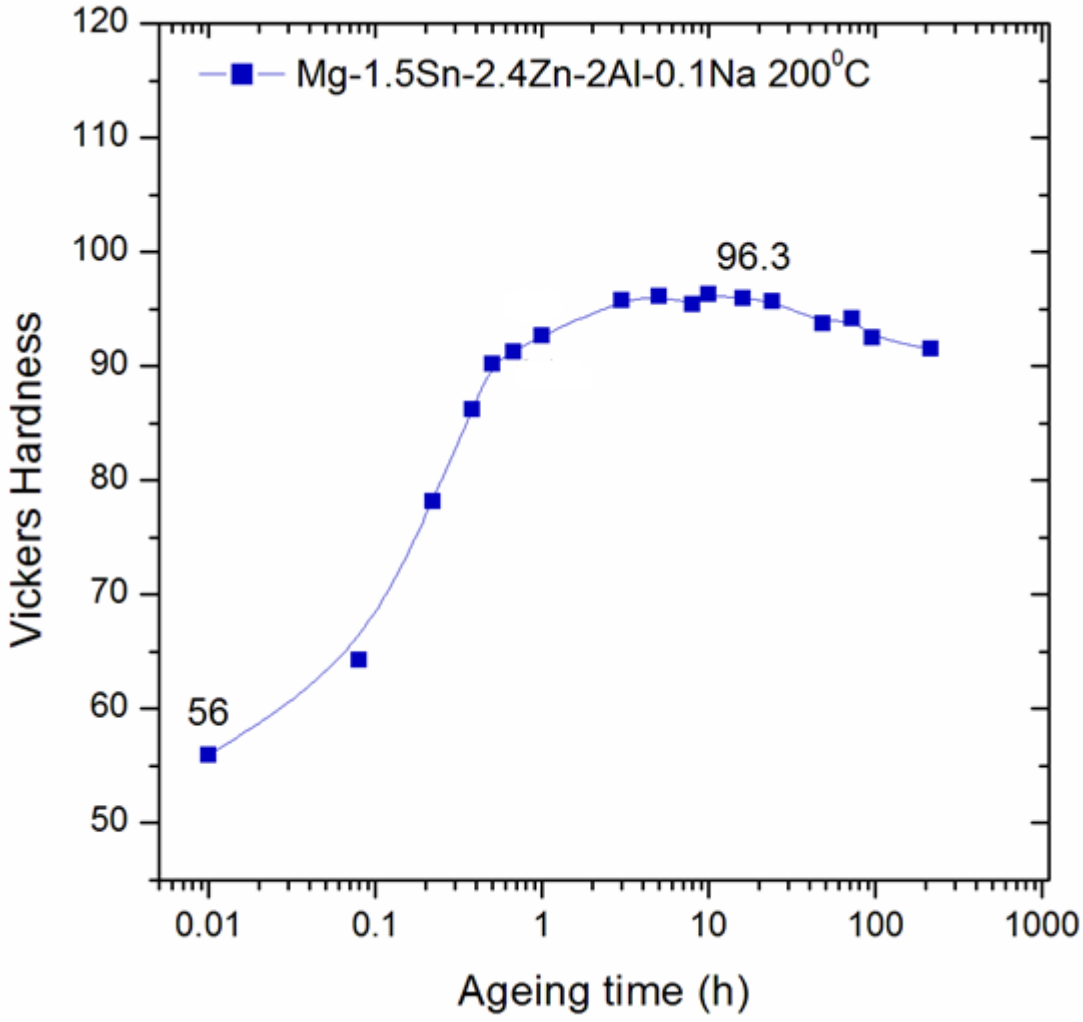

Fig 5.9: Ageing curve at 200°C for Mg-1.5Sn-2.4Zn -2Al-0.1Na at% alloy.

The optimized alloy Mg-1.5Sn-2.4Zn-2Al was micro-alloyed with Na in a similar fashion to the high-Sn- TAZ1031-0.1Na alloy. The result shown in Figure 5.9 shows the Na addition successfully and dramatically enhanced the age hardening response achieving ~96 HV upon only 3h of ageing at 200°C.

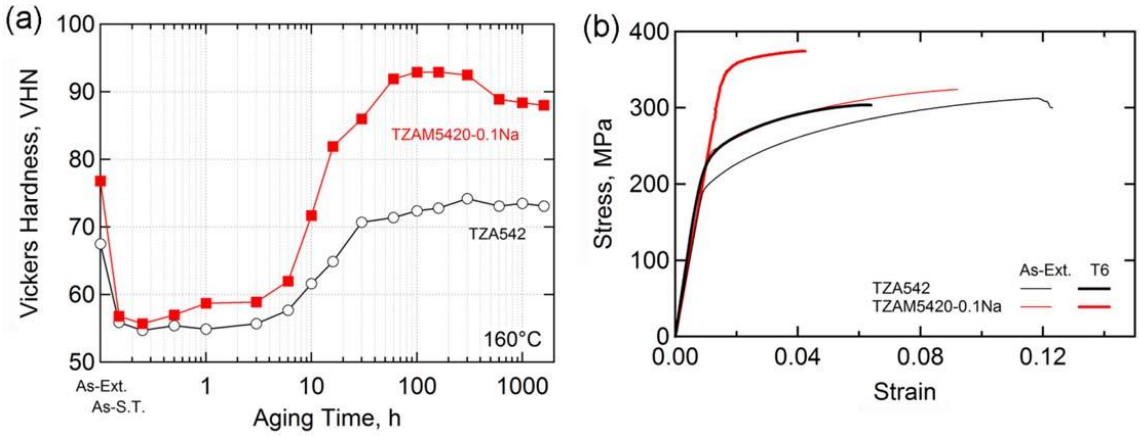

Fig 5.10 (a) Age hardening response of optimized alloys during aging at 160 °C for TZA542 and TZAM5420-0.1Na alloys. (b) Stress-strain curves of the as-extruded and T6 treated TZA542 and TZAM5420-0.1Na alloys

In a similar fashion to previous attempt to investigate the post extrusion T6 response of extruded high-Sn TAZ1031 alloys, Mn microalloying was performed in an attempt to reduce grain growth upon solution treatment on the Mg-1.5Sn-2.4Zn-2Al-0.1Na (TZAM5420-0.1Na).

The newly developed low-Sn Mg-1.5Sn-2.4Zn-2Al (TZA542), and Mg-1.5Sn-2.4Zn-2Al-0.1Na (TZAM5420-0.1Na) were extruded at 300°C and extrusion ram speed of 2 mm/s followed by T6 treatment consisting of solution treatment at450 °C for 15 min. followed by artificial ageing at160 °C. Accordingly Tensile testing was performed to evaluate the mechanical property in tension for noth as-extruded and T6 aged conditions. The results are shown in Figure 5.10. The ageing curve shows a decrease in as quenched state ~55 HV followed by an increase in ageing response to ~95HV for the TZAM5420-0.1Na alloy in 100h as opposed to only 75HV for the TZA542 alloy taking ~300h.

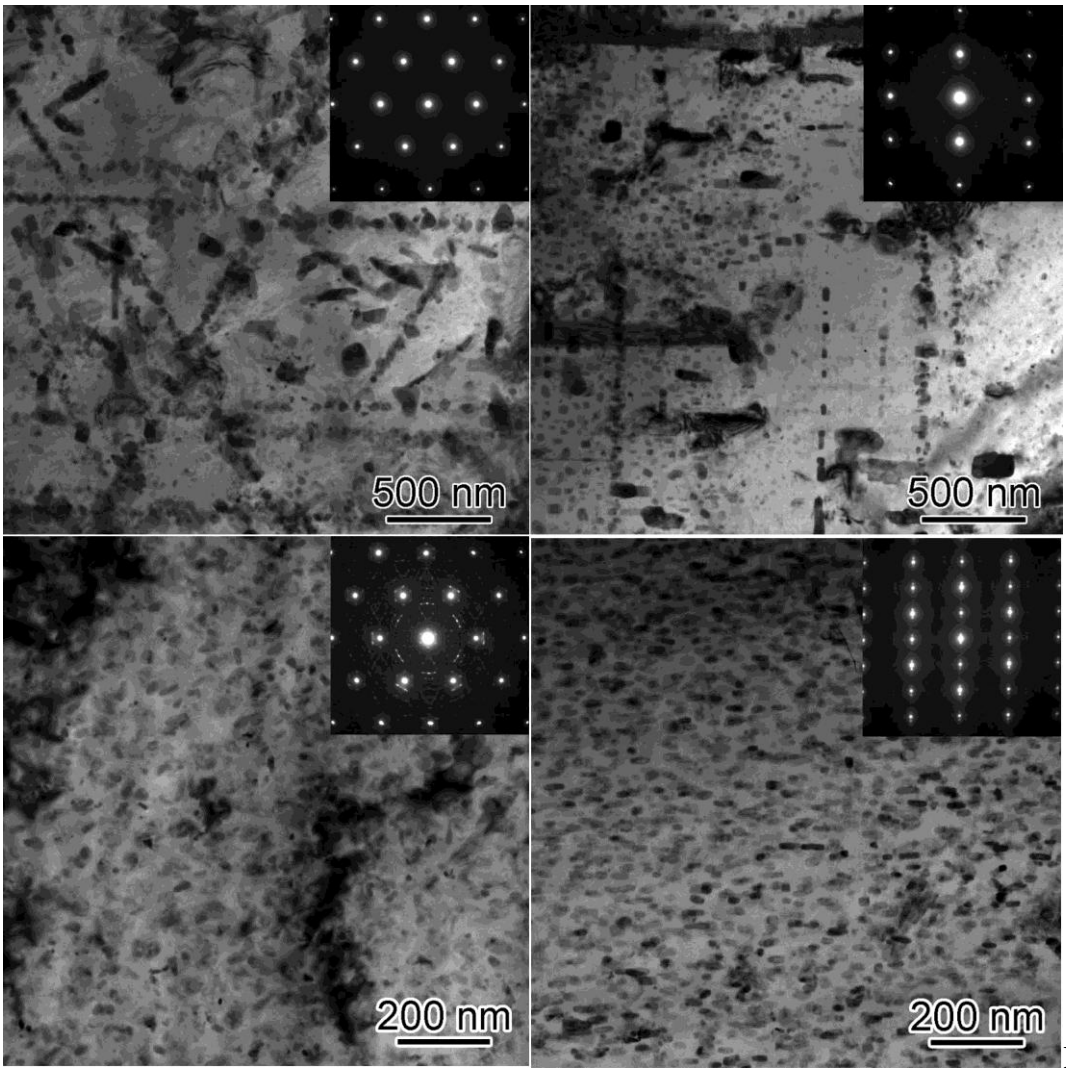

Fig 5.11:

Figure 5.11: TEM bright field images of T6 treated TZA542 (top), TZAM5420-0.1Na alloy (bottom) extruded at 300°C, ram speed =2mm/s from basal (left)and prismatic zone axis (right).

In the T6 treated TZA542 alloy, precipitates are heterogeneously dispersed within the matrix in contrast to the microstructure of the T6 treated TZAM5420-0.1Na shown in the bottom half of Figure 5.11 where refined lath-shaped Mg_2Sn with the length of about 110 nm form on the basal plane with much higher number density as compared to the TZA542 alloy. The precipitates in TZAM5420-0.1Na Precipitates are homogenously dispersed within the matrix.

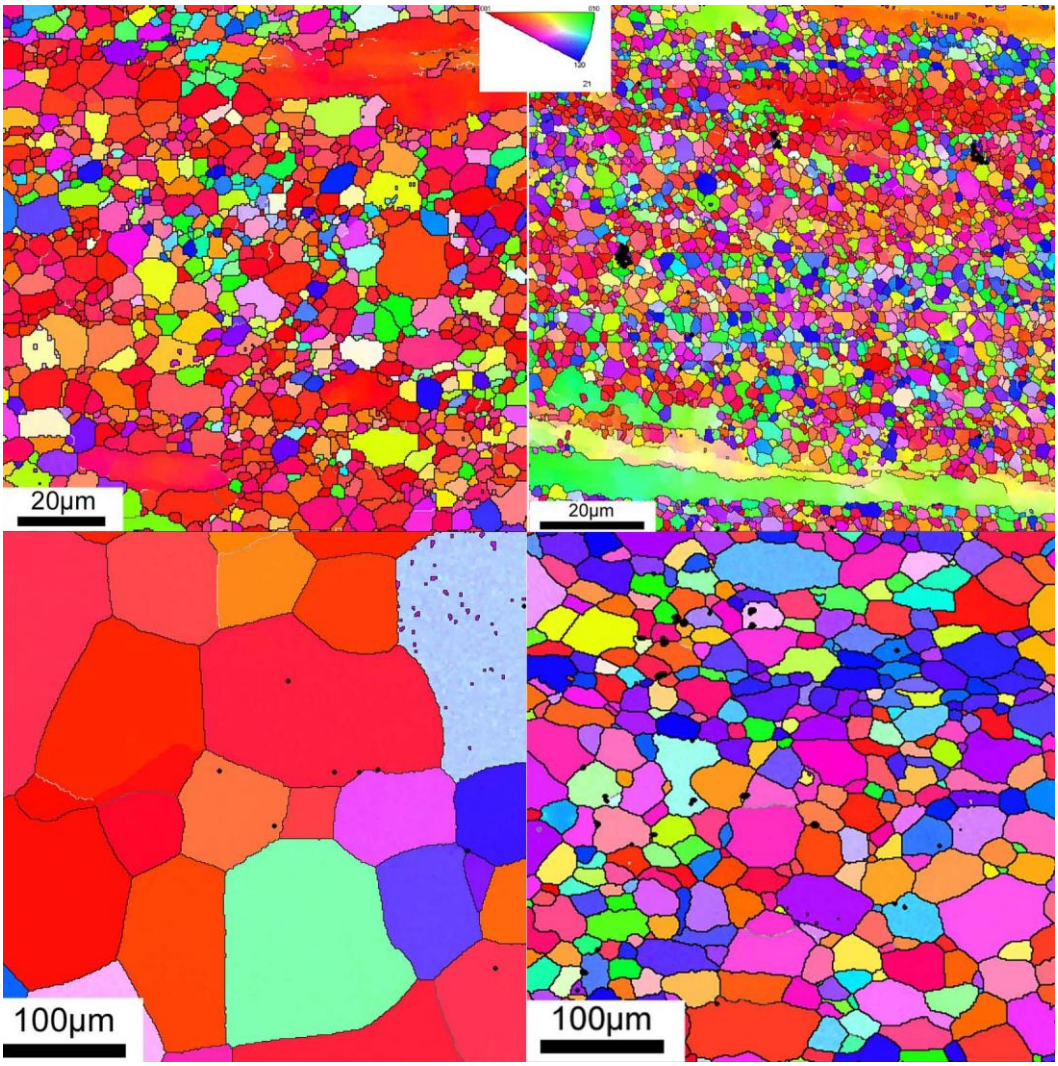

Fig 5.12: Top: EBSD IPF-Z orientation maps of as extruded TZA542 (Mg-1.2Sn-1.7Zn-2Al), and TZAMN54200 (Mg-1.2Sn-1.7Zn-2Al-0.1Mn-0.1Na) extruded at 300C, ram speed =2mm/s, Bottom: same alloys solution treated at 450°C (data taken from a plane normal to radial direction)

Figure 5.12 show the inverse pole figure (IPF) maps obtained from the as-extruded TZA542 and TZAM5420-0.1Na alloys from a plane parallel to the extrusion direction. Both as-extruded samples exhibit the bimodal grain structure consisting of fine and equi-axed recrystallized grains, and coarse un-recrystallized grains elongated along the extrusion direction. The recrystallized grains in the TZA542 alloy have the average grain size of 4.5 µm while those in the TZAM5420-0.1Na alloy have slightly finer grain size of 2.5 µm..

The grain structure exhibits the fully recrystallized feature on the solution treatment as shown in the IPF maps of the solution treated TZA542 and TZAM5420-0.1Na alloys shown in bottom.

While the grains in the TZA542 alloy significantly coarsen to 89.5 μm after the solution treatment, the grain grew to only 25.3 μm in the TZAM5420-0.1Na alloy.

.5.4 Summary and Conclusions

- The TAZ1031 alloys do not respond well to T5 and T6 treatment post extrusion.
- TAZ1031-0.1Na alloys show an enhanced ageing response after T6 treatment post extrusion.
- Mn additions lead to lowering grain growth during solution treatment post extrusion.
- The as-extruded TZA542 alloy exhibits the yield strength, σ_{YS}, of 202 MPa, with the elongation to failure, ε, of 0.11. After the T6 aging, the σ_{YS} of the TZA542 alloy slightly increases to 228 MPa while the TZAM5420-0.1Na alloy shows significant strengthening by T6 aging to give σ_{YS} of 347 MPa although the tensile elongation ε decreases to 0.03.
- The enhanced strength in the as-extruded and T6 aged TZAM542-0.1Na alloy is attributed to enhanced precipitation hardening caused by Na additions acting as heterogonous nucleation sites for Mg_2Sn precipitation in addition to Mn lowering grain growth during solution treatment post extrusion.

References

[1] T. Sasaki, K. Yamamoto, T. Honma, S. Kamado and K. Hono, Scr. Mater. 59 (2008) 1111–1114

[2] F. R. Elsayed, T.T. Sasaki, C.L.Mendis, T. Ohkubo, and K. Hono, Mater. Sci. Eng. A, 566 (2013) , pp. 22-29.

[3] F. R. Elsayed, T.T. Sasaki, C.L.Mendis, T. Ohkubo, and K. Hono, , Scripta Mater. 68 (2013) 797–800

[4] T.T. Sasaki, J.D. Ju, K. Hono, K.S. Shin, Scripta Mater. 61 (2009) 80.

[5] J.R. TerBush, M. Setty, N. Stanford, M.R. Barnett, A.J. Morton, J.F. Nie, Proceedings of 9th International Conference on Magnesium Alloys and their Applications, 2012, pp. 579.

Chapter 6 - Summary and Conclusions

Chapter (2) Mg-Sn system alloy design > Macro-alloying

The aluminum additions had a significant effect on the peak hardness values and the time to reach peak hardness. The increment in the hardening response was about 23HV in the ternary Mg-2.2Sn-3Al. The optimized composition exhibited refined precipitate size and increased homogeneity of precipitate distribution. In addition to higher frequency of non basal precipitates. .

.

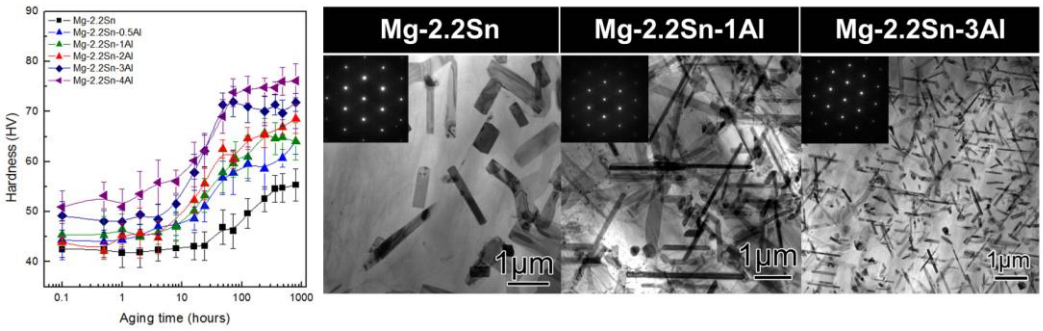

Fig.5.1: Age hardening behavior of various ternary Mg-Sn-Al alloys , (right): TEM bright field images of the peak-aged alloys.

Chapter (2) Mg-Sn system alloy design > Micro-alloying

The peak hardness achieved was enhanced further up to~82 Hv vy Zn microalloying, and average precipitate length of the Mg-2.2Sn-3Al-0.5Zn quaternary alloy was refined to about ~32% compared to that of the ternary Mg-2.2Sn-3Al alloy.

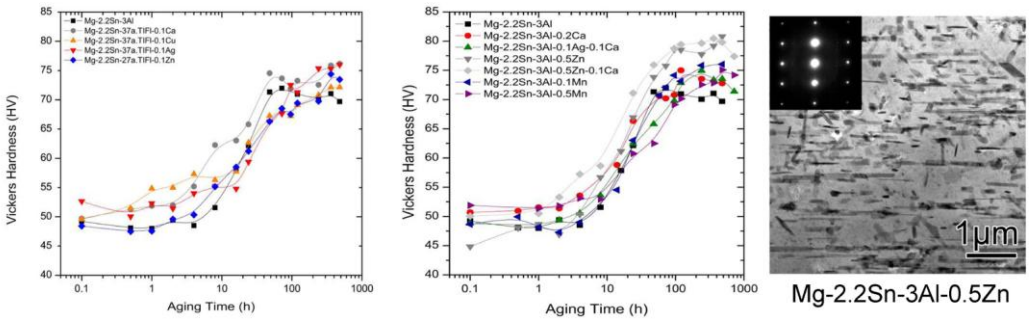

Fig.5.2: Age hardening behavior of various quaternary Mg-Sn-Al alloys , (right): TEM bright field image of the peak-aged Mg-2.2Sn-3Al-0.5Zn alloy.

Chapter (3) Na microalloying effect

The Na micro-alloyed Mg-9.8Sn-3.0Al-0.5Zn-0.1Na alloy (TAZ1031-0.1Na) showed the highest age hardening response with the fastest kinetics among the RE-free Mg-Sn based alloys reported so far. The peak hardness exceeding 100 HV that is usually unachievable in magnesium alloys without rare earth elements has been confirmed in the alloy after aging for only 10 h at 180°C. The successful improvement in the aging response was made possible by introducing Na clusters as heterogeneous nucleation sites for the Mg_2Sn precipitates, which substantially refine the aged microstructure.

.

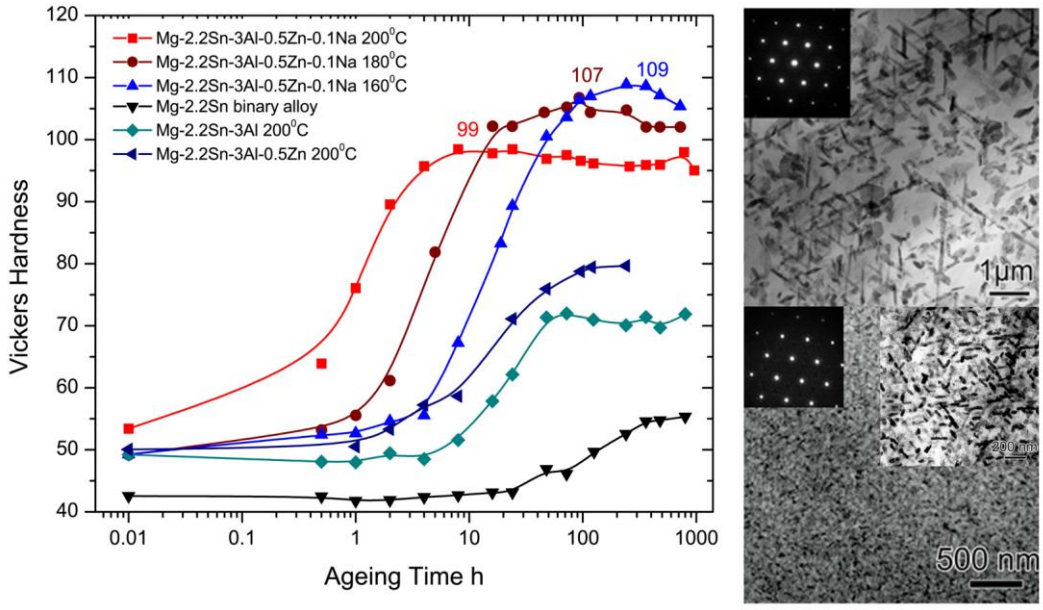

Fig.5.3: Age hardening behavior of Mg-2.2Sn-3Al-0.5Zn-0.1Na alloy at various temperatures , (right): TEM bright field images of the peak-aged alloys with and without Na addition.

Chapter (4) Extruded TAZ alloys processing-property relationship

The effect of different extrusion conditions on AZ31, TAZ1031, and TAZ1031-0.1Na has been studied, and correlated to the final microstructure, texture, and mechanical properties. The TAZ1031 alloy showed low yield asymmetry and a versatile strength-ductility combination ranging from medium to high strength tailored by the extrusion processing conditions. The TAZ extruded alloys showed medium 214 MPa to high strength ~319 MPa which is enhanced further up to 336MPa by Na addition The TAZ1031-0.1Na alloy shows further enhanced tensile yield strength of~336 MPa, which is a new strength milestone for a low cost RE-free Mg-Sn alloy without using expensive alloying elements but the absence of sufficient ductility may be detrimental to commercial attractiveness as to mainstream structural components. A future strategy to optimize the alloy composition and further improve the strength-ductility combination will prove useful to explore the potent

effect of Na micro-alloying in enhancing the age hardening without sacrificing too much ductility.

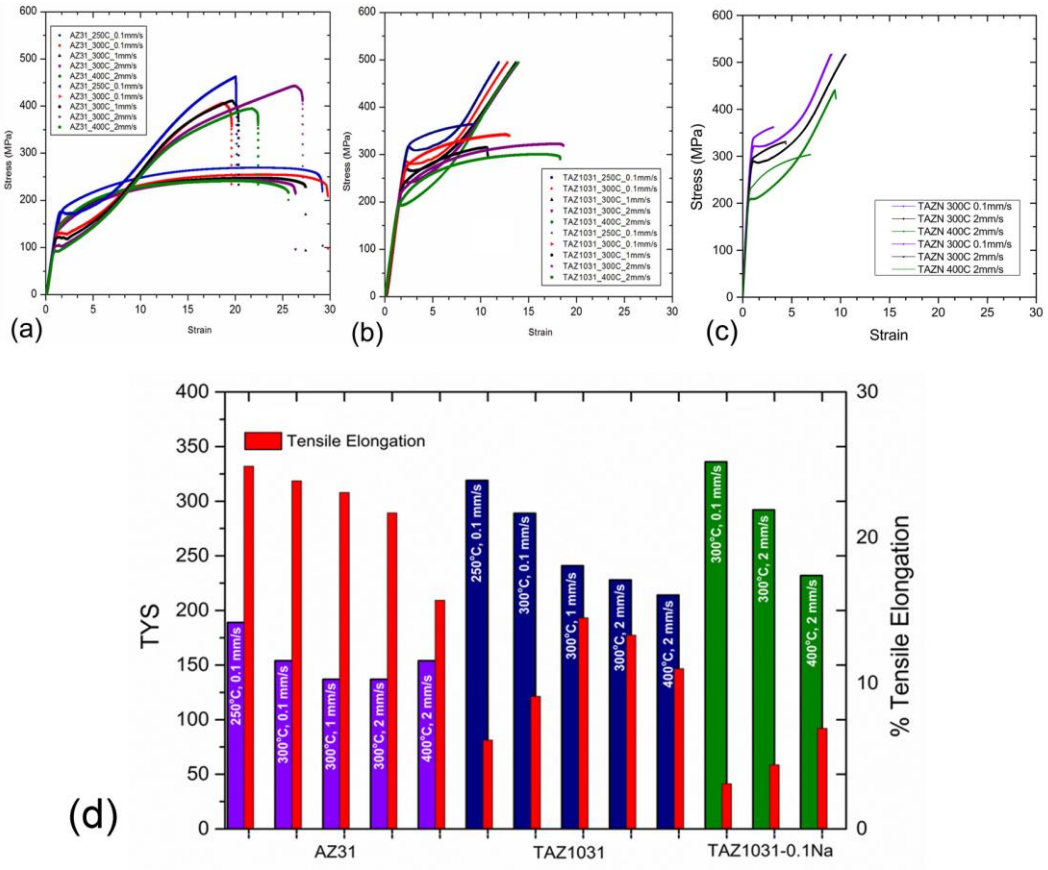

Fig. 5.4 shows stress-strain curves of the extruded alloys at different conditions & comparison to AZ31 commercial alloy

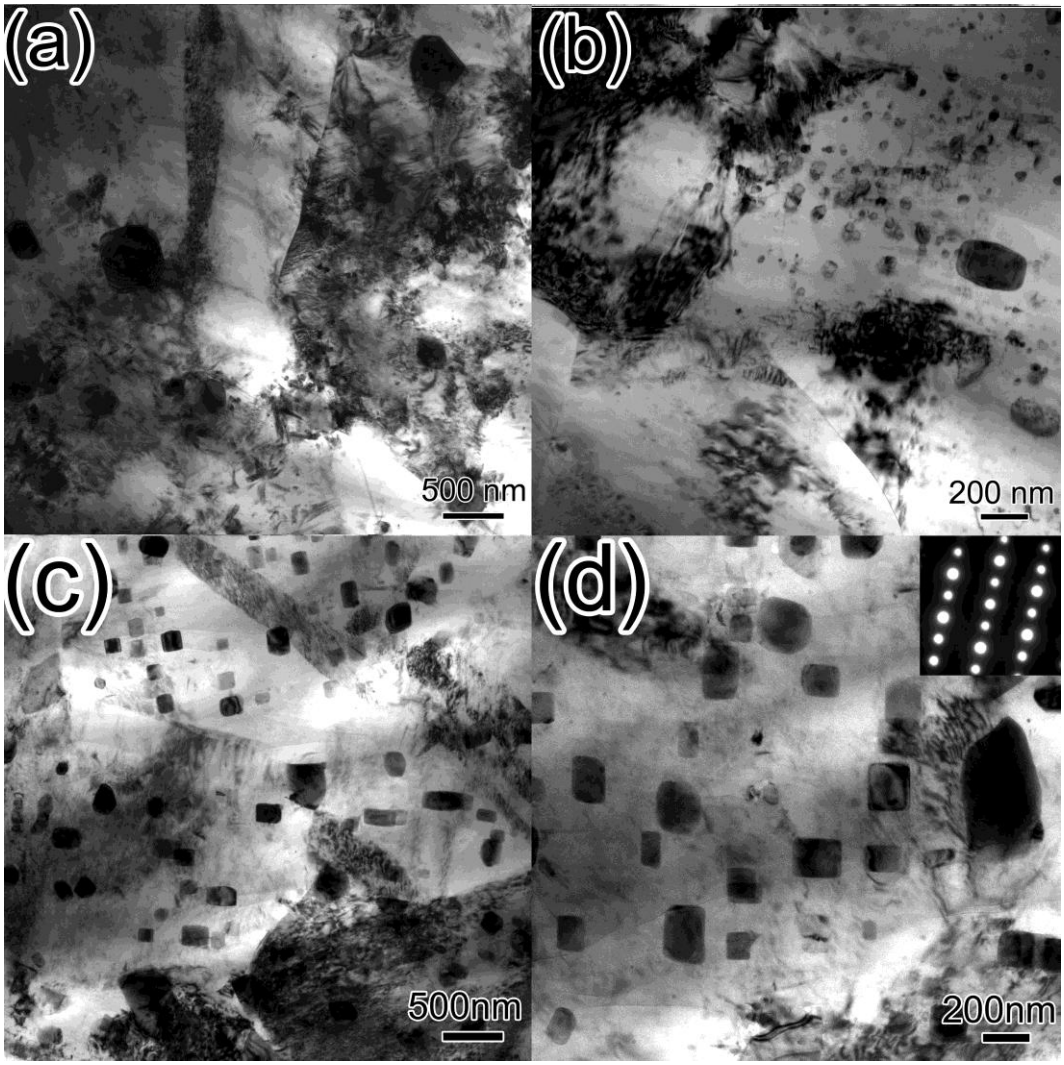

Fig. 5.5 shows TEM micrographs of a,b) TAZ1031 alloy extruded at 400°C with a ram speed of 2mm/s, e,f) TAZ1031-0.1Na extruded at same condition

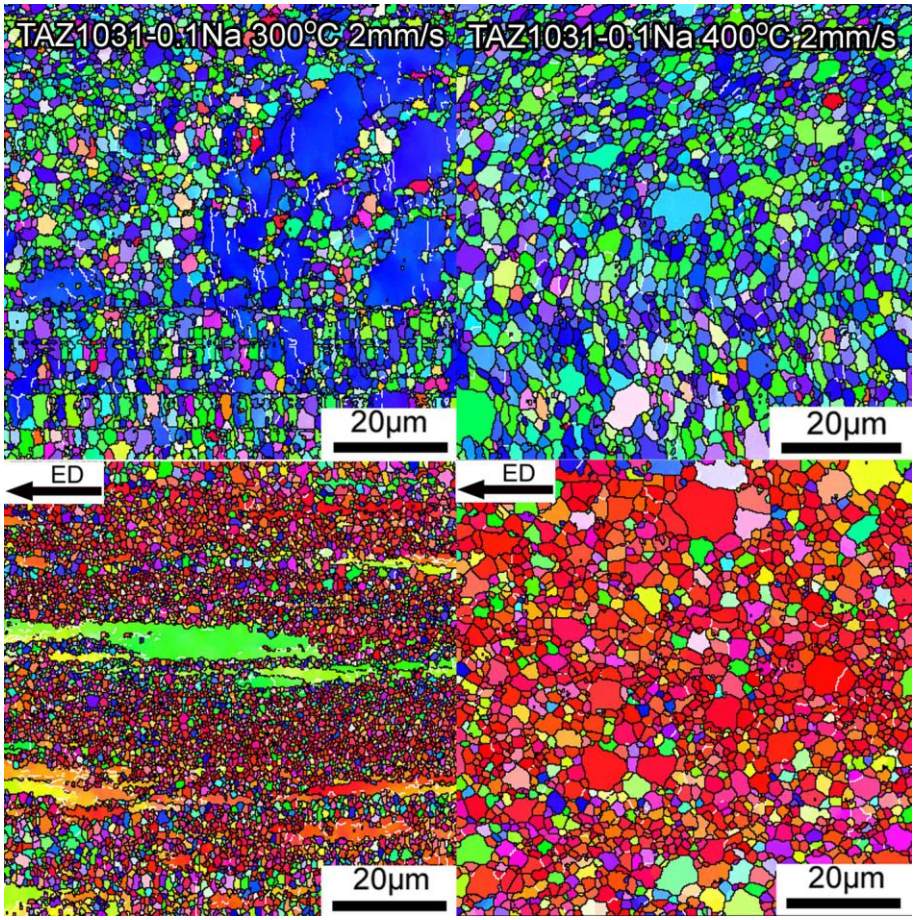

Fig. 5.6 shows EBSD IPF-Z orientation maps of TAZ1031-0.1Na alloy extruded at 300°C and 400°C with a ram speed of 2 mm/s

Chapter (5) Further Alloy optimization

The TAZ1031-0.1Na alloy showed recovered ageing response up to ~100 HV upon T6 aging treatment post the extrusion process, however since the TAZ1031-0.21Na alloy is heat treated at high temperature of 525°C and it showed severe reduction in ductility in T6 condition post extrusion, alloy composition optimization was undergone to explore the possibility of improving property after T6 treatment post extrusion. Therefore alloy optimization by reducing the Sn amount, and increasing Zn was performed; we are able to reduce the solution temperature at which the alloy is heat treated to 450°C. After

microalloying the optimized alloy with Na, and extruding it, we could find significant precipitation strengthening of the Mg-5.4Sn-4.2Zn-2.0Al-0.1Mn-0.1Na alloy by solution treatment and artificial aging. The yield strength increased from 243 to 347 MPa by aging at 160 °C for 100 h after a solution treatment at 450 °C for 0.25 h. This high strength is attributed to the inhibition to the grain growth by Al-Mn particles during the solution treatment and refinement of the precipitate by Na microalloying addition.

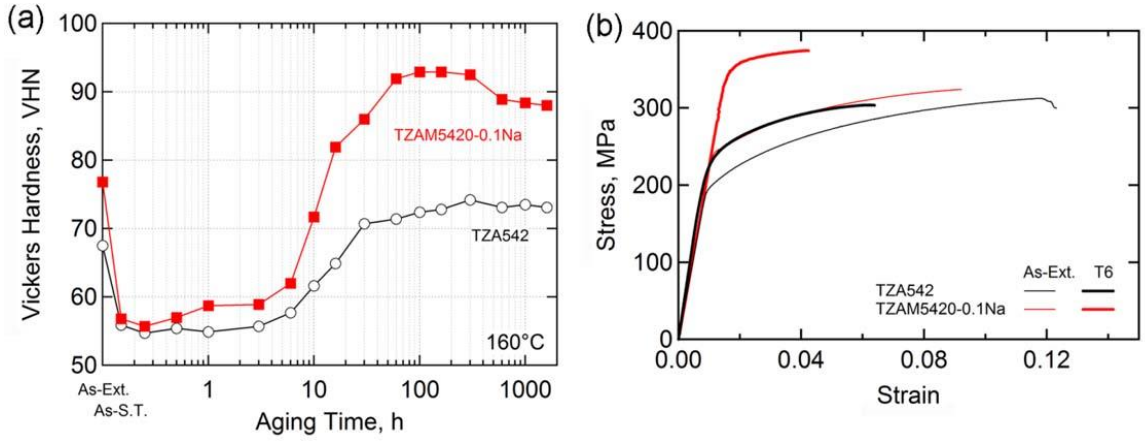

Fig 5.7 (a) age hardening response of optimized alloys during aging at 160 °C for TZA542 and TZAM5420-0.1Na alloys. (b) Stress-strain curves of the as-extruded and T6 treated TZA542 and TZAM5420-0.1Na alloys